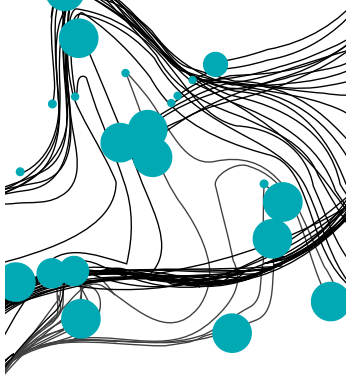

On the Development of a Ground-Positioned Microphone Phased Array for Fly-Over Noise Measurements on Unmanned Aerial Vehicles

Master Thesis
EFD-454

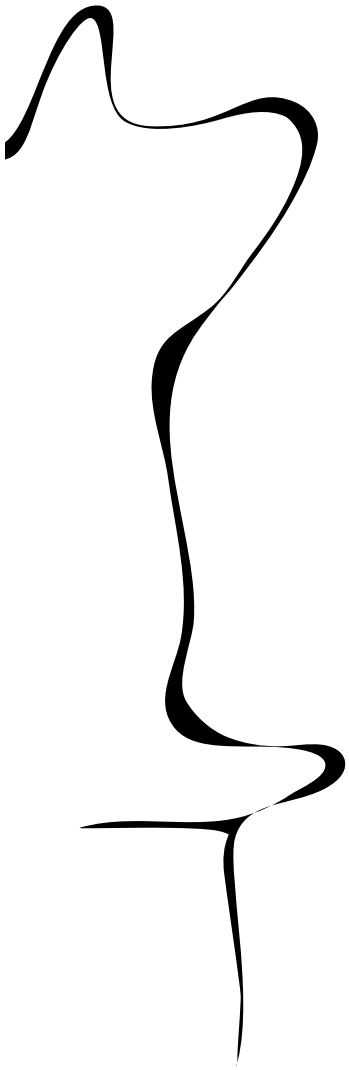

Author: J.H.B. Smits

Assessment Committee:
Chair:
prof.dr.ir C.H. Venner

Members:
prof.dr.ir H. Askes (external member)
dr.ir. L. Hirschberg (member)
dr.ir. M.P.J. Sanders (supervisor)

Date:
September 11, 2024

UNIVERSITY OF TWENTE.

Abstract

This thesis details the development of a ground-positioned microphone phased array designed to localize and quantify noise from unmanned aerial vehicle flyovers. The microphones used in the array are low-cost analogue MEMS microphones designed to withstand outdoor weather conditions. A custom printed circuit board and electronic circuit were developed to power the microphones and optimize their performance. The array was designed for flexible microphone positioning, enabling performance optimisation based on the specific sound source of interest. A measurement method and setup, known as acoustic GPS, was implemented to accurately and efficiently determine the positions of the microphones. Far-field acoustic beamforming algorithms were implemented in Python. Extensive measurements were conducted in an anechoic chamber to validate the far-field acoustic beamforming algorithms and verify the microphone calibration method. Additionally, the performance and robustness of the measurement system were evaluated during outdoor flyover tests with a quadcopter UAV. The capabilities of the ground-positioned microphone phased array system were successfully demonstrated, showcasing its potential as a valuable tool for noise analysis of UAVs, ultimately contributing to the mitigation of UAV noise pollution.

Contents

Chapter 1

The Rise of Unmanned Aerial Vehicles

1.1 The evolution of unmanned aerial vehicles

Unmanned aerial vehicles (UAVs) were initially developed during the twentieth century for military purposes. These platforms were meant to perform dull, dirty, and dangerous tasks. For example, during the First World War, the first pilotless aircraft was tested in March 1917. Equipped with early radio technology, it was designed to destroy an enemy's zeppelin. A few years later, the British produced a radio-controlled aircraft to be used for training purposes, nicknamed 'the drone' [2], shown in Figure 1.1 [1]. The first large-scale deployment of UAVs was during the Vietnam War, where they were tasked with surveillance, being decoys, and dropping both bombs and leaflets.

Figure 1.1: The preparations on the *Queen Bee*, being observed by Winston Churchill and Secretary of State for War Captain David Margesson [1].

In the early stages of UAV development, aircraft and signal transmission systems were costly. However, costs have decreased significantly due to advancements in motors, batteries, and other electronics, making drones and radio transmitters cheaper. The reduced costs and simplified transmission systems popularised UAVs for the private sector, leading to their widespread use in various civil applications.

1.2 Configurations of unmanned aerial vehicles

Unmanned aerial vehicles (UAVs), more commonly known as drones, are remotely operated aerial platforms without a human on board [3]. Today, a wide variety of UAVs are available. Their application, along with the pros and cons, depends on the configuration of these platforms. In the following paragraphs, multirotor, fixed-wing, and VTOL UAVs are shortly discussed.

Multirotor UAVs have more than two lift-generating rotors. Figure 1.2a illustrates a multicopter platform, specifically a quadcopter. Other multirotors can include six or even eight motors if they require more power, commonly called hexacopters or octacopters, respectively. Consumers often use them for cinematography, drone racing, and other leisure-related activities. These platforms are more manoeuvrable, can hover in place, and can land or take off vertically.

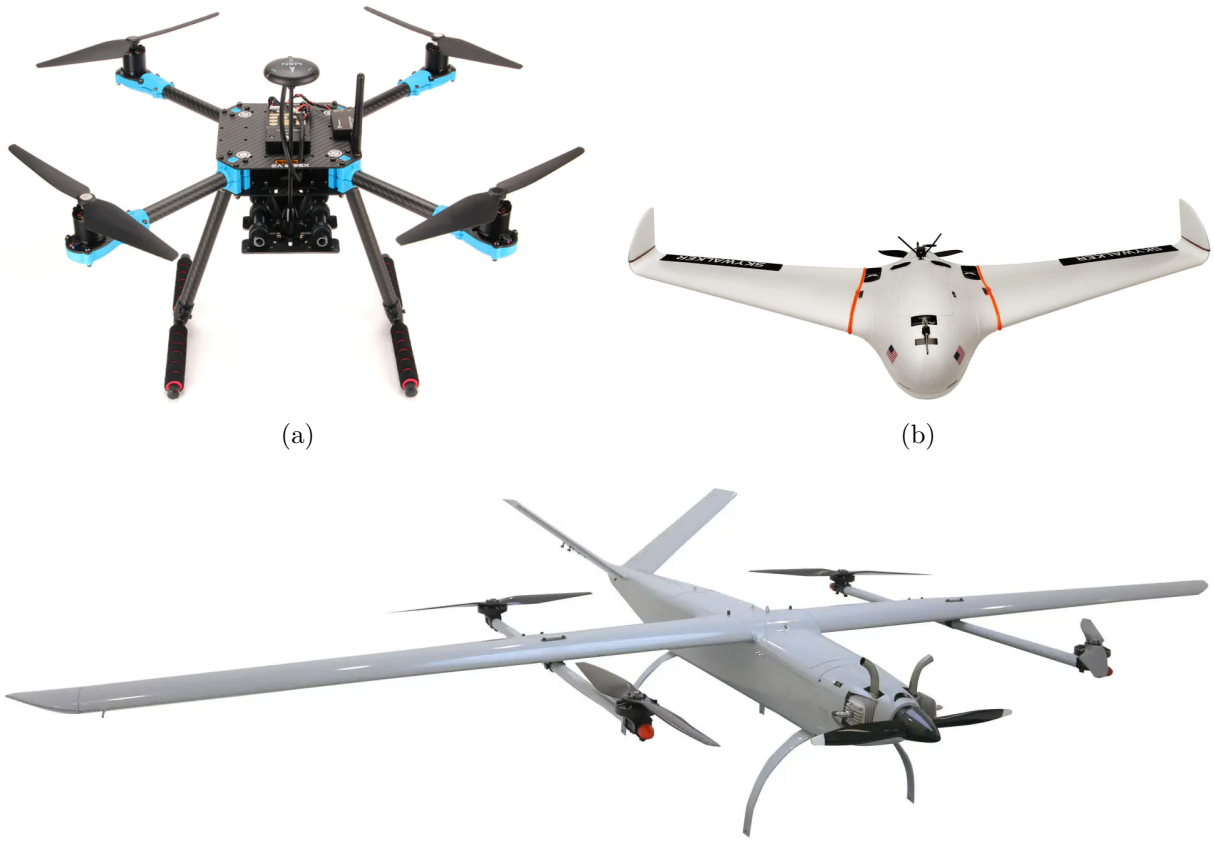

(a) (b)

(c)

Figure 1.2: (a) The Holybro PX4 X500 multirotor development platform. (b) Shows the Skywalker, a fixed-wing UAV. Lastly, (c) shows a VTOL UAV from Brouav.

Another type of UAV is the fixed-wing UAV. These drones have at least one fixed wing that provides lift rather than vertical rotors. They can cover more extensive distances at increased altitudes with respect to multirotors. However, these platforms must be in forward flight for the wing to provide lift. This also means they are less manoeuvrable than multirotors and need a runway for take-off and landing. An example of a fixed-wing drone is given in Figure 1.2b.

A third type of UAV is a hybrid of multirotors and fixed-wing drones. A Vertical Take-Off and Landing drone (VTOL) can transfer between horizontal and vertical flight. This UAV has a fixed wing and a multitude of rotors to accomplish this. It, therefore, combines the manoeuvrability of a multirotor with the endurance of the fixed-wing drone. A VTOL UAV is shown in Figure 1.2c, where the rotors and a fixed wing can be seen.

These UAVs can be broadly deployed into many facets of society [4,5]. As a few examples, these UAVs can be used in agriculture to help with herding, sowing, and monitoring [6]. Simultaneously, these platforms inspect and maintain railways, bridges, highways, wind turbines, and other hard-to-reach places [7,8]. Furthermore, UAVs are used for parcel delivery, thereby reducing transport time [9]. One of the studies, by Aydin et al. [9], has shown the extensive market for these platforms in the present and the possible future. However, while the deployment of these aerial platforms is vast and ever-increasing, scientific research is crucial to assess the potential impact of widespread UAV implementation in everyday life on the environment.

1.3 Environmental impact of UAV noise radiation

A major environmental concern is the potential impact of UAVs on noise pollution. Currently, road traffic noise is one of the top-ranking factors affecting human health [10, 11]. However, current literature also suggests that drone noise is significantly more annoying than road traffic [12–14].

Using recordings of UAV fly-overs, S. Hara et al. showed that participants' stress levels increased with higher UAV noise power and reduced again as the noise subsided. However, subconscious stress levels remained unchanged even when noise levels decreased [14]. Further research suggests that health effects of noise over-exposure are sleep disorders, cognitive impairment, hypertension, ischemic heart disease, diastolic blood pressure, reduction of working performance, and increased annoyance [10,11,15]. This significant impact on human health led the European Union Aviation Safety Agency (EASA) to propose guidelines for measuring drone noise [16].

Furthermore, noise is also a significant factor in the social acceptance of UAVs. A study by Schäffer et al. [17] demonstrated that an individual's attitude towards UAVs is primarily influenced by their concern for noise, which was supported by a study from Torija et al. [18]. The study furthermore showed that concerns about noise were more significant if the participant had a previous encounter with the noise from a UAV. Paying attention to the noise footprint of these drones can, therefore, significantly increase the implementation grade and success rate of UAVs in the urban environment [19]. Hence, the localisation and quantification of UAV noise sources are of great interest to the scientific and the general community.

1.4 The necessity for fly-over noise measurements on UAVs

Many UAV noise measurements are performed in anechoic chambers to avoid any environmental impact on the measurement [12, 13, 20]. However, UAV measurements in confined spaces can create inaccurate or incomplete results. Flow recirculation and ground effect can significantly impact measurements in relatively small spaces compared to the UAV. Furthermore, drone operating conditions (e.g. manoeuvres and forward flight) can notably affect the radiated noise

due to a change in flow regime [12, 20, 21]. Therefore, the importance of outdoor fly-over noise measurements on UAVs is stressed to perform measurements in accurate flow conditions.

Furthermore, most current literature focuses on UAV sound power levels, frequency power spectra, directivity, and perception in humans using a few microphones [12, 20, 21]. However, to better understand what is making noise on UAVs, some literature has attempted to use acoustic cameras [22,23]. These cameras, comprising a multitude of microphones, are used to 'see' sound. Therefore, these acoustic cameras could be used to develop aerial platforms and improve the noise footprint.

1.5 The focus of this work

Developing and using an acoustic camera is nontrivial. Numerous acoustic cameras consist of many expensive condenser microphones sampled by a costly data acquisition system, making the start-up costs daunting. Furthermore, many microphone arrangements are fixed and optimised for specific sources. This optimisation problem can be avoided by using a flexible microphone arrangement (microphones on individual plates), such that these cameras can be optimised based on the sound source under consideration. However, accurately determining the positions of these individual microphones can be difficult. Therefore, developing and using an acoustic camera is complex and presents many challenges.

However, these acoustic cameras can significantly help engineers design more silent UAVs. This would improve social acceptance of UAV employment and would reduce the impact of UAV deployment on human health. Therefore, this master's thesis concerns developing and using an inexpensive acoustic camera to localise and quantify noise sources on UAVs in outdoor fly-over measurements.

Chapter 2

Aeroacoustics of unmanned aerial vehicles

Sound, in reality, can be radiated due to vibrating strings, unstable rotating discs, the diaphragm of a speaker, or the motion of fluids. The field of acoustics deals with such sound's production, transmission, reception, control, and effects [24]. Aeroacoustics is a sub-regime of acoustics mainly concerned with sound in air [25, 26].

This chapter discusses the complexity of UAV aeroacoustics by examining some of the mechanisms that produce noise on a drone. First, it focuses on airfoil-induced noise. Then, it discusses the additional sound sources on a rotor. Lastly, it discusses a UAV's aeroacoustics, stressing the complete problem's complexity with multiple rotors and a frame.

2.1 Airfoil noise

UAVs use rotors to produce thrust and achieve flight. The blades on these rotors are built up from cross-sections, named airfoils. Furthermore, these airfoils are the cross-sections of wings, rotors, and propellers. Thus, discussing their produced noise is the first step in understanding rotor noise and, eventually, UAV noise.

The following sections describe the mechanisms that produce noise on an airfoil in undisturbed flow. Lastly, leading-edge noise due to a turbulent domain is also discussed.

Laminar boundary layer separation noise

Laminar boundary layer vortex shedding can occur when, on either side of the airfoil, a predominantly laminar flow is present [27]. Such noise is created due to an interaction between streamwise flow instabilities, called Tollmien-Schlichting waves, and the vortices shed at the trailing edge, as shown in Figure 2.1. The streamwise instabilities are initiated by a disturbance on the skin of the airfoil but are eventually sustained by the trailing edge vortices in a feedback loop. Furthermore, a feedback loop exists since this is an interaction between the trailing edge vortices and the Tollmien-Schlichting waves. Therefore, only specific frequencies are excited about the shedding rates of the trailing edge vortices [27, 28].

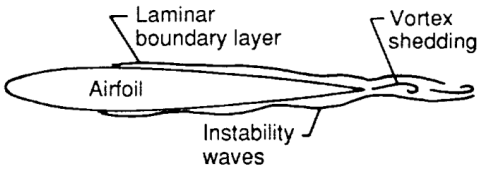

Figure 2.1: Laminar boundary layer noise [27]

Turbulent boundary layer noise

At increased Reynolds numbers, a turbulent boundary layer develops on the airfoil. Turbulent boundary layer noise is produced by the turbulent structures inside this boundary layer, producing chaotic pressure fluctuations on the skin of the airfoil, as shown in Figure 2.2. Boundary layer pressure fluctuation statistics are vital in predicting the produced noise due to the chaotic nature of turbulence [25]. Furthermore, research shows that the conditions under which these turbulent structures evolve play an essential role in the noise that is radiated [27]. Lastly, the sound pressure created by this mechanism scales with Mach to the fifth power at low frequencies.

Boundary layer separation noise

Boundary layer separation noise is most prominent at high angles of attack. Small, turbulent structures form at the trailing edge at slight angles of attack. However, with an increasing angle of attack, the flow separation region will move in the direction of the leading edge and the turbulent structures' integral length scale increases, as shown in Figure 2.3. This can result in a deep stall, causing a low-frequency dominant noise over the entire chord of the wing [27]. Furthermore, this flow separation is often dynamic, with a highly unsteady flow.

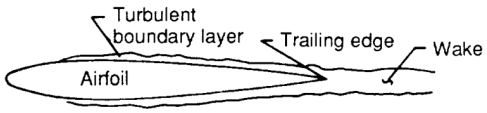

Figure 2.2: Turbulent boundary layer noise [27]

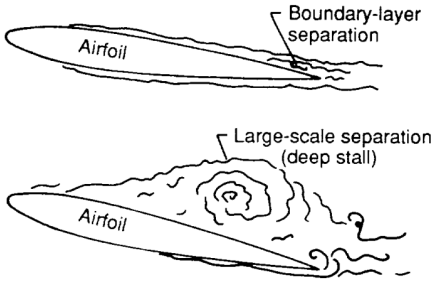

Figure 2.3: Seperation stall noise [27]

Trailing edge bluntness noise

Noise due to trailing edge bluntness was established by Brooks and Hodgson to be an import self-noise source [29]. Due to a finite trailing edge thickness, vortex shedding occurs at the trailing edge, radiating noise into the far-field. The dominant frequency of the noise is often scaled with the velocity of the flow U and the thickness of the blunt edge h to obtain the Strouhal number, $\mathrm{St}'''_{peak} = \frac{f_{peak}h}{U} \approx 0.1$. However, for rotor-blade and wing designs, the bluntness of the airfoil is relatively small compared to the boundary layer thickness. This significantly reduces the sound power of the tonal component of this mechanism [30].

Tip vortex noise

Tip vortices are generated due to the pressure difference between the tip's low- and high-pressure sides. Due to the formation of these vortices, structures form in the wake of a tip with thick, viscous, turbulent cores [27]. It is taken to be that these structures pass over the trailing edge in the tip region, causing noise radiation [27]. These structures cause high-frequency noise with respect to the other noise sources depending on the length scale and the loading of the wing.

Leading edge noise

Leading edge noise (turbulence-impingement noise) is no longer considered airfoil self-noise. This noise is produced due to the blades' movement through a region of turbulent or unsteady flow impinging on the leading edge [27, 30, 31]. This mechanism's perceived noise is related to the turbulent inflow statistics and the leading edge radius [27]. This is an important noise source to consider in low Mach number flows [31].

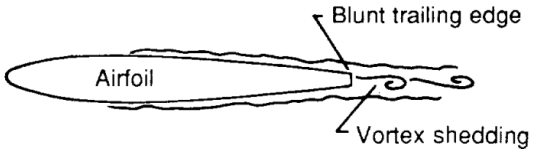

Figure 2.4: Trailing edge bluntness noise [27]

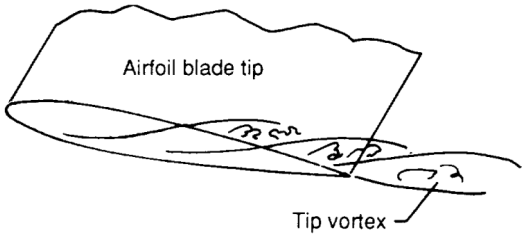

Figure 2.5: Tip vortex noise [27]

As mentioned, airfoils are the 'building blocks' of rotors. However, rotor geometry and operating conditions are more complex than a simple airfoil. A rotor consists of multiple rotating blades, making the aerodynamics and aeroacoustics more complex. Therefore, introducing the additional sound sources on a rotor is essential.

2.2 Rotor noise

The types of rotor noise are split into three categories in the frequency domain, which can be harmonic, narrowband, or broadband [32]. They are also frequently divided into another set: steady, unsteady, and random sources.

Harmonic noise is produced by sources that repeat themselves during every rotor rotation. The sound sources on a single blade repeat themselves for every blade on the rotor, giving rise to harmonics in the frequency content at frequencies described by Equation 2.2.1 [32]. Here, N is the number of blades on the propeller, and RPM the rotations per minute. The fundamental frequency of this tone is called the blade passing frequency (BPF). Furthermore, since the produced signal is not purely sinusoidal, multiple harmonics are present, given by $\text{BPF} \cdot n$ where n is an integer value larger than zero. For consumer drones like the DJI Mavic Air 2, the typical rotational velocity of the rotor during hover is around 100 Hz, generating a BPF of 200 Hz with a two-bladed rotor.

$$\mathrm{BPF} = N\frac{\mathrm{RPM}}{60} \tag{2.2.1}$$

In contrast, broadband noise is produced in a non-periodic, chaotic flow and is often due to turbulent flow interacting with the blades [32]. Its name already discloses that broadband noise has components at all frequencies. Narrowband noise is almost periodic. However, the energy is not entirely concentrated at an isolated frequency.

2.2.1 Steady sources

Steady sources are defined as sources which would appear constant in time for the rotating blade's frame of reference. Due to the rotation of the blade, these sources produce a periodic sound signature in a stationary frame of reference. These steady sources are often divided into linear thickness, linear loading, and quadrupole sources [33].

Thickness noise is produced due to the displacement of fluid by the volume of a blade. The amplitude of this noise scales with the blade's volume, while the frequency characteristic depends on the shape of the cross-section of the blade and the rotational velocity. This is why thin blades and planform sweep are often used to control this noise mechanism. A distribution of monopole sources can describe this noise mechanism well and becomes increasingly important at increased velocity.

Loading noise is a noise produced by the forces from the blade on the fluid, a combination of thrust and torque. The periodic force fluctuation of the blade on the surroundings radiates into the far field, propagating as sound. This type of noise is essential at low to moderate speeds and can be modelled using dipole sources [32].

Quadrupole sources can become important in the non-linear, transonic regime. However, thickness and loading sources are the most important noise sources when considering subsonic airfoil velocities. These non-linear contributions are often modelled using quadrupole sources surrounding the blade.

2.2.2 Unsteady sources

In contrast to steady sources, unsteady sources are time-dependent in the blade's frame of reference. This includes random and periodic loading variations on the blade. An example of periodic blade loading is the placement of a rotor near a pylon. The loading on a single blade changes during its revolution due to a difference in flow conditions near the pylon, resulting in unsteady loading. This results in noise produced at harmonics of the blade-passage frequency. The noise generated by unsteady loading is not axisymmetric, making the radiated sound even more complex [33]. Furthermore, blade vortex interaction is another example of unsteady loading and occurs in the forward flight of a helicopter [32, 34]. Unsteady loading occurs due to the impingement of a tip vortex from a leading blade against a trailing blade, rapidly changing the flow conditions on the trailing blade [32](graphically explained in Figure 2.6).

The vortices from the blades pass over the trailing blades during forward flight. This results in unsteady loading due to a sudden change in the angle of the attack. Also, the tip vortices are often surrounded by high turbulence levels that impinge on the trailing blades. This is frequently called blade wake interaction noise and is broadband in nature [32].

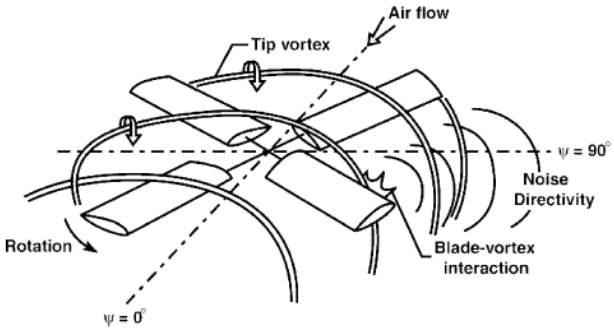

Figure 2.6: The BVI process [35].

2.2.3 Random sources

Random sources radiate broadband noise into the acoustic far-field. Depending on the operation conditions and design, rotors have two important random source mechanisms radiating broadband noise. Firstly, leading-edge noise due to turbulence impingement on the leading edge. Secondly, noise is generated due to unsteady loading near the blade's trailing edge. This fluctuating loading occurs due to the random nature of a possible turbulent boundary layer on the blade passing over the trailing edge.

2.3 UAV sound radiation

Understanding sound radiation on UAVs will support the design process of the ground-positioned microphone phased array. Furthermore, discussing the complex interactions on a UAV can help interpret the results during the measurements in chapter 7. For this purpose, airfoil and rotor noise were discussed, laying the foundation for understanding UAV sound radiation.

Looking at the expected sound pressure levels, Schäffer showed that for drones in the range of 1 to 21 kg, the expected A-weighted SPL ranges from 65 to 95 dB [17]. These measurements were performed at 1 m from the drone hovering above a reflective surface. These noise emissions slightly increased for forward flight, which was also shown by Cussen [15]. Lastly, Niesten [36] showed that the sound reflections in an urban environment from facades alone could increase the (A-weighted) sound pressure level anywhere between 3 dB until 13 dB compared to free-field measurements.

Measurements were conducted to look at the frequency spectrum of a UAV. The most prominent sources of UAV-radiated noise were attributed to tip-to-tip and rotor-strut interactions [20,37,38]. Tip-to-tip sound, according to these studies, was generated due to the unsteady loading of a blade by vorticity and turbulence ingestion in the region where rotor tips come close to each other. The rotor-strut noise was generated due to large thrust fluctuations when a blade passed over a strut, causing significant unsteady loading. They also showed that decreasing the separation distance between rotors and the distance between a rotor and strut significantly increased the radiated sound pressure levels. Furthermore, Schäffer has demonstrated that the spectral characteristics of UAV noise include low- and mid-frequency tonal components along with broadband noise [17]. They showed that the tonal components are related to the rotor's BPF and the sound from the brushless motors.

Many components on a UAV can produce noise, some of which are highlighted in Figure 2.7. When looking at a single rotor, noise can stem from turbulence ingestion, flow separation, vortex shedding, tip vortices and noise from the turbulent boundary layer. However, when looking at a complete UAV, complex interactions can also produce significant amounts of noise, such as blade-to-blade interaction, blade-frame interactions, blade-vortex interactions, blade-wake interactions, frame-wake interactions or recirculating flow [20, 39]. The sound coming from the rotors and the complex interactions make the acoustic signature of a UAV highly complex. Therefore, it is often hard to distinguish a single source of sound without extensive testing or validated numerical models.

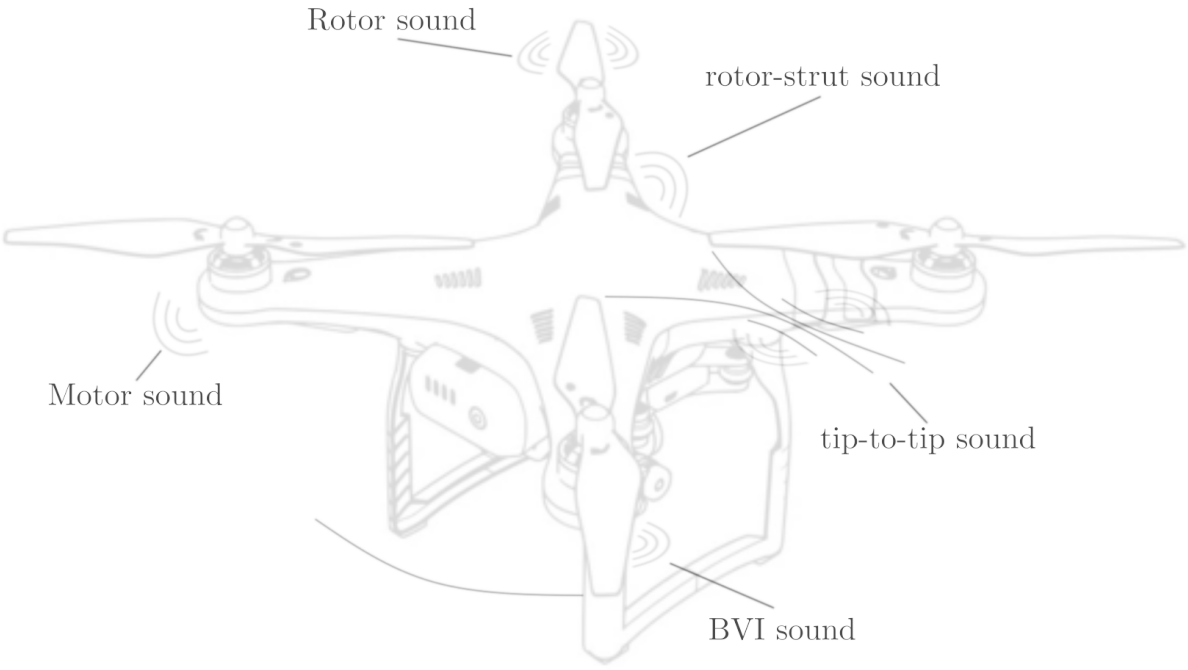

Figure 2.7: Some of the expected sources of sound on a UAV.

Chapter 3

Acoustics

The behaviour of sound, and especially its propagation through the medium, is a paramount stepping stone in understanding methods of sound source localisation. Therefore, this chapter provides the background theory used by sound source localisation algorithms, discussed in chapter 4. This is done by discussing the wave equation and the sources of sound.

3.1 Linear acoustics

The propagation of sound in air can be described with the linear acoustic wave equation. This equation is derived from the continuum mechanics framework's mass and momentum balance equations. The derivation of these two conservation equations is given in the appendix in section A.1. After the derivation of the wave equation, the generation of waves is briefly discussed by the addition of source terms in the homogeneous linear wave equation.

3.1.1 The homogeneous wave equation

Consider the generation and propagation of acoustic waves within a medium where the time-averaged properties are uniform and no significant flow is present. The medium under consideration has a pressure p, density ρ, and velocity $\mathbf{u}$. Furthermore, viscous forces are small for sound propagation over practical distances compared to inertial forces and are often ignored along with body forces such as gravity [30]. Linearising the homogeneous mass and (inviscid) momentum conservation equations, given in Equation 3.1.1 and Equation 3.1.2, is the first step in deriving the linearised wave equation.

$$\frac{\partial \rho}{\partial t} + \nabla \cdot (\rho \mathbf{u}) = 0 \tag{3.1.1}$$

$$\frac{\partial (\rho \mathbf{u})}{\partial t} + \nabla p + \rho \mathbf{u} \cdot \nabla \mathbf{u} = 0 \tag{3.1.2}$$

Sound waves are considered small perturbations to a fluid's ambient state. Pressure, density, and velocity are therefore transformed as a sum of a small perturbation and the constant reference state (p_0, ρ_0, and $\mathbf{u}_0$) as in Equation 3.1.3.

$$p = p_0 + p', \quad \rho = \rho_0 + \rho', \quad \mathbf{u} = \mathbf{u}_0 + \mathbf{u}' \tag{3.1.3}$$

Using the linearised states in Equation 3.1.1, one obtains Equation 3.1.4 for the mass conservation equation.

$$\frac{\partial(\rho_0 + \rho')}{\partial t} + \nabla \cdot \Big((\rho_0 + \rho')(\mathbf{u}_0 + \mathbf{u}')\Big) = 0 \tag{3.1.4}$$

Assuming that $\rho' \ll \rho_0$, ρ_0 is time-averaged and constant throughout the medium [40], Equation 3.1.4 can be rewritten into Equation 3.1.5.

$$\begin{aligned} \frac{\partial \rho'}{\partial t} + \rho_0 \nabla \cdot \mathbf{u}' + \rho' \nabla \cdot \mathbf{u}_0 = 0 \\ \Big(\frac{\partial}{\partial t} + \nabla \cdot \mathbf{u}_0\Big)\rho' + \rho_0 \nabla \cdot \mathbf{u}' = 0 \end{aligned} \tag{3.1.5}$$

Applying the same methodology to the momentum equation (Equation 3.1.2), the equation with linearised states is given in Equation 3.1.6, assuming an inviscid medium without body forces.

$$\frac{\partial(\rho_0 + \rho')(\mathbf{u}_0 + \mathbf{u}')}{\partial t} + \nabla(p_0 + p') + (\rho_0 + \rho')(\mathbf{u}_0 + \mathbf{u}') \cdot \nabla(\mathbf{u}_0 + \mathbf{u}') = 0 \tag{3.1.6}$$

The mean pressure gradient in a stationary, inviscid medium is often due to body forces. However, since these body forces are ignored, simplifications are possible: $\nabla(p_0 + p') = \nabla p'$. Applying these simplifications allows Equation 3.1.6 to be rewritten into Equation 3.1.7.

$$\rho_0 \Big(\frac{\partial}{\partial t} + \nabla \cdot \mathbf{u}_0\Big)\mathbf{u}' + \nabla p' = 0 \tag{3.1.7}$$

By applying $(\frac{\partial}{\partial t} + \nabla \cdot \mathbf{u}_0)$ to Equation 3.1.5 and taking the divergence of Equation 3.1.7, Equation 3.1.8 and Equation 3.1.9 are obtained respectively.

$$\Big(\frac{\partial}{\partial t} + \nabla \cdot \mathbf{u}_0\Big)^2 \rho' + \rho_0 \nabla \cdot \mathbf{u}' \Big(\frac{\partial}{\partial t} + \nabla \cdot \mathbf{u}_0\Big) = 0 \tag{3.1.8}$$

$$\rho_0 \nabla \cdot \mathbf{u}' \Big(\frac{\partial}{\partial t} + \nabla \cdot \mathbf{u}_0\Big) + \nabla^2 p' = 0 \tag{3.1.9}$$

Where $\nabla^2 = \nabla \cdot \nabla$. Subtracting Equation 3.1.9 from Equation 3.1.8, yields Equation 3.1.10.

$$\Big(\frac{\partial}{\partial t} + \nabla \cdot \mathbf{u}_0\Big)^2 \rho' - \nabla^2 p' = 0 \tag{3.1.10}$$

Lastly, the pressure can be written as a function of solely the density and entropy (as in Equation 3.1.11), considering a state of local thermodynamic equilibrium. Temperature variations are sufficiently small in this state for a 'constant temperature' approximation.

$$dp = \left(\frac{\partial p}{\partial \rho}\right)_s d\rho + \left(\frac{\partial p}{\partial s}\right)_\rho ds \tag{3.1.11}$$

To simplify this equation, the process is considered isentropic. This is valid if one assumes an ideal gas in an adiabatic process, resulting in a particle's constant entropy. Finally, we can assume a homentropic process in our uniform mean fluid, resulting in $ds = 0$.

Lastly, the speed of sound can be defined by $c = \sqrt{(\partial p/\partial \rho)_s}$, by which Equation 3.1.11 becomes Equation 3.1.12.

$$p = c_0^2 \rho \tag{3.1.12}$$

In which the average pressure and density approximate the speed of sound, i.e. $c_0 = c(\rho_0, p_0)$. Using this constitutive relation between pressure and density, Equation 3.1.10 can be rewritten into the convective wave equation in Equation 3.1.13.

$$\frac{1}{c_0^2}\left(\frac{\partial}{\partial t} + \nabla \cdot \mathbf{u}_0\right)^2 p' - \nabla^2 p' = 0 \tag{3.1.13}$$

Assuming that there is no mean flow ($\mathbf{u}_0 = 0$), the convective wave equation simplifies to the *d'Alembert wave equation*, given in Equation 3.1.14.

$$\frac{1}{c_0^2}\frac{\partial^2 p'}{\partial t^2} - \nabla^2 p' = 0 \tag{3.1.14}$$

This homogeneous second-order partial differential equation (PDE) describes wave propagation at the speed c_0. The solution of this equation depends on the initial conditions specified and the boundary conditions of the domain. Moreover, due to its linearity, solution superposition holds, and multiple waves can propagate throughout the medium without distorting each other [30, 40].

3.1.2 The inhomogeneous wave equation

In the derivation of Equation 3.1.14, it was assumed that no mass source term or external forces were present. Thereby, it solely describes the propagation of waves. However, a wave equation can be derived without these assumptions. The result is that the wave equation contains a source term $q(\mathbf{x}, t)$, shown in Equation 3.1.15.

$$\frac{1}{c_0^2}\frac{\partial^2 p'}{\partial t^2} - \nabla^2 p' = q \tag{3.1.15}$$

This source term allows for any deviation from the standard homogeneous wave equation. Therefore, adding sound sources in the medium is possible in regions where $q(\mathbf{x}, t)$ is non-zero. This results in a separated domain where q is zero, and wave propagation prevails and a domain where q is non-zero, where we deviate from wave propagation and can add a sound source to the domain.

Important to note is that a unique acoustic field can be determined when the source terms are known and initial and boundary conditions are well defined. However, the opposite is not valid.

Ffowcs Williams, an Emeritus rank Professor specialising in aeroacoustics, emphasised that a measured acoustic field has no unique source type and distribution. However, it is only possible to define a source distribution with the same measurable acoustic field as the real source. This idea is best explained when imagining a set of well-placed and calibrated surround sound speakers playing music as if there was a band in the room, even though there is not.

3.2 Quantification of sound level and annoyance

Sound, to most people, is coupled to the sensation of hearing. Either by listening to music, the noise coming from a vibrating radiator or the sirens from an emergency vehicle. The sensation of hearing is governed by pressure perturbations in the medium, interacting with the human eardrum (a thin diaphragm). These longitudinal pressure waves causing the disturbance propagate at $344.2\,\mathrm{m\,s^{-1}}$, the speed of sound for air at $20\,^{\circ}\mathrm{C}$ at $101\,325\,\mathrm{kPa}$.

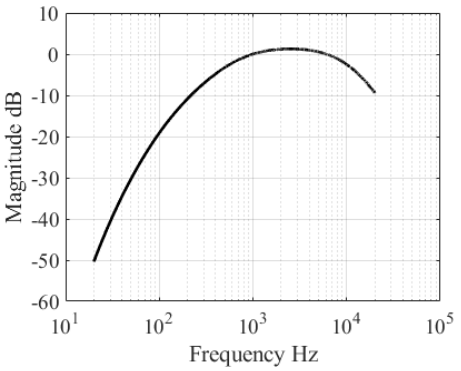

Figure 3.1: The frequency response of the A-Weighing filter.

The sound properties determine the response of a human listener. For example, not all frequencies are perceivable to the human auditory system. The human ear is most responsive to sound between 20 Hz and 20 kHz. At a speed of sound of $343\,\mathrm{m\,s^{-1}}$, this means that the wavelengths of interest lie between 17 m to 17 mm. Also, a human can hear sound waves with amplitudes as low as 20 µPa up to 200 Pa. The large frequency envelope and the significant dynamic range make the human ear a great addition to the human sensory system [40].

Due to the large perceivable range of sound wave amplitudes, it is common to express the ears' sensitivity on a logarithmic scale. This scale is referred to as the sound pressure level (SPL). This scale represents the sound level in dB with respect to a reference pressure. For almost all airborne applications, the reference pressure is chosen to be 20 µPa. The SPL is given in terms of the root mean square of the fluctuating pressure p_{rms} and this reference pressure p_{ref} by *Equation* 3.2.16.

$$\mathrm{SPL} = 20\log_{10}\left(p_{rms}/p_{ref}\right) \tag{3.2.16}$$

When considering the perceived noise by the human ear, the measured sound spectrum is often A-weighted. This sound filter approximates the sensitivity of a human ear to estimate how loud sound is perceived. Therefore, a weighing curve shown in Figure 3.1, is used. This weighing curve is defined in an international standard IEC 61672:2003 [41] and provides an insight into the perception of sound loudness.

Most often, reducing sound implies reducing annoyance from the observer's perspective, where the A-weighting of sound is of great importance. Therefore, A-weighing is applied to the results in section 7.2 and section 7.3. However, loudness is not the only factor impacting annoyance. Roughness, tonality, fluctuating strength, and sharpness are also significant in annoyance quantification [42]; however, these factors are not considered in this thesis.

Chapter 4

Sound source localisation and quantification

The results obtained from previous chapters function as stepping stones for understanding sound source localisation algorithms. Time-domain delay-and-sum or conventional beamforming methods can be employed when considering the localisation of sound sources in the far field. These algorithms process the signals received by microphone arrays to tell something about a sound wave's strength and angle of incidence. They are the backbone of many microphone arrays and are, therefore, discussed in this chapter.

4.1 Far-field acoustic beamforming

4.1.1 Time domain beamforming: delay and sum

Consider a microphone phased array containing a total of N microphones positioned at $\mathbf{x}_n$ in a homogeneous stagnant medium also containing a compact sound source at ξ, as shown in Figure 4.1. Each microphone can measure the pressure waves coming from this source. However, due to the difference in propagation distance between microphones, the signal obtained between microphones is shifted slightly.

The shift in signal can be taken advantage of in a method called delay-and-sum. In this method, the user defines an interrogation plane on which many points are defined. For each point in this grid, the wave arrival time is calculated to each microphone and the measured microphone signals are delayed to adjust for the difference. If a source is present in the location under consideration, constructive wave interference occurs between microphone signals. However, if no source is present at the point under consideration, the phase difference between microphones is random, and the sum of their amplitudes will be small. The phased array output for a point in the search grid is given by Equation 4.1.1.

$$z(t) = \frac{1}{N} \sum_{n=1}^{N} w_n p_n(t - \tau_n) \tag{4.1.1}$$

The time-shifted signals for each microphone p_n are weighted by w_n, summed, and normalised by the number of microphones N. The amount of delay is microphone-specific and proportional to the distance from the microphone to the interrogation point given by $\tau_n = \frac{r_n}{c_0}$, where c_0 is the average speed of sound in the medium and $r_n = |\mathbf{x}_n - \xi|$. The weights are often used to account for the decay in signal amplitude over the propagation distance.

Suppose one assumes that the pressure amplitude is inversely proportional to the propagation distance. The weights can then account for amplitude decay by choosing $w_n = 4\pi r_n$, and the equation can be rewritten into Equation 4.1.2.

$$z(t) = \frac{1}{N} \sum_{n=1}^{N} 4\pi r_n p_n(t - \tau_n) \tag{4.1.2}$$

This is the case for monopole-type sources in the free field, along with dipoles and quadrupoles in the acoustic far-field [43]. By plotting the amplitude of the delay-and-sum in a grid of interrogation points, an output map can be obtained in which possible sources can be localised and quantified (source map in Figure 4.1).

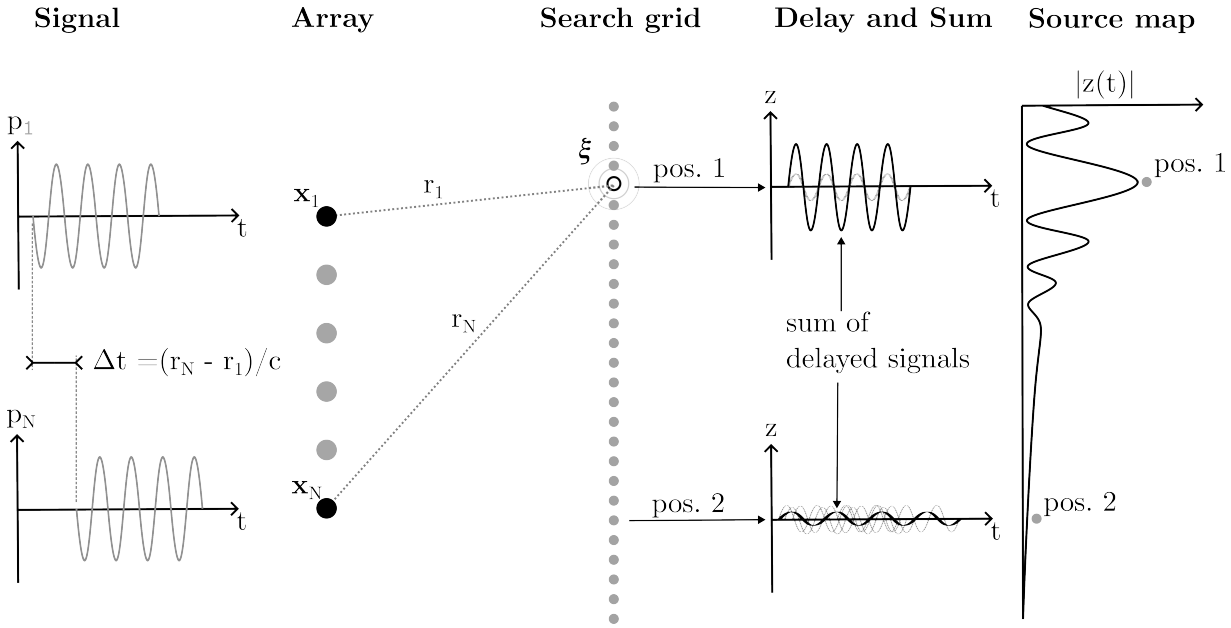

Figure 4.1: The delay and sum method with N microphones, with a source at position ξ.

4.1.2 Conventional beamforming in the frequency domain

Frequency-domain beamforming techniques can be used instead of beamforming in the time domain Using the frequency domain for beamforming allows the user to process the microphone signal and improve the performance of the beamformer.

Consider the time-series output of delay-and-sum beamforming, given in Equation 4.1.1. Using the Fourier transform, one can rewrite this formulation to Equation 4.1.3 in the frequency domain.

$$\tilde{z}(\omega) = \sum_{n=1}^{N} w_n \tilde{p}_n(\omega) e^{-i\omega\tau_n} \tag{4.1.3}$$

Where $\tilde{p}_n$ stands for the frequency domain equivalent of the time-series signal. One can see in this formulation how the response of each microphone is multiplied by a position-dependent phase shift and weighting factor. These terms are often reorganised into the signal part ($\tilde{p}_n$), originating from the microphone, and the phase shifting and weighting part ($w_n e^{-i\omega\tau_n}$). The formulation can then be rewritten into Equation 4.1.4.

$$\tilde{z}(\omega) = (w_n e^{-i\omega\tau_n})^{\dagger} \tilde{p}_n(\omega) \tag{4.1.4}$$

Where the † operator is used as the Hermitian conjugate operator. The vector ($w_n e^{-i\omega\tau_n}$) is often referred to as the steering vector, which is used for weighing and introducing a phase delay to the microphone signal. This steering vector is often defined in source vector components: $\frac{g_n^{\dagger}(\omega)}{\|g_n(\omega)\|^2}$, with $g_n = \frac{e^{-i\omega\tau_n}}{4\pi r_n}$. This eventually yields Equation 4.1.5.

$$\tilde{z}(\omega) = \frac{g_n^{\dagger}(\omega)}{\|g_n(\omega)\|^2} \tilde{p}_n(\omega) \tag{4.1.5}$$

Since the microphone signals are processed digitally, there is a finite number of frequency bins to consider, and the formulation discretises the frequency to yield Equation 4.1.6.

$$\tilde{z}(\omega_k) = \frac{g_n^{\dagger}(\omega_k)}{\|g_n(\omega_k)\|^2} \tilde{p}_n(\omega_k) \tag{4.1.6}$$

For the sake of readability the term (ω_k) is omitted, however, one should keep in mind that the parameters are still frequency dependent. The arrays frequency domain response can be used to determine the power of the signal, using the relationship in Equation 4.1.7

$$\begin{aligned} Z &= \frac{1}{2}|\tilde{z}|^2 \\ &= \frac{1}{2} \frac{(g_n^{\dagger}\tilde{p}_n)}{\|g_n\|^2} \frac{(g_n^{\dagger}\tilde{p}_n)^*}{\|g_n\|^2} \\ &= \frac{1}{2} \frac{g_n^{\dagger}(\tilde{p}_n \tilde{p}_n^{\dagger}) g_n}{\|g_n\|^4} \end{aligned} \tag{4.1.7}$$

The term $\frac{1}{2}(\tilde{p}_n\tilde{p}_n^\dagger)$ is named the cross-spectral matrix (CSM) and would eventually look like Equation 4.1.8. Each term in the CSM can be calculated using a window-averaged approach (Welch's method) to suppress noise in the microphone signals.

$$\mathrm{CSM}_{mn} = \frac{1}{2}\begin{bmatrix} \tilde{p}_1\tilde{p}_1^* & \cdots & \tilde{p}_1\tilde{p}_N^* \\ \vdots & \ddots & \vdots \\ \tilde{p}_N\tilde{p}_1^* & \cdots & \tilde{p}_N\tilde{p}_N^* \end{bmatrix} \tag{4.1.8}$$

The eventual equation to solve is given in Equation 4.1.9. Using conventional beamforming instead of time-domain delay-and-sum allows post-processing techniques to improve results. Microphone-phased arrays use this equation for far-field acoustic beamforming.

$$Z = g_n^\dagger \,\mathrm{CSM}\, g_n \tag{4.1.9}$$

4.2 Microphone phased arrays

Using the conventional beamforming technique described in subsection 4.1.2, some key performance indicators (KPI) and limits of microphone phased arrays can be discussed. This is done by assessing resulting beamforming maps based on a custom Python simulation of incoherent monopole sources. These criteria and KPIs are used during the design process of the ground-positioned microphone phased array.

4.2.1 The diffraction limit and Rayleigh's criterion

Consider a simple simulated monopole source whose position, frequency and amplitude are defined in a plane exactly 1 m from the array. The source is given unit source strength at all frequencies ($Q = 1\mathrm{Pa\,m}$) at $\xi = [0.3, 0.4, 1]\mathrm{m}$. The source location is shown by a red dot in Figure 4.2. The array consists of 48 microphones whose positions are of lesser importance. A rectangular search grid is constructed between -1 m and 1 m in both x and y with a resolution of 0.007 m in both directions.

One can readily see the source location due to a main lobe in the source map in the three figures of Figure 4.2. Along with this single main lobe, the rest of the domain is also non-zero and shows some artificial contributions to the map, even though there is no source in the rest of the domain. The resulting beamforming map of a single monopole source is known as the Point Spread Function (PSF) or beam pattern of the array [30, 44].

Spatial resolution

Spatial resolution is one of the performance indicators of an array and is determined by the width of the main lobe (beamwidth). The spatial resolution of the array is defined by the width of the main lobe at -3 dB of the peak, as is shown in Figure 4.3. Narrower peaks mean a better spatial resolution and an improved ability to spatially distinguish two closely spaced sound sources.

Using Rayleighs criterion for optical lenses, the resolution of an array can be related to the array diameter D, source wavelength λ and distance between the array and the source d as in

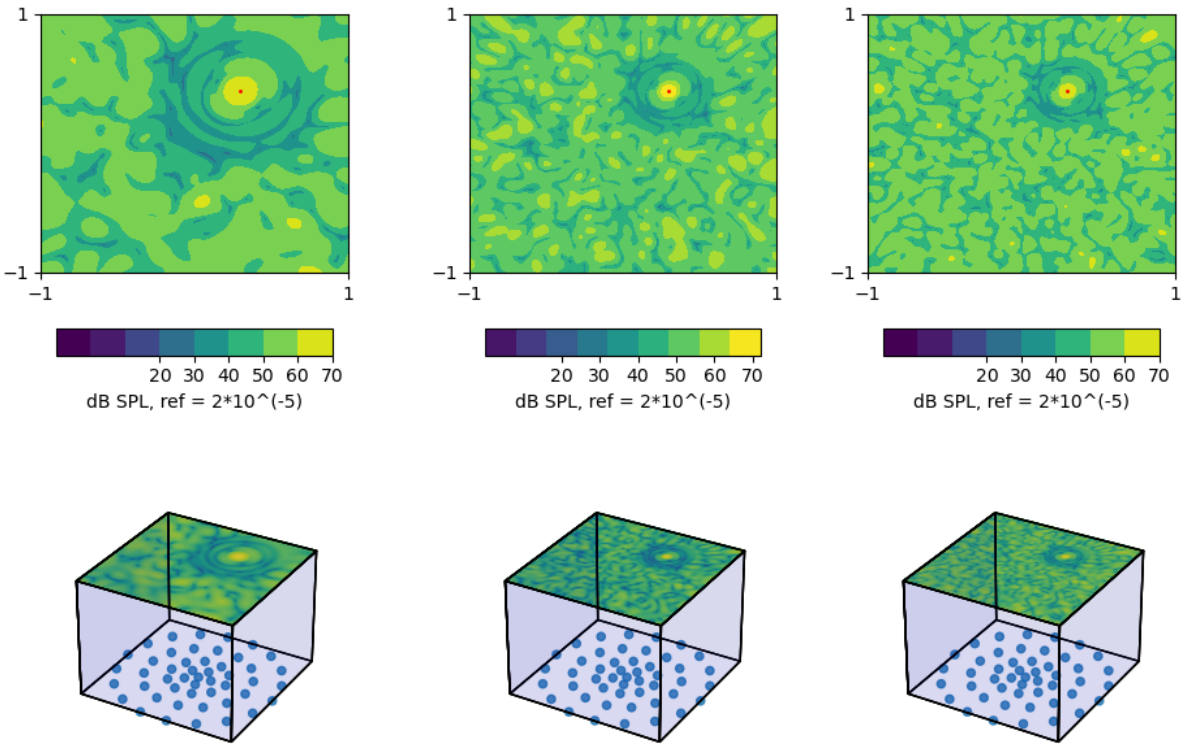

(a) Frequency of 2 kHz (b) Frequency of 3.5 kHz (c) Frequency of 4 kHz

Figure 4.2: A simulated output map for a single monopole at 1 m from the array.

Equation 4.2.10 [45]. One can observe that the spatial resolution diminishes with increasing wavelength (decreasing frequency) and increased distance between source and observer. Furthermore, increasing the array diameter improves the spatial resolution of the source map in an ideal situation according to Rayleigh's criterion.

$$beam\ width \sim \frac{\lambda d}{D} \tag{4.2.10}$$

Primary to peripheral beam ratio

Another quality-related parameter is the main-lobe-to-side-lobe ratio (MSL). This performance indicator describes the level differences between the primary and peripheral lobes. In the source map, the sources' position is given by the position of the main lobe. However, side lobes are present on the beamforming map. These artificial contributions make it challenging to distinguish possibly smaller sources in the domain from the side lobes of a more substantial source. Therefore, keeping the side lobe levels as low as possible is crucial when designing a microphone-phased array.

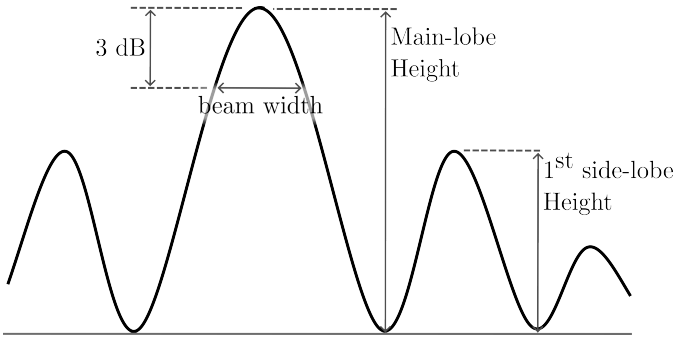

Figure 4.3: Characteristics of beam patterns.

4.3 Additional post-processing techniques

The simulated beamforming results in Figure 4.2 reflect an ideal situation. In reality, *coherence loss* and microphone noise can negatively impact the beamforming map. Furthermore, multiple main lobes might overlap, or a side lobe can interact with the main lobe of another source, making sound source quantification difficult. However, diagonal removal and source region integration techniques allow for the improvement of the source map and the accurate quantification of sound sources.

4.3.1 Diagonal removal

The cross-spectral matrix contains the auto-power elements of each microphone over its diagonal, i.e. $CSM_{mn} = \tilde{p}_m \tilde{p}_n^*$ for $m = n$. The auto-powers on the diagonal can contain incoherent signal power, such as microphone-dependent noise. The contribution of these elements to the output map is often detrimental in acoustic localisation [30]. Furthermore, since these elements have no phase information, they are not critical to the array's performance. Therefore, diagonal removal is often performed by removal of these elements.

This technique is also useful when considering coherence loss. The consequence of coherence loss for the CSM is decreased levels of cross-power elements and an increasing contribution of the auto-powers, reducing the quality of the source map.

4.3.2 Source region integration

The location of a sound source is only part of the sound's characterisation. In general, the source levels are also of interest. For a single well-resolved monopole source, the monopole's power corresponds to the maximum level in the beamforming map. However, a single monopole source is a rare occurrence in reality. When multiple sources are present in the domain, a convolution of numerous PSFs is observed. Furthermore, coherence loss between microphones can result in difficulties with sound source quantification due to the reduction and broadening of the main lobe. This can make the quantification of sound source power challenging.

To overcome this and normalise the results, a method called *source region integration* can be employed [46]. The technique integrates part of the source map $Z_{h,exp}$ and normalises it by simulating a single monopole source in the centre of the integration region. Since the source map is discretised in space, the integration becomes a summation over points h, as in Equation 4.3.11 [30].

$$P_{exp} = \sum_{h=1}^{H} Z_{h,exp} \cdot \frac{P_{sim}}{\sum_{h=1}^{H} Z_{h,sim}} \tag{4.3.11}$$

Where the power of the simulated monopole is given by P_{sim} and the sound source power in the source map by P_{exp}, furthermore, $\sum_{h=1}^{H} Z_{h,sim}$ and $\sum_{h=1}^{H} Z_{h,exp}$ denote the integration of the simulation region and experimental region, respectively. The number of grid points in the integration region is denoted by H. As long as the integration area does not contain significant contributions from sources outside the area and the sources are assumed uncorrelated, this method produces accurate source levels, even in the presence of coherence loss [30].

4.4 Implementation and Validation of Conventional Beamforming in Python

The Python simulation of incoherent monopole sound sources is used for a preliminary performance assessment of microphone arrangements. With this performance assessment, a microphone arrangement is designed in section 5.1. The code is, therefore, briefly explained.

The code initiates the domain with a set of incoherent monopole sources along with some observers. The frequency response of a microphone due to a simple source is given by Green's free-field function in Equation A.2.18. This is used to calculate the frequency response at all observers $\mathbf{x}_n$ from a source at ξ with strength Q, given by Equation 4.4.12.

$$\tilde{p}_n = \frac{Q}{4\pi|\mathbf{x}_n - \xi|} e^{-ik|\mathbf{x}_n - \xi|} \tag{4.4.12}$$

The responses of all observers due to a single source are used to construct a cross-spectral-matrix (CSM), as given by Equation 4.4.13. The index s denotes a CSM specific to a single source.

$$\mathrm{CSM}_{mn,s} = \frac{1}{2} \tilde{p}_{m,s} \tilde{p}^*_{n,s} \tag{4.4.13}$$

After constructing the CSM for each source individually, the CSMs for a specific frequency are summed up. This is done to simulate the incoherent nature of sources in the domain. The importance of this approach becomes apparent when mathematically describing the CSM for many sources in the domain. Consider dealing with coherent sources having a constant phase difference. The microphone response is a sum of both source responses at the observer, i.e. $\tilde{p}_n = \tilde{p}_{n,1} + \tilde{p}_{n,2}$, since any change in response is coherent between sources. Here, the index after the subscript denotes the contribution of a specific source. When using this in the description of the CSM, i.e. Equation 4.4.13, Equation 4.4.14 is obtained.

$$\mathrm{CSM}_{mn} = \frac{1}{2}(\tilde{p}_{m,1} + \tilde{p}_{m,2})(\tilde{p}^*_{n,1} + \tilde{p}^*_{n,2}) = \frac{1}{2}(\tilde{p}_{m,1}\tilde{p}^*_{n,1} + \tilde{p}_{m,1}\tilde{p}^*_{n,2} + \tilde{p}_{m,2}\tilde{p}^*_{n,1} + \tilde{p}_{m,2}\tilde{p}^*_{n,2}) \quad (4.4.14)$$

The terms $\tilde{p}_{m,1}\tilde{p}^*_{n,2}$ and $\tilde{p}_{m,2}\tilde{p}^*_{n,1}$ imply a coherence between sources. These terms should be avoided when simulating incoherent sources. To avoid this, multiple CSMs are constructed for each source separately and are sequentially summed up for each frequency as in Equation 4.4.15.

$$\mathrm{CSM}_{mn} = \sum_{s=1}^{S} \mathrm{CSM}_{mn,s} = \sum_{s=1}^{S} \frac{1}{2}\tilde{p}_{m,s}\tilde{p}^*_{n,s} \quad (4.4.15)$$

Similarly, with two incoherent sources, this simplifies to Equation 4.4.16.

$$\mathrm{CSM}_{mn} = \frac{1}{2}(\tilde{p}_{m,1}\tilde{p}^*_{n,1}) + \frac{1}{2}(\tilde{p}_{m,2}\tilde{p}^*_{n,2}) = \frac{1}{2}(\tilde{p}_{m,1}\tilde{p}^*_{n,1} + \tilde{p}_{m,2}\tilde{p}^*_{n,2}) \quad (4.4.16)$$

Compared to equation Equation 4.4.14, this does not show the cross-terms, thereby simulating completely incoherent sources. The complete CSM then looks like Equation 4.4.17.

$$\mathrm{CSM}_{mn} = \sum_{s=1}^{S} \frac{1}{2} \begin{bmatrix} \tilde{p}_{1,s}\tilde{p}^*_{1,s} & \cdots & \tilde{p}_{1,s}\tilde{p}^*_{N,s} \\ \vdots & \ddots & \vdots \\ \tilde{p}_{N,s}\tilde{p}^*_{1,s} & \cdots & \tilde{p}_{N,s}\tilde{p}^*_{N,s} \end{bmatrix} = \frac{1}{2} \begin{bmatrix} \tilde{p}_1\tilde{p}^*_1 & \cdots & \tilde{p}_1\tilde{p}^*_N \\ \vdots & \ddots & \vdots \\ \tilde{p}_N\tilde{p}^*_1 & \cdots & \tilde{p}_N\tilde{p}^*_N \end{bmatrix} \quad (4.4.17)$$

After the CSM is constructed, the source vector components are calculated for all observers for a specific search point $\mathbf{y}$; $g_n = \frac{1}{4\pi|\mathbf{x}_n - \mathbf{y}|} e^{-ik|\mathbf{x}_n - \mathbf{y}|}$. The CSM and steering vectors are used to perform the calculation in Equation 4.1.9 and produce an output at a specific frequency in a specific interrogation point $\mathbf{y}$. This calculation is performed multiple times, changing the steering vector for each search grid point to obtain a complete source map at a specific frequency.

With this method, some benchmark tests were performed. Results thereof are used in subsection 4.2.1. A brief validation of the benchmark results can show the correct functioning of the code.

Firstly, in subsection 4.2.1 the source was placed at $\xi = [0.3, 0.4, 1]$m. Looking at Figure 4.2, the source position can be accurately retrieved from the resulting beamforming map.

Furthermore, the source strength was of unit magnitude (i.e. Q =1 Pa m in Equation 4.4.12). The beamforming map attains its maximum value when $\mathbf{y}$ coincides with ξ. At this point, the source map level is given by $Z_{\mathbf{y}=\xi} = \frac{1}{2}|\tilde{p}|^2$. However, the results are presented in SPL for d =1 m from the source by Equation 4.4.18. Therefore, the maximum level in the output map should be 68.985 dB. The simulation results in a maximum level of 68.9849 dB. Therefore, the frequency domain simulation for incoherent monopole sources seems to function correctly and can be used in the design of a microphone arrangement.

$$\mathrm{SPL} = 20\log_{10}\left(\frac{\sqrt{Z}}{4\pi d}\frac{1}{p_{ref}}\right) \quad (4.4.18)$$

Additionally, three simulations with two, three, and four incoherent sources are shown in Figure 4.4. Figure 4.4a shows two sources at 1 m distance radiating sound at 2 kHz. One source has unit source strength (top right), and the other Q =0.8 Pa m. Secondly, Figure 4.4b shows three sources at 1 m radiating sound at 2 kHz. An additional source is added to the domain (top left) with a source strength of 0.6 Pa m. The side lobe levels of the larger sources make it difficult to distinguish the less powerful source. Lastly, Figure 4.4c shows an experimental result during the microphone arrangement design in section 5.1. Four unit strength sources were added to the domain at 3 m. This beamforming map shows the source at 4 kHz.

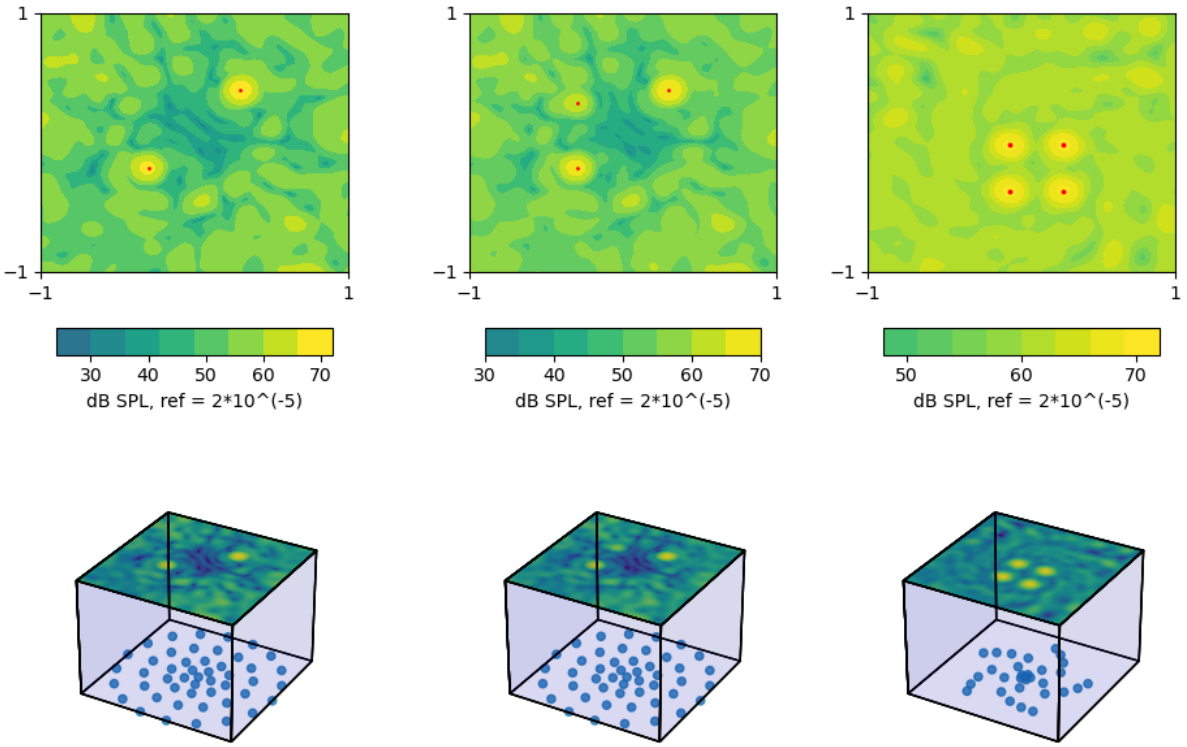

(a) (b) (c)

Figure 4.4: Resulting beamforming maps using Python to simulate conventional beamforming for incoherent sources.

Chapter 5

Design of a microphone phased array for UAV fly-over measurements

5.1 Microphone arrangement design

The microphone arrangement significantly impacts the array's performance, especially aperture size and inter-microphone distances. Prime and Doolan have conducted a performance assessment for many different microphone arrangements over a vast range of frequencies in *"A comparison of popular beamforming arrays"* [47]. This thesis will, therefore, use the results of Prime and Doolan and will not give a thorough analysis of an optimal microphone arrangement.

A dual setup was created featuring a central frame and microphone pucks to keep the array transportable and allow for flexible microphone placement. Furthermore, this allows for microphone arrangement optimisations for different types of sound sources. An array diameter of 3 m was chosen to have sufficient spatial accuracy to distinguish closely spaced rotors. The central frame consists of 31 microphones in an Underbrink pattern. The Underbrink pattern is, according to Prime and Doolan, a good compromise between spatial resolution and dynamic range [47]. This Underbrink pattern is extended by a multi-spiral design of 25 microphones. Furthermore, the microphone positions can be seen in Figure 5.1, where the central frame in the Underbrink arrangement is highlighted in red, while the multi-spiral is given a blue hue.

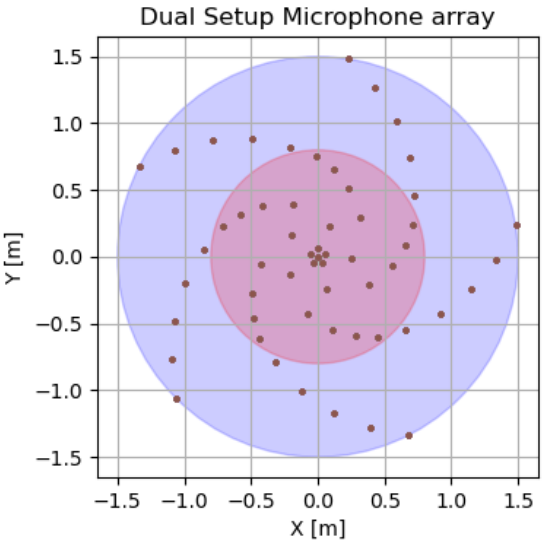

Figure 5.1: The microphone positions of the Underbrink-Multi spiral design. The Underbrink pattern is made with, r_0 =0.06 m, r_{max} =0.75 m, N_a =5, N_m =6, and $\nu = 5\pi/16$. Furthermore the Multi-spiral design is made with, r_0 =0.85 m, r_{max} =1.5 m, N_a =5, N_m =5, and $\nu = \pi/16$. The region in red shows the Underbrink pattern, while blue depicts the multi-spiral design.

The microphone positions of the Underbrink array are determined by Equation 5.1.1 and Equation 5.1.2. Furthermore the microphone arrangement for the multi-spiral extensions are determined by Equation 5.1.3, Equation 5.1.4, and Equation 5.1.5. In these equations, $i = 1, ..., N_a$ and $j = 1, ..., N_m$. Furthermore, r_0 is the minimum radius, while r_{max} is the maximum. N_a is the number of spiral arms, and N_m is the number of microphones per arm. Also, ν is a parameter describing the curvature of the arm. The exact microphone positions are added to the appendix in Figure A.3.8.

$$r_{i,j} = \sqrt{\frac{2j-3}{2N_m-3}} r_{max} \qquad \text{with} \qquad r_{i,1} = r_0 \tag{5.1.1}$$

$$\theta_{i,j} = \ln(\frac{r_{i,j}}{r_0})\tan(\nu) + \frac{i-1}{N_a}2\pi \tag{5.1.2}$$

$$l_j = \Big(\frac{j-1}{N_m-1}\Big) l_{max} \qquad \text{with} \qquad l_{max} = \frac{r_0\sqrt{1+\cot^2(\nu)}}{\cot(\nu)}\Big(\frac{r_{max}}{r_0} - 1\Big) \tag{5.1.3}$$

$$\theta_{i,j} = \tan(\nu)\ln\Big(1 + \frac{l_j}{r_0\tan(\nu)\sqrt{1+\cot^2(\nu)}}\Big) + \frac{i-1}{N_a}2\pi \tag{5.1.4}$$

$$r_{i,j} = r_0 e^{\cot(\nu)\theta_{i,j}} \tag{5.1.5}$$

The performance of this array was evaluated by its PSF and the simulation of multiple closely spaced incoherent sound sources. The output maps were assessed on spatial accuracy, SNR, and MSL ratio. One of the results is given in Figure 4.4c.

5.2 Hardware design and considerations

The phased array's design focuses on transportability, producibility, reliability, and robustness. Furthermore, hardware costs were kept to a minimum to allow for cheap replacements should anything fail.

The Underbrink arrangement is constructed using a circular central plate with five connecting arms that attach to the central plate. Lasercut 16 mm multiplex wood and 6 mm PMMA sheet was used in constructing these pieces. The wood serves as the mounting panel on which the microphones are screwed, while the PMMA sheet is added to the top for increased frame stiffness. 16 mm spacers were added beneath the wooden panel to lift the central plate and the connecting arms off the ground. This was done to reduce the chance of moisture damage to the microphones should the setup be laid on humid ground.

The outer microphones, placed on pucks, are constructed with the same 16 mm multiplex and 6 mm PMMA. However, the PMMA is added to the bottom of the wood to reduce the chances of moisture damage to the electronics. In the final design, a 120 mm diameter steel disc (3 mm thick) was added to the bottom of each puck to keep it from moving once placed. Furthermore, windshields were added by mounting 4 mm thick open-cell foam above the microphone ports.

Lastly, a stencil was constructed from 1 mm steel to lay the outer microphones in place effortlessly. A 16 mm multiplex frame was glued to this steel to keep it from bending. Figure 5.2 shows the computer-generated design used to produce the necessary files for the laser cutter.

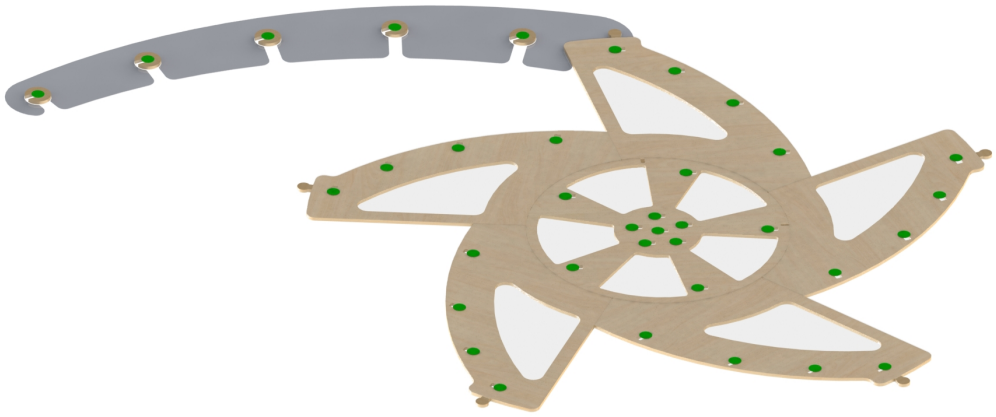

Figure 5.2: The rendered array design shows the central plate, a single arm of the outer microphones, and a stencil to lay these pucks in a multi-spiral arrangement.

5.2.1 MEMS Microphone decision and considerations

Many acoustic cameras use expensive analogue microphones. Furthermore, the signals are sampled and converted (analogue to digital) by costly data acquisition systems. In such setups, the costs of the array increase significantly with the increasing number of microphones. However, small PCB-mounted systems prove reliable counterparts to expensive condenser microphones due to recent developments in MEMS (Microelectromechanical system) microphone technology. Therefore, the decision was made to use PCB-mounted analogue MEMS microphones with additional onboard signal processing and voltage regulation.

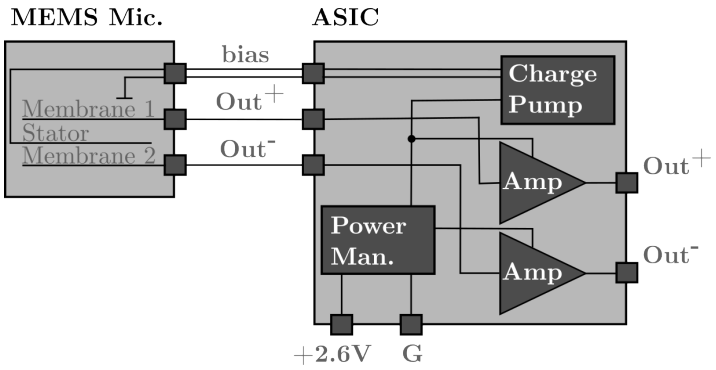

Figure 5.3: A schematic representation of the Infineon IM73A135V01 analogue MEMS microphone. The MEMS is shown on the left, while the Application Specific Integrated Circuit (ASIC) is given on the right.

The Infineon IM73A135V01 was chosen as the microphone. This analogue MEMS microphone has an IP57-rated design and is adequately robust for outdoor use. These microphones can function after a 2 h submersion in 1 m deep water and are furthermore dust-resistant. They should, therefore, be able to function in the outdoor environment without the risk of microphone damage.

Furthermore, these microphones were chosen based on their outstanding performance compared to alternatives. Along with a signal-to-noise ratio of 73 dB (A-weighted), it boasts a 135 dB (SPL) acoustic overload pressure level (AOPL), allowing it to be used in boisterous conditions. Furthermore, it has a flat frequency response from 20 Hz up to 18 kHz and an omnidirectional pickup pattern. Due to their tight manufacturing tolerances, the phase differences are minor. Lastly, these microphones are sensitivity calibrated to within ±1 dB of each other. A schematic representation of the microphone is given in Figure 5.3. The IP-rated design and outstanding performance make this analogue microphone an excellent choice for an outdoor acoustic camera.

5.2.2 PCB design aspects

The PCB design focused on device reliability, robustness, signal precision, and ease of use. For an in-depth electrical schematic, the reader is referred to the appendix (Figure A.3.9). In contrast, a simplified schematic of the PCB layout and signal processing is given in Figure 5.5.

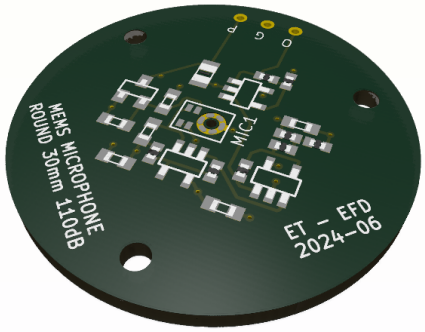

Figure 5.4: Shows the constructed PCB with the MEMS microphone. Components are hidden to show the layout and traces on the board.

A three-stage amplifier provides signal amplification. These stages amplify the signal by a factor of 24 while keeping it from clipping at 0 V and 12 V. This reduces the relative amount of noise picked up between the PCB and the DAQ, improving the reproducibility of measurements. This is especially useful since the data acquisition system should be placed far from the microphone array to avoid noise contamination. Hence, long cables are necessary. Furthermore, amplifying the signal means that the data acquisition system uses more bits in analogue to digital conversion, making signal reconstruction more accurate.

Furthermore, the PCB is powered using 12 V. This 12 V is used by both the microphone and the amplifiers. However, a step-down regulator powers the microphone, which only requires 2.6 V. This regulator also functions as a buffer if the PCB input voltage is not precisely 12 V (due to noise or offsets). This improves the reliability and robustness of these PCBs.

A three-pin header was installed. This was done for the PCB's ease of use since a simple female connector slides on easily. The header pins are labelled P (power), G (ground), and O (output).

Finally, the designed Infineon microphone PCBs could not be used due to manufacturing delays. These were exchanged with a microphone board from Sparkfun (ICS-40180) with an AOPL of 124 dB, an SNR of 65 dB (A-weighted), and a flat frequency response between 60 Hz to 20 000 Hz. These microphones were powered using a benchtop power supply, providing a stable 3.2 V. For the measurements, 56 Sparkfun microphones were powered on 224 mW.

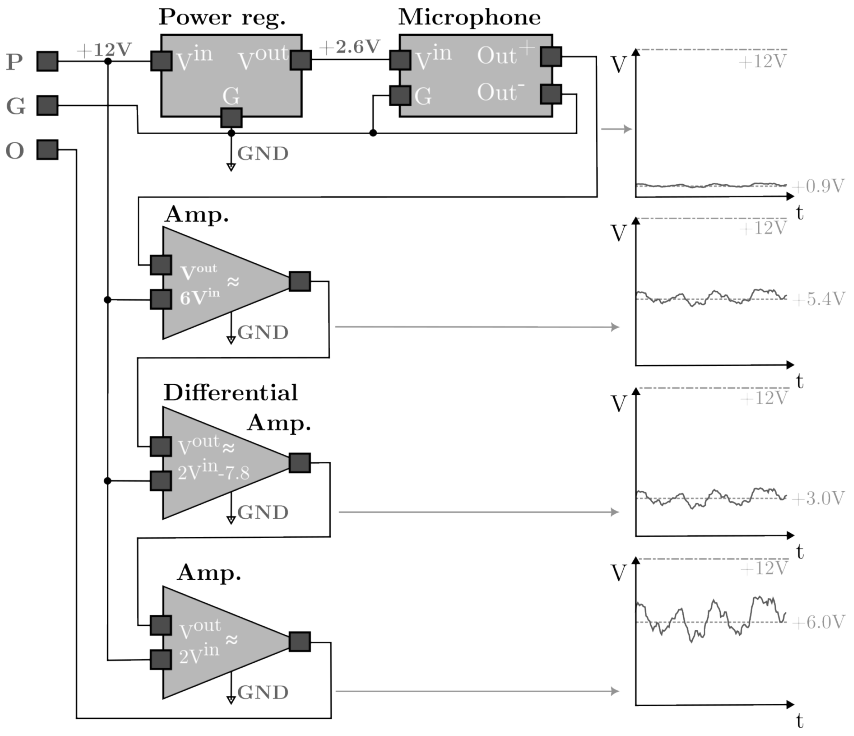

Figure 5.5: A schematic representation of PCB components and signal processing.

5.3 Data acquisition system

The analogue signals from the microphones are transported over 5 m long shielded copper cables. These three-core cables supply the PCBs with power, ground, and a data cable. These cables connect to multiple 16 channel distribution boxes, which were already available. These distribution boxes only allowed for three core cables, limiting the use of the microphone's differential output. In a redesign, these boxes should provide enough cable cores for differential signals. Sequentially, the distribution boxes are connected to the data acquisition system. The complete setup is shown in Figure 5.6 where a power supply and laptop are also given for the necessary power and data processing.

Data acquisition and processing are performed on a National Instruments NI PXIe-1073 chassis equipped with four NI PXI-4499 Dynamic Signal Acquisition cards. This data acquisition system is capable of simultaneously sampling 64 analogue channels at 204.8 kHz, with a 24 bit ADC. For this purpose, it uses its First In, First Out buffer. Since there are a total of 56 microphones in the set-up, this should be more than enough.

The obtained data is processed in real-time using LabView and is written to a *.tdms* file for post-processing steps. The LabView application, which was visually programmed, performs real-time conventional beamforming for demonstration purposes. The program also calculates the power spectral density of a chosen microphone. This is done to give the user real-time insight into the performed measurement, with which a new measurement can be set up in a matter of seconds. However, due to the visual programming environment of LabView, the code is complex and challenging to illustrate effectively. Therefore, it is not given in this report.

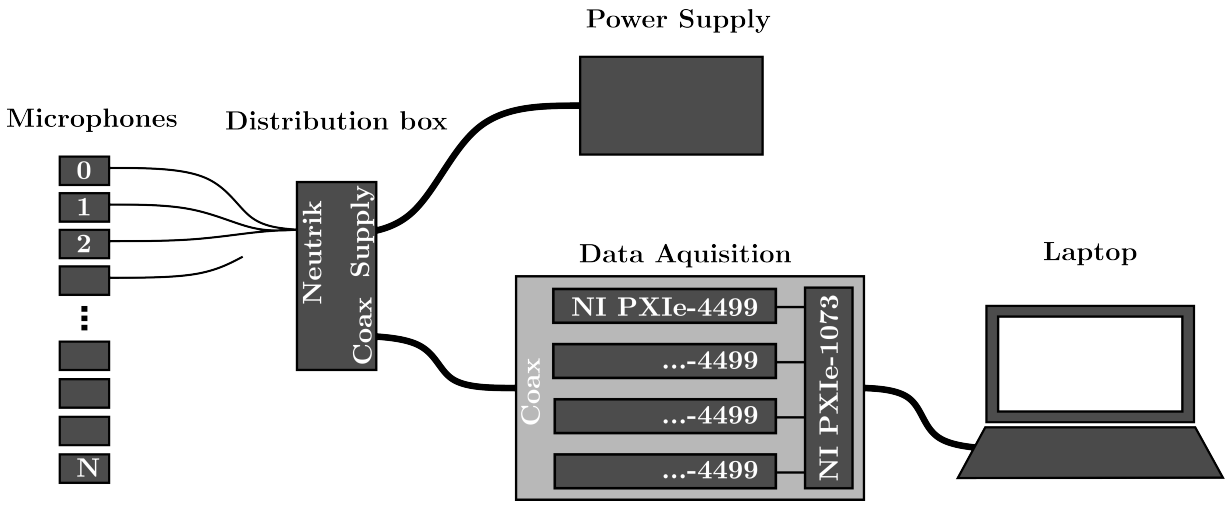

Figure 5.6: A schematic overview of the data acquisition setup. The data is read from the FIFO buffer and is sequentially processed via LabView.

Chapter 6

Calibration of the microphone positions using an acoustic GPS

Acoustic beamforming algorithms rely on the user's knowledge of the exact microphone positions, which are used to construct the steering vectors. A deviation between the expected and actual acoustic microphone positions, a combination of physical position and phase delay, can significantly reduce the quality of the output map. However, it can be challenging to position microphones accurately for outdoor measurements. Therefore, it is crucial to calibrate the microphone positions after placement.

Some literature suggests using theodolites to determine the positions of the microphones [48] accurately. However, this is a time-consuming and laborious effort. Furthermore, this method only results in the microphone's physical position without considering system-related signal delays. However, research has been ongoing on so-called acoustic GPS modules [49, 50]. These aGPS modules could serve as an efficient in-situ calibration technique to retrieve the acoustic positions of many microphones simultaneously. This can be useful not only during beamforming measurements but also for any measurement that requires accurate microphone positions (e.g. directivity measurements). Therefore, an aGPS could be an efficient position calibration method for large microphone-phased arrays.

6.1 The acoustic GPS

Similarly to the regular GPS method, the aGPS method uses the distance between sources and observers to tell something about the observer's position. An acoustic GPS's sources are loudspeakers, while the receivers are the microphones. Lauterbach et al. describe a minimisation problem, which determines the acoustic position of each target microphone independently [49]. They mention the need for a large panel with at least five loudspeakers behind converging ducts (similarly to Figure A.3.4a) and a reference microphone.

This method is improved upon by Ernst et al. [50] with their self-calibrating acoustic GPS (SC-aGPS) algorithm. They consider the uncertainty of the speakers and reference microphone locations. They also solve the problem for a system as a whole (instead of solving it for every microphone independently). Furthermore, they add a secondary reference microphone for the

accurate calculation of the speed of sound. Both these methods are programmed in MatLab. However, the following sections will discuss the SC-GPS algorithm used in this thesis.

6.1.1 The SC-aGPS algorithm

The calculation of the acoustic microphone positions using the SC-aGPS algorithm is performed in four separate steps. Performing these steps results in the microphones' acoustic positions in the aGPS frame of reference.

1. The five sources are powered in sequence, and all microphone signals (reference and target microphones) are recorded simultaneously.
2. The time delay between the reference microphones and each target microphone is calculated and stored.
3. The speed of sound is determined by the time delay between the reference microphones when one of the speakers was powered.
4. The time delays are converted to distances using the speed of sound and are used to obtain the acoustic positions in a non-linear set of equations. These equations are solved in a least square minimisation problem.

Because step two and three need to calculate the time delay between two signals, the method to obtain this delay is discussed first.

Calculation of a time delay between two signals via the frequency domain

After the measurements have been performed, all signals are filtered first. All unexcited frequencies (of the loudspeaker) are damped using a bandpass filter from 4 kHz to 15 kHz with a damping of 150 dB per decade. Then, using Welch's method, an averaged cross-correlation function is calculated via the frequency domain.

The delays between two microphone signals are calculated via the frequency domain using the convolution theorem. This theorem states that the Fourier transform of a convolution of two signals is equivalent to the product of the Fourier-transformed signals, i.e. $\mathcal{F}(p_1 * p_2) = \mathcal{F}(p_1) \cdot \mathcal{F}(p_2)$, where $\mathcal{F}(\cdot)$ is the Fourier transform and $*$ the convolution operator. However, the correlation function is used to determine the time delays. For this purpose, one of the signals is conjugated and time-reversed. This transforms the convolution into a correlation function, i.e. $\mathcal{F}(p_1(t) * p_2(-t)^*) = \mathcal{F}(p_1(t)) \cdot \mathcal{F}(p_2(t))^*$. For real-valued signals, one can drop the conjugate in the left-hand term, resulting in $\mathcal{F}(p_1(t) * p_2(-t)) = \mathcal{F}(p_1(t)) \cdot \mathcal{F}(p_2(t))^*$. This equation's inverse Fourier transform finally results in the cross-correlation function in Equation 6.1.1.

$$R_{p_1,p_2}(t) = p_1(t) * p_2(-t) = \mathcal{F}^{-1}\Big(\mathcal{F}(p_1(t)) \cdot \mathcal{F}(p_2(t))^*\Big) \tag{6.1.1}$$

The maximum of the cross-correlation function gives the time delay of the two signals. However, to accurately obtain the position of this maximum, the signals are oversampled at 200 kHz and a spline interpolation is used in the region of the maximum [50].

Calculation of the speed of sound

The speed of sound is necessary to accurately determine the acoustic positions of the microphones. Furthermore, the calculated speed of sound is used in the beamforming measurements, with the construction of the steering vectors.

Two reference microphones are used on the plate to determine the speed of sound. This is done by calculating the delay between the reference microphones when one of the speakers is powered. This delay can then be used in calculating the speed of sound, as in Equation 6.1.2.

$$c_0 = \frac{|\mathbf{x_{ref,1}} - \mathbf{y_n}| - |\mathbf{x_{ref,2}} - \mathbf{y_n}|}{\Delta t_{ref}} \tag{6.1.2}$$

Calculation of the microphone position

Then, the minimisation function can be set up for Ernst's self-calibrated aGPS algorithm. The following system of equations is of interest here, given in Equation 6.1.3.

$$F_{i,j,k}(\mathbf{x}_i, \mathbf{x}_{ref,j}, \mathbf{y}_k) = |\mathbf{y}_k - \mathbf{x}_i| - |\mathbf{y}_k - \mathbf{x}_{ref,j}| - c_0 D_{ijk} \tag{6.1.3}$$

In this equation, $\mathbf{y_k}$, $\mathbf{x_i}$, and $\mathbf{x_{ref,j}}$ denote the positions of the tweeter, the target microphone, and the reference microphone, respectively. This equation is the basis for the optimisation problem shown in Equation 6.1.4.

$$\min_{\substack{\mathbf{x}_i \\ \mathbf{x}_{ref,j} \\ \mathbf{y}_k}} \sum_{i=1}^{N_t} \sum_{j=1}^{N_r} \sum_{k=1}^{N_s} F_{i,j,k}(\mathbf{x}_i, \mathbf{x}_{ref,j}, \mathbf{y}_k)^2 \tag{6.1.4}$$

In this case, N_t, N_r, and N_s are the number of target microphones, reference microphones, and speakers, respectively. The optimisation algorithm should be constrained close to the initial guess of positions, especially since the locations of the loudspeakers and reference microphones on the aGPS panel are measured with a coordinate measurement machine with a tolerance of 0.03 mm [51]. Therefore, a set of constraints is set up to force the algorithm to look for an optimum in the neighbourhood of the initial positions, given in Equation 6.1.5. In this equation, E_i, E_j, and E_k specify the maximum expected error for the target microphone, reference microphone, and speakers, respectively.

$$\begin{aligned} |\mathbf{x}_i - \hat{\mathbf{x}}_i| &\leq E_i & i &= 1, ..., N_t \\ |\mathbf{x}_{ref,j} - \hat{\mathbf{x}}_{ref,j}| &\leq E_j & j &= 1, ..., N_r \\ |\mathbf{y}_k - \hat{\mathbf{y}}_k| &\leq E_k & k &= 1, ..., N_s \end{aligned} \tag{6.1.5}$$

This function is minimised using the interior-point method in MatLab and outputs the target microphone coordinates in the aGPS frame of reference.

6.1.2 Transformation of the reference frame

The previous calculations are performed in the aGPS coordinate frame, while the positions of the target microphones need to be known in the acoustic camera frame of reference. This coordinate transformation is performed in Equation 6.1.6.

$$\mathbf{x}_{i,\text{cam}} = \mathbf{R}\mathbf{x}_{i,\text{gps}} + \mathbf{t} \tag{6.1.6}$$

Where $\mathbf{x}_{i,\text{cam}}$ and $\mathbf{x}_{i,\text{gps}}$ are the microphone coordinates in the acoustic camera and the aGPS frame, respectively, $\mathbf{R}$ is the orthogonal rotation matrix, and $\mathbf{t}$ is a translation vector. It is shown by Gander [52] that $\mathbf{t}$ is the vector between the centres of gravity of the point clouds $\mathbf{x}_{i,\text{cam}}$ and $\mathbf{x}_{i,\text{gps}}$. They can, therefore, be calculated directly. However, obtaining $\mathbf{R}$ has to be done by another least-squares minimisation. Eventually, this yields the calculated microphone positions in any reference frame.

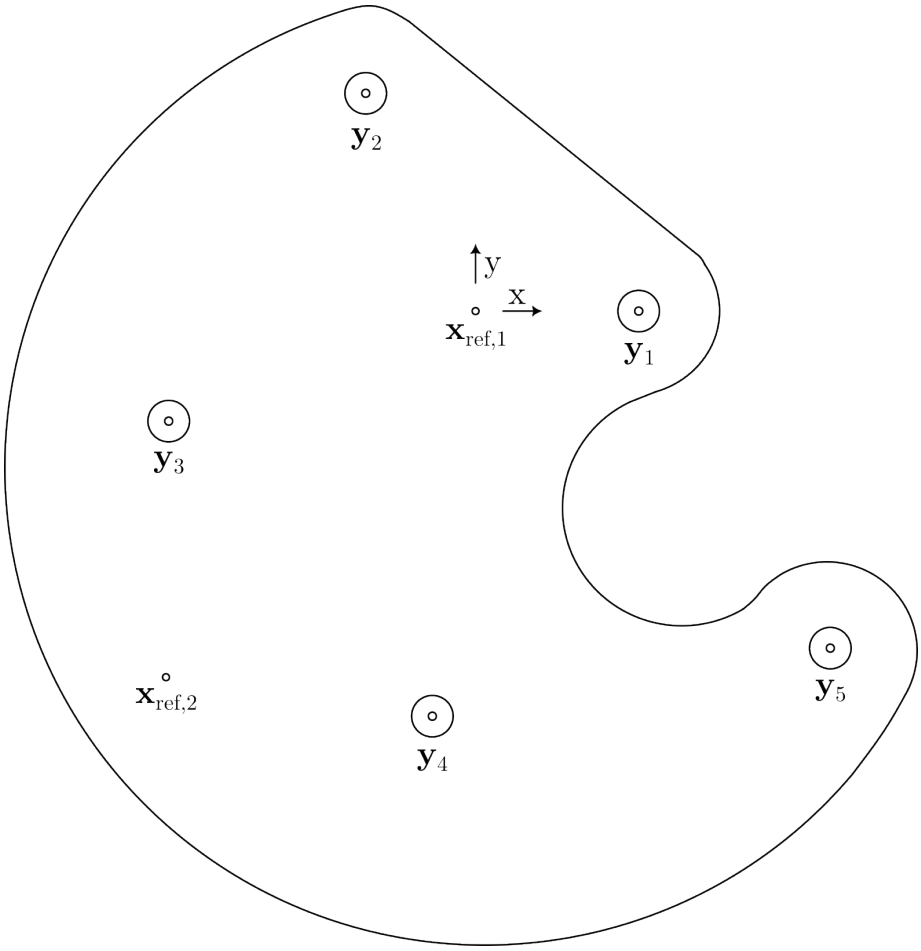

Figure 6.1: The arrangement of microphones and loudspeakers, looking at the front of the aGPS panel. The assumed and measured coordinates of the microphones and loudspeakers are given in Table A.3.3 and Table A.3.4, respectively.

6.2 Acoustic GPS module design

The constructed aGPS panel, shown in Figure 6.2, is constructed from a circular plate of 20 mm multiplex, with a diameter of 1.3 m. A heavy plate was chosen to limit vibrations due to a powerful mounted speaker. Selecting a lighter panel would make the setup more manageable. However, this could also increase the chance of speaker sound vibrating through the wood to the reference microphones. This would result in unusable measurements for the aGPS algorithm since it assumes that the sound propagates through the air, not the wood.

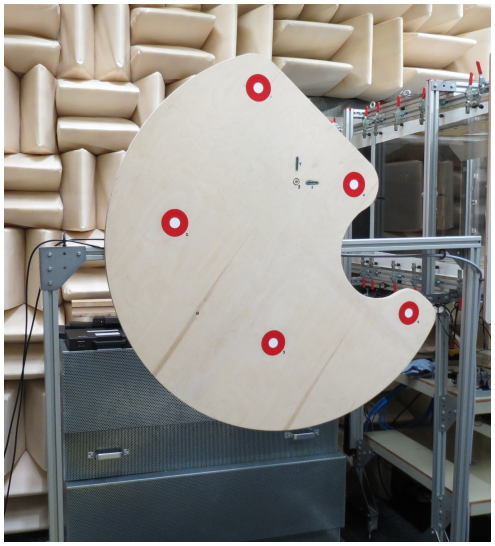

Figure 6.2: The constructed aGPS on the aluminium framing, showing the positions of the speakers by the red circles.

Two GRAS 40PH-10 microphones were mounted to the panel as reference microphones. These microphones have a flat frequency response between 10 Hz until 20 kHz and an AOPL of 135 dB (SPL). This frequency range and high AOPL ensure their compatibility with powerful loudspeakers. These reference microphones are placed far apart, so any mounting error is relatively small compared to the distance between microphones.

Five hi-fi loudspeakers (VISATON 8005) were mounted behind 3D-printed converging ducts to simulate monopole sound sources. These loudspeakers were chosen based on their flat frequency response between 1.5 kHz and 22 kHz, mostly coinciding with the usable frequency range of the reference microphones. Also, their power limit of 100 W makes them powerful sound sources, especially useful for outdoor use. The arrangement of loudspeakers is based on a Dougherty-log spiral and can be seen in Figure 6.1. Power is provided by a 40 W sound amplifier, built into a custom switch box to turn the loudspeakers on and off.

After mounting the loudspeakers and microphones to the panel, the ports were measured by a coordinate measurement machine (FARO Quantum LLP) [51]. This is done to improve the aGPS algorithm, which requires an accurate initial guess of the microphone (both targets and references) and loudspeaker positions. Lastly, the entire panel was mounted to an aluminium frame.

6.3 aGPS experimental validation

6.3.1 Phase calibration of CAE antenna

The accuracy of the aGPS calibration method is assessed using the CAE microphone array. Since this array has known microphone positions, any deviations can be attributed to aGPS errors and microphone signal delays. Assuming the microphone signal delay to be small, performing this measurement will show the accuracy of the aGPS method. As a secondary objective, this measurement will show that a position calibration of externally sampled microphones is possible. The aGPS's reference microphones are connected to the NI DAQ system, while the CAE system runs on its own DAQ.

The components of the aGPS module were already mentioned in section 6.2 and will not be repeated. A picture of the measurement setup is shown Figure 6.3a. Both the aGPS and CAE microphone array are set up in an upright position, with a distance of 2 m between their centres (unlike the 0.6 m in the picture). In aGPS coordinates, the centre of the CAE antenna was positioned at $[0, 0, 2]$m. The speakers in the aGPS panel were excited by a white noise signal. The CAE microphone array, having 112 microphones, is mounted on a tripod and connected to a laptop running *CAE noise inspector*. This software allows for measuring with their acoustic antenna and saving the microphone signals to a *.tdms* file.

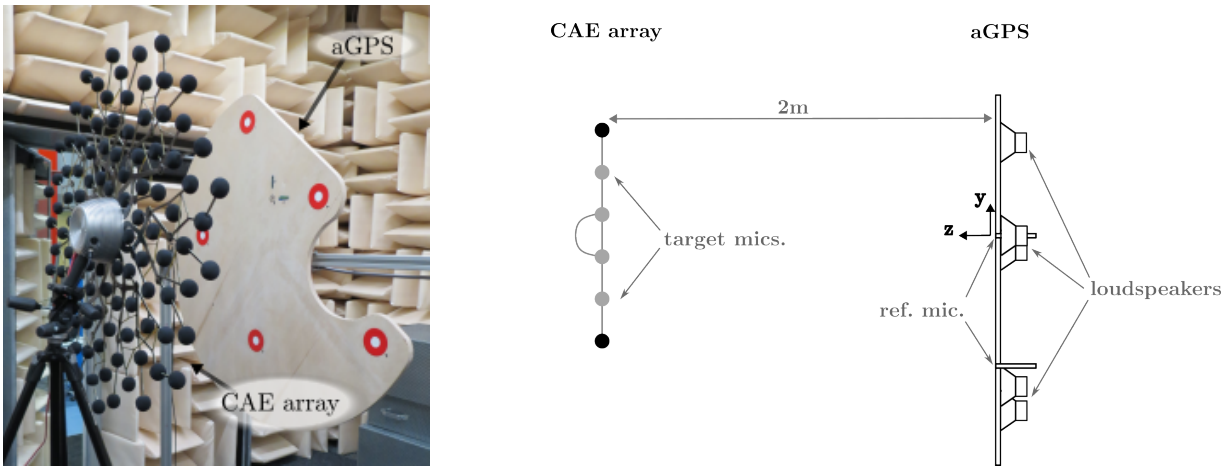

(a) (b)

Figure 6.3: (a) Shows the CAE array and aGPS module used during the aGPS performance assessment. (b) Shows a simplified sketch of the setup with the used (aGPS) coordinate system and the distance between aGPS and acoustic camera.

First, the speed of sound will be calculated using Equation 6.1.2. The calculated speed of sound is compared to the speed of sound in an ideal gas: $c = \sqrt{\frac{\gamma RT}{M}}$. In this equation, γ is the heat capacity ratio, R is the molar gas constant, T is the absolute temperature, and M is the molar mass of the gas.

Then, using the calculated delays and the speed of sound, the optimisation algorithm determines the acoustic positions of all microphones (and loudspeakers). The acoustic positions of the target microphones are compared to the microphone coordinate file of the CAE array.

DAQ settings and signal processing

The measurements were performed at a sampling frequency of 47 998 Hz. This is significantly lower than the 200 kHz mentioned previously but was restricted by the sampling frequency of the CAE array. Furthermore, a sampling time of 10 s was chosen. These settings were used for all five measurements (one for each speaker). All signals were bandpass filtered between 4 kHz and 15 kHz with a damping of 150 dB per decade.

Then, time-shift corrections were applied to the target microphone signals. Time-shift correction was applied by assuming the distance between the first target microphone and the first reference microphone was known. Using the calculated speed of sound, an estimated delay could be calculated. The mismatch between the expected and actual delay was used to shift the target microphone signals and correct for the unsynchronised measurement start.

The delays are calculated between the shifted target microphone signals and the reference microphones. For Welch's method in determining the delays, a *hanning* window with 2048 samples was chosen along with 50 % overlap. The calculated delays were stored in the delay matrix.

The interior-point optimisation algorithm was chosen for the SC-aGPS algorithm and the transformation into the acoustic camera's frame of reference. The following constraints were used (Equation 6.1.5): E_i =0.2 m, E_j =0.002 m, and E_k =0.002 m.

Results of the CAE position calibration

The temperature at the time of measuring was 26.5 °C. In dry air[1], this results in a speed of sound of 346.9 m s^{-1}. The aGPS estimated the speed of sound at 347.1 m s^{-1}. This results in a deviation of 0.2 m s^{-1} (error of 0.06 %).

After 193 iterations of Equation 6.1.4 an minimum was found that satisfied the constraints in Equation 6.1.5. The average deviation of the CAE array within aGPS coordinate frame was calculated as 5.43 mm. After the coordinate transformation into the array's frame of reference, the average deviation was calculated as 4.93 mm. Figure 6.4a shows the deviations decomposed in the x, y, and z components, where also the average deviation is given by a grey circle. The average deviation in x, y, and z direction was calculated to be 3.2 mm, 0.9 mm and 2.9 mm respectively.

The Euclidean norm of the deviation for each microphone can be seen in Figure 6.4b. Many microphones show only a slight deviation. However, 8 outliers are visible with a deviation larger than 10 mm.

[1]This assumes that there is no moisture in the air, furthermore, γ = 1.4, R =8.3145 J mol^{-1} K^{-1}, and M =0.028 964 5 kg mol^{-1}

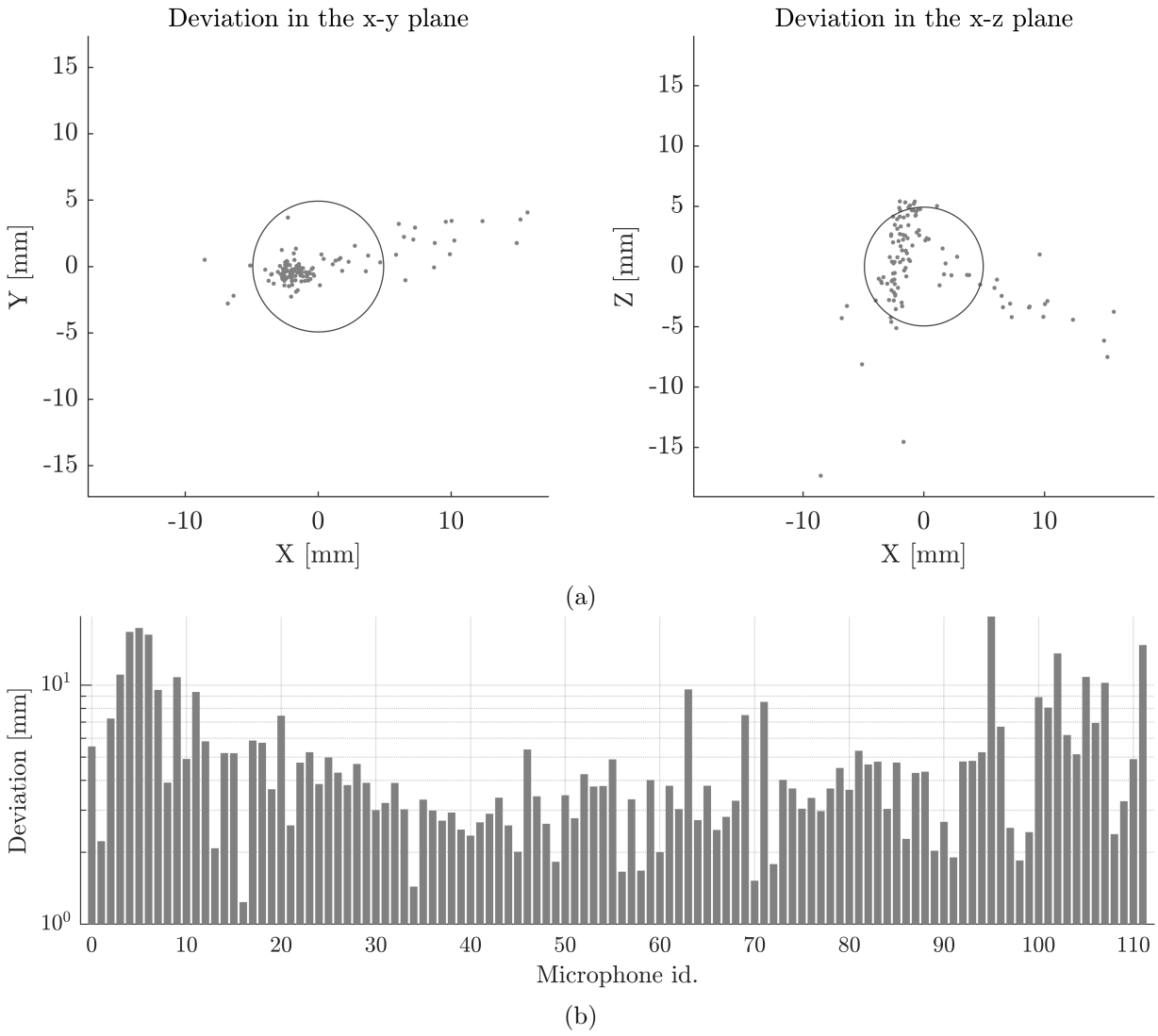

Figure 6.4: (a) The deviations per microphone of the CAE antenna in the x-y (left) and x-z plane (right). The average deviation is given by the circle. (b) The deviation's Euclidean norm for each microphone of the CAE antenna.

6.3.2 Phase calibration of the ground positioned acoustic camera

The ground-positioned microphone phased array is calibrated to see if beamforming improvements can be obtained in section 7.1. The components necessary for such a calibration are the aGPS (discussed in section 6.2) and the ground-positioned acoustic camera (discussed in chapter 5). The setup is schematically shown in Figure 6.5, while a picture is given in Figure 7.1. The loudspeakers in the aGPS were sequentially powered with a white noise signal, while the DAQ sampled 58 microphones (2 reference microphones and 56 target microphones).

This section aims to show the results of a position calibration of the ground-positioned microphone phased array. Therefore, a comparison between the calculated and aGPS-retrieved speed of sound is omitted. Hence, only the deviation from the initial guess of microphone positions is shown.

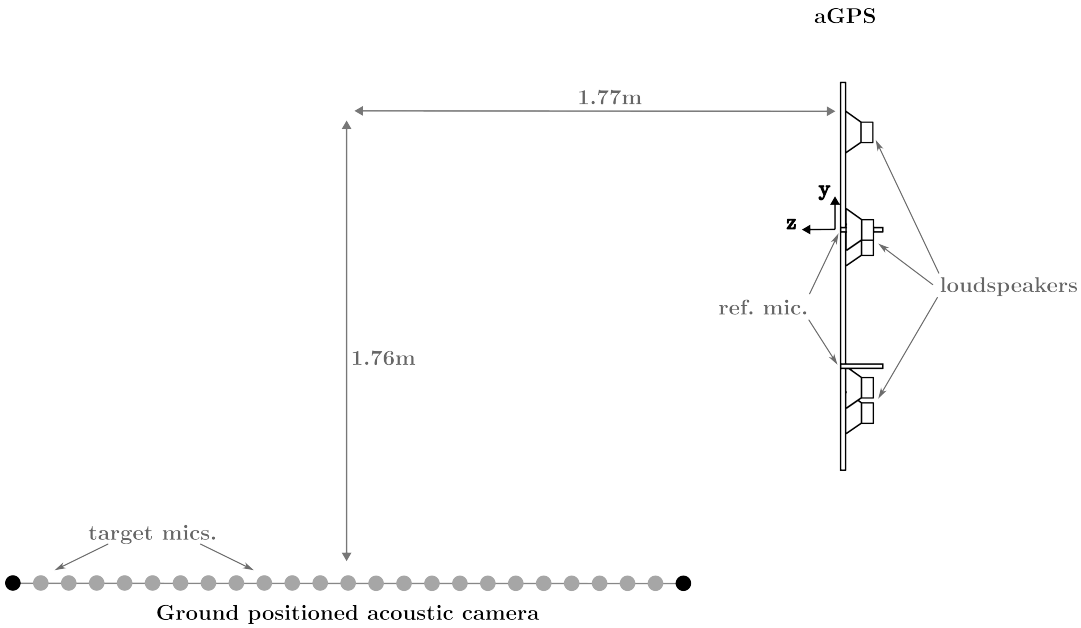

Figure 6.5: The measurement setup for a position calibration of the ground-positioned microphone phased array. The central microphone of the ground-positioned phased array was placed at $[0.24, -1.76, 1.77]$m in aGPS reference frame.

DAQ settings, signal processing, and optimiser settings

A higher sampling frequency could be chosen since the aGPS and acoustic camera were both connected to the NI DAQ. Therefore, a sampling frequency of 200 kHz was used in 5 measurements of 10 s each. All signals were bandpass filtered between 4 kHz and 15 kHz using 150 dB damping per decade. For Welch's method in calculating the time-delays, a 8192 sample *hanning* window was chosen with 50 % overlap. Such a large window was chosen to allow for the large difference in sound arrival time between the reference and target microphones.

Lastly, the interior-point method was chosen as the optimiser for the aGPS algorithm and the transformation of the reference frame. The following constraints were applied (Equation 6.1.5): E_i =0.2 m, E_j =0.002 m, and E_k =0.002 m.

Results of a position calibration for the ground-positioned acoustic camera

The calculated speed of sound was found to be $345.21\,\mathrm{m\,s^{-1}}$, with which an optimum was found after 362 steps of the interior-point algorithm. However, the optimiser mentioned a possibly lower minimum outside of the constraints.

The average deviation in the aGPS's frame of reference was found to be 1.2 mm. After a coordinate transformation into the acoustic camera reference frame, an average deviation of 0.69 mm was calculated. The deviations per microphone and the corresponding Euclidean norm can be found in Figure 6.6. Three significant outliers are visible, while the rest of the microphones lay within 1 mm of the initial guess (the created coordinates according to section 5.1).

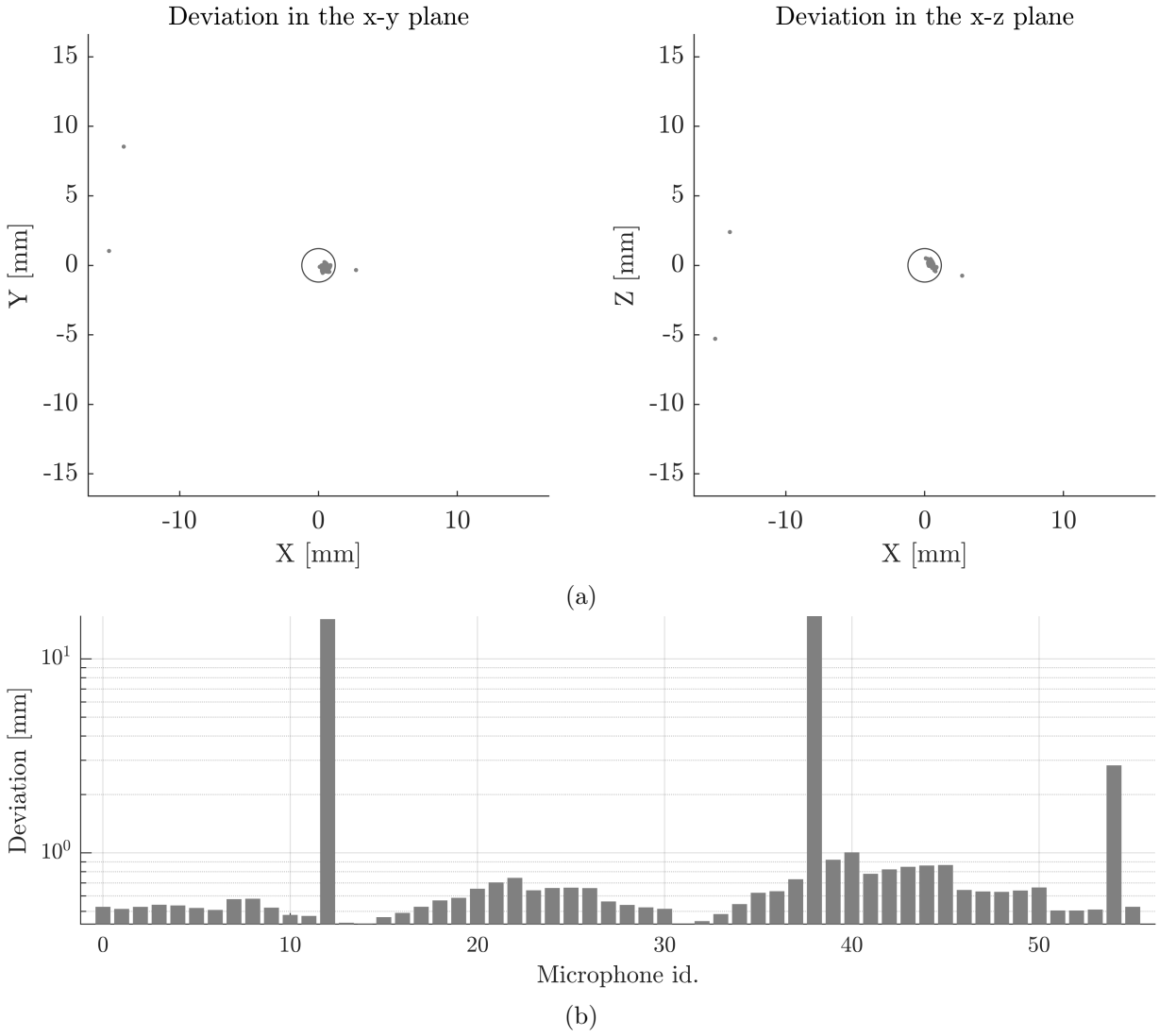

Figure 6.6: (a) The deviations per microphone of the designed antenna in the x-y (left) and x-z plane (right). The circle gives the average deviation. (b) The Euclidean norm of the deviation for each microphone of the designed antenna.

Chapter 7

Experimental shakedown of the ground-positioned acoustic camera

Measurements were performed to validate the functioning of the ground-positioned microphone phased array and test its robustness during outdoor noise measurements on UAVs. Furthermore, the aGPS's use is tested for beamforming applications. The first two measurements were performed in the anechoic chamber of the University of Twente and will validate the functioning of the array and aGPS. The third measurement is an outdoor UAV fly-over measurement. This final measurement will show and discuss the far-field beamforming capabilities of the acoustic camera in outdoor UAV fly-over measurements.

7.1 Performance assessment of far-field beamforming with a loudspeaker

Beamforming is performed on a loudspeaker to assess the performance of the ground-positioned microphone phased array. The performance will be evaluated by comparing the results to a simulation of a monopole sound source. Then, comparisons can be made looking at the array's spatial accuracy, MSL ratio, and SNR. Lastly, the aGPS is employed to see if the output maps can be improved by a position-calibration of the microphones.

The required equipment for the acoustic camera is already discussed in section 5.1 and will not be repeated in this chapter. Also, the aGPS and its corresponding equipment (discussed in section 6.1) are employed for the acoustic position calibration. Moreover, the extra equipment for this measurement includes a Cambridge Audio Minx Min 12 loudspeaker and a rope to hang the loudspeaker from the ceiling. A picture of this setup is given in Figure 7.1.

Firstly, Beamforming is performed with the loudspeaker at 2 m, 2.5 m and 3 m above the array's centre. These measurements are compared with the simulation of a monopole source at the same position as the loudspeaker. Secondly, the microphones were position calibrated using the aGPS, of which the results are discussed in subsection 6.3.2. Output maps are made using the calibrated microphone positions. These output maps will be compared to those without a position calibration to see if any performance improvements are observable.

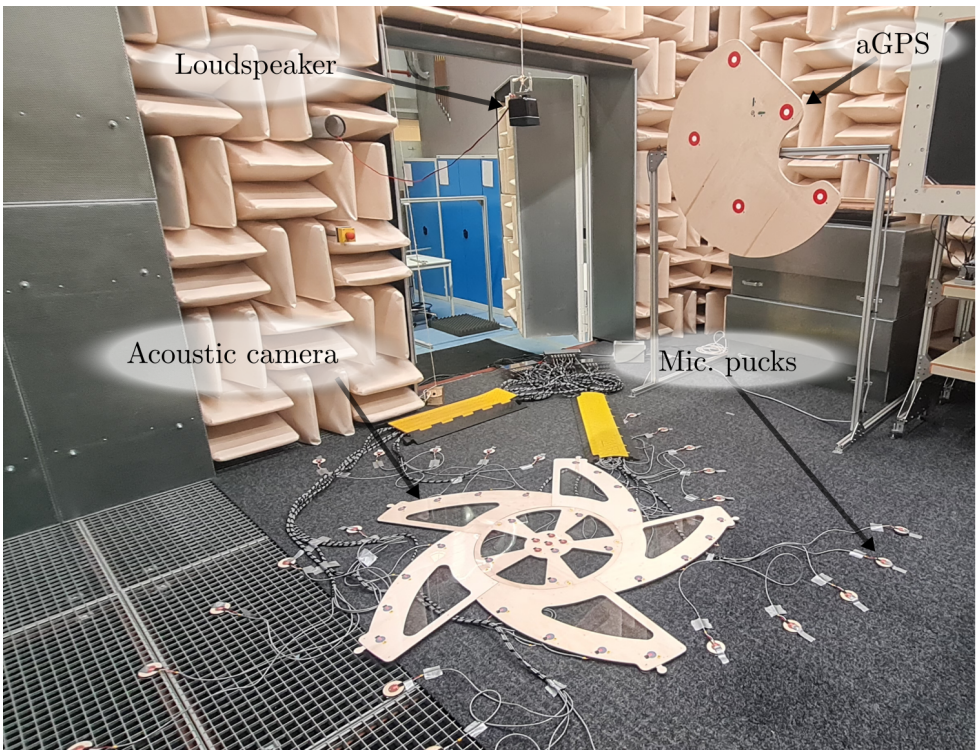

Figure 7.1: The setup for the beamforming performance assessment. The loudspeaker, aGPS, and acoustic antenna are shown.

Data acquisition and beamforming settings

The loudspeaker was powered with a white noise signal, while the microphones were sampled at 47 998 Hz for 10 s. The microphone signals were used to construct the CSM from the power spectral density using Welch's method. A *hanning* window with 1024 samples was chosen with 50 % overlap.

A search grid was constructed between −0.25 m and 0.25 m in both x and y direction. In both directions, 301 gridpoints were used to yield a resolution of 1.7 mm. These output maps are given in dB SPL according to Equation 4.4.18, for which the dynamic range is set to 15 dB.

Beamforming maps of a loudspeaker and results of a position calibration

First, Figure 7.3 gives the results for the loudspeaker at 3 m for different frequencies. Many side lobes are visible in the measurements, especially at high frequencies. The simulation results show less noise and lower side lobe levels. Furthermore, looking at Figure 7.3a, the spatial accuracy of the array seems to be visibly less than the simulatory results. The beamwidth of the measurement is 0.13 m, while the simulatory beamwidth is 0.117 m (4 kHz at 3 m). Lastly, this beamwidth decreases with increasing frequency.

Figure 7.4, shows the results looking at 12 kHz at 2 m, 2.5 m and 3 m from the source. Again, many side lobes are visible with more noise than the simulation results. Furthermore, the beamwidth increases with increasing distance.

Lastly, Figure 7.5 shows the result of a phase calibration. Side lobe levels, SNR and spatial accuracy, remain unchanged (under visual inspection). However, an increase in main lobe level is observed. The increase in the main lobe level is calculated and given in the captions. The increase in primary lobe levels directly results from improved microphone signal coherence and, therefore, improvements in results. The increase of main lobe levels due to a position calibration seems to increase with the frequency under consideration. This is also shown in Figure 7.2, where one can observe that an inverse relationship exists between the observed wavelength and the increase in main lobe level. This is probably due to the fact that the microphones need to be positioned more accurately when looking at smaller wavelengths. Any large position deviation with respect to the observed wavelength will yield inaccurate phase information of the sound. This results in coherence loss between microphone signals. Ernst et al. [50] showed similar results. With 1 mm of a positioning error, the level loss of the primary lobe is positively correlated to the frequency under consideration. The results in Figure 7.2 and Figure 7.5 show that only a slight main lobe increase is obtained in the current setup with a position calibration.

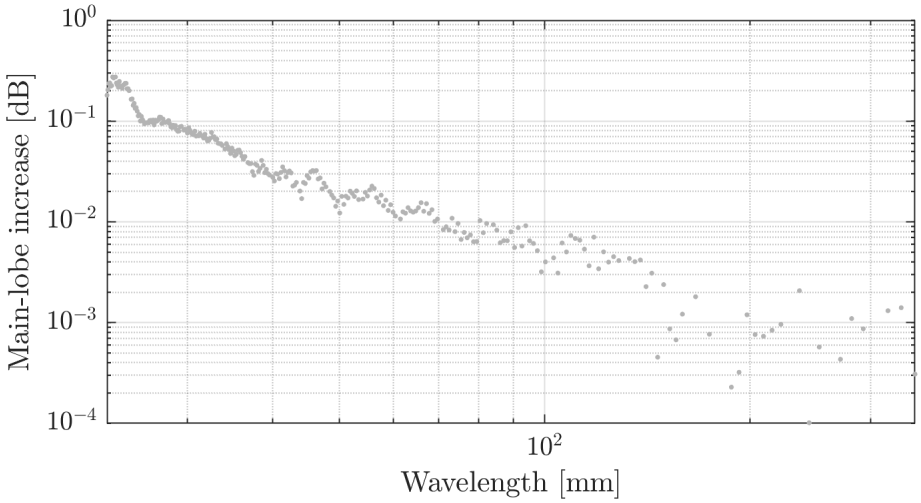

Figure 7.2: The increase in main lobe level for position calibrated measurements when performing a beamforming measurement on a loudspeaker at 2 m.

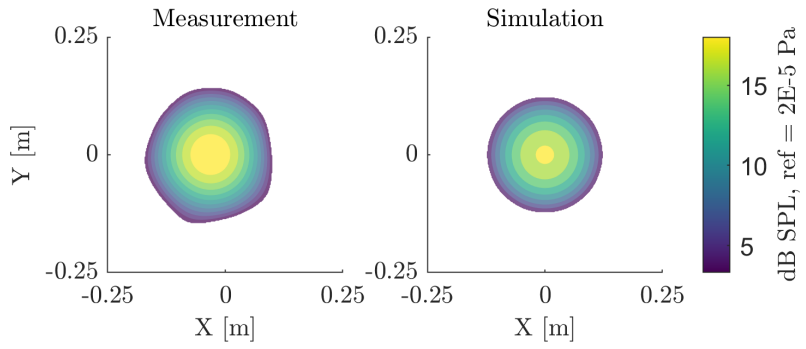

(a) 4 kHz

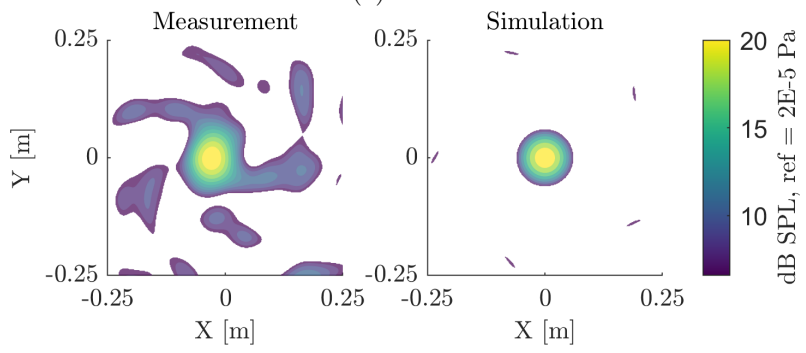

(b) 8 kHz

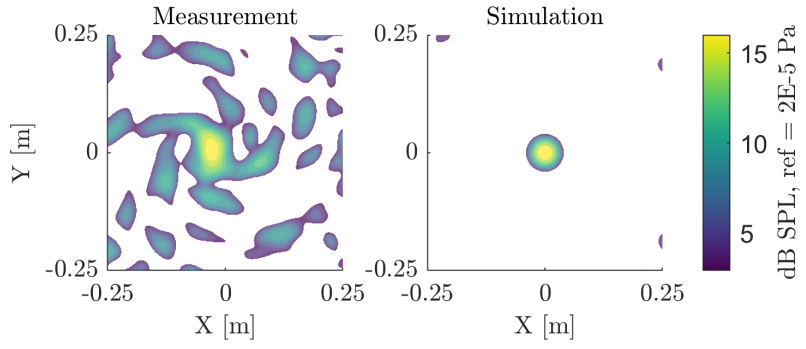

(c) 12 kHz

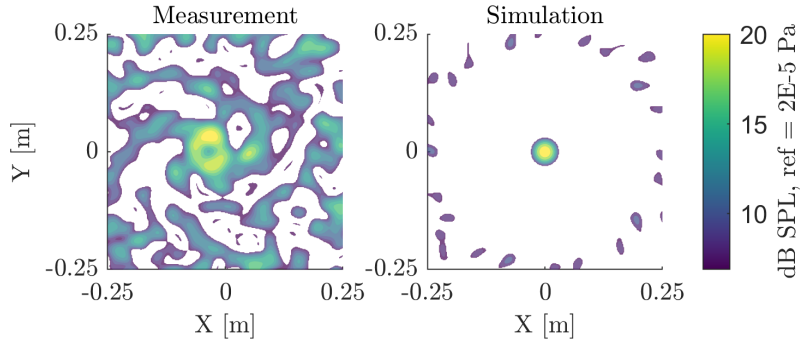

(d) 16 kHz

Figure 7.3: The beamforming maps at 3 m for different frequencies. Results were obtained with the designed array.

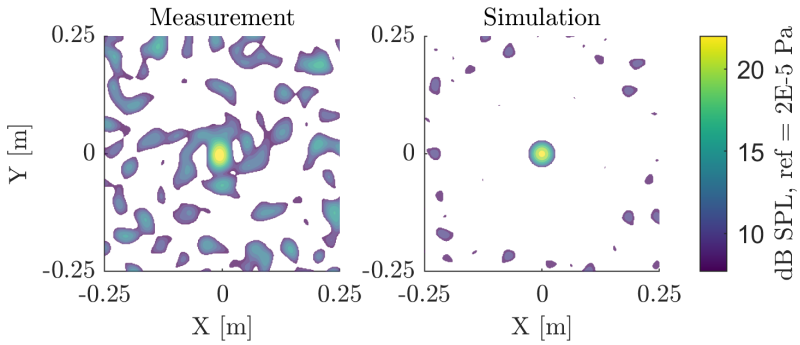

(a) 2 m distance

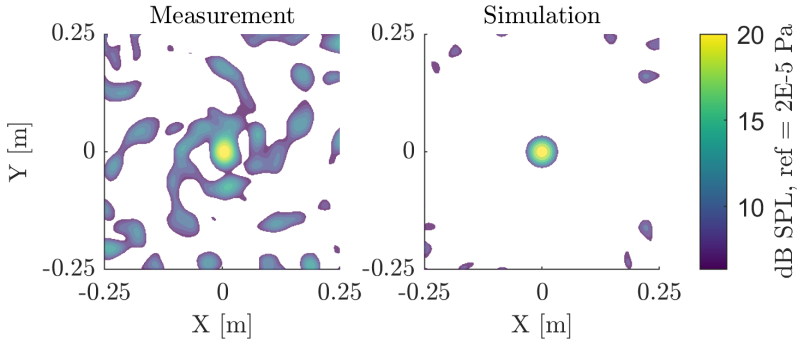

(b) 2.5 m distance

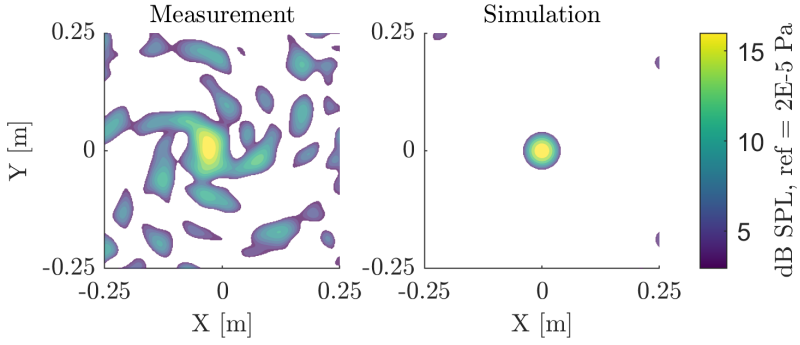

(c) 3 m distance

Figure 7.4: The beamforming maps of 12 kHz at different distances. Results were obtained with the designed array.

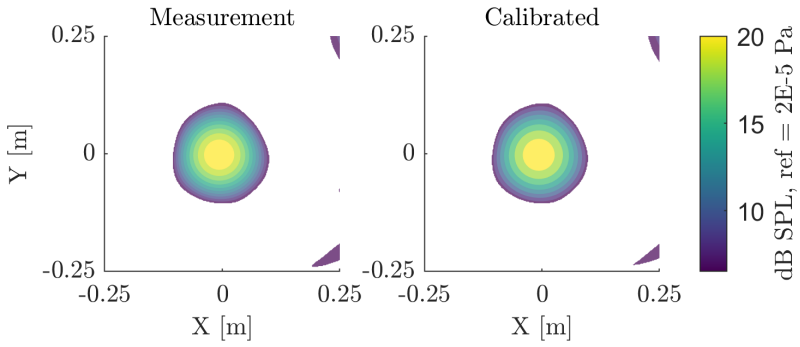

(a) 4 kHz, 0.007 dB main lobe increase

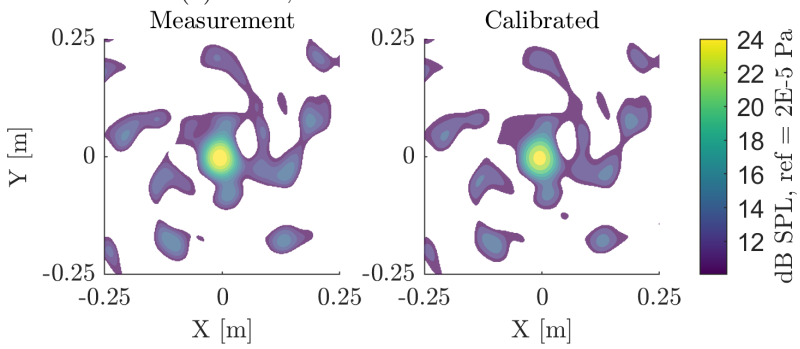

(b) 8 kHz, 0.023 dB main lobe increase

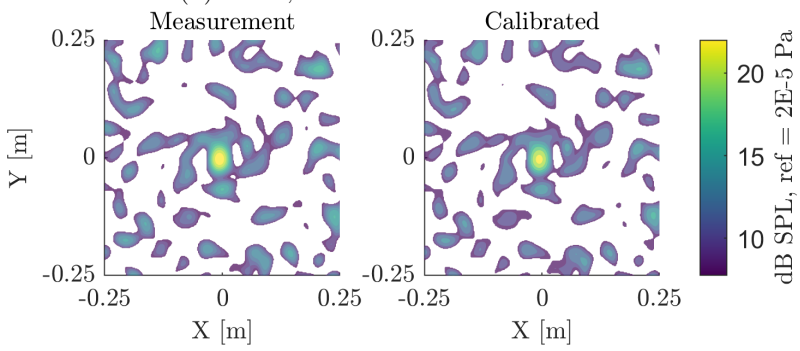

(c) 12 kHz, 0.093 dB main lobe increase

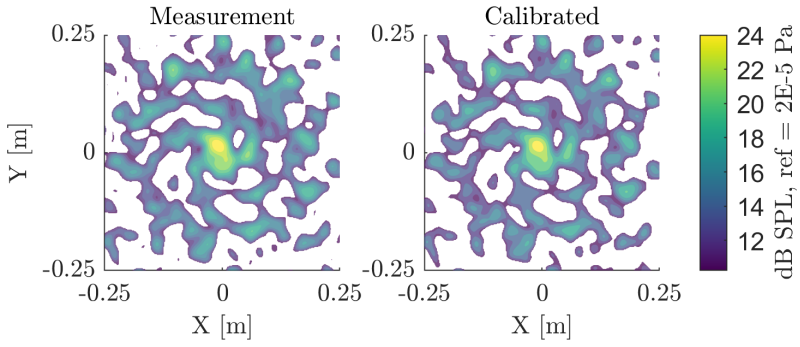

(d) 16 kHz, 0.116 dB main lobe increase

Figure 7.5: The beamforming maps for a phase calibration at 2 m in the centre of the array.

7.2 Noise source localisation on a fixed UAV

Beamforming is performed on a DJI Phantom 4 to form a baseline for UAV beamforming measurements. The resulting output maps are discussed, and possible sound sources are highlighted. This measurement will validate the functioning of the ground-positioned microphone phased array for measurements on (relatively) small UAVs.

Besides the acoustic camera and its necessary equipment, a stock DJI Phantom 4 was mounted to the ceiling. This was done in such a way that the downwash of the rotors would not impinge on any framing. This frame was constructed using aluminium profiles and steel wire. A special aluminium claw was built with soft padding to hold the UAV from the top. Using tie wraps, the UAV was mounted in this claw. This setup is shown Figure 7.6, where part of the framing, the UAV, and the acoustic camera are visible. A picture of the UAV and its relevant information is in the appendix in Figure A.3.10 and Table A.3.5.

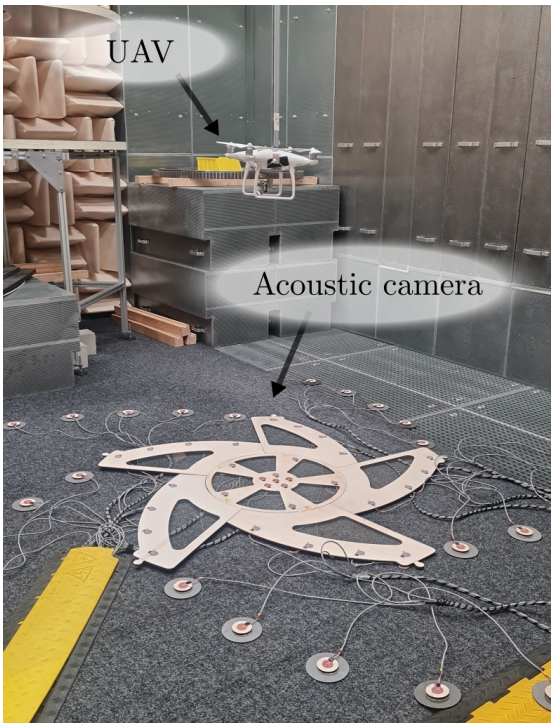

Figure 7.6: The setup for the beamforming measurement on a DJI Phantom 4.

The drone was suspended 1.3 m above the (aGPS calibrated) array and was given a slight power input. The RPMs could not be set, so giving a slight thrust input was achieved using the joystick on the controller.

The power spectral density is calculated and given in dB SPL to get an idea of the frequency content of the sound. These spectra are plotted for three microphones at different distances from the array's centre. Additionally, the results from source region integration are provided. Also, the SPL is calculated for each microphone independently according to Equation 3.2.16. Lastly, the most prominent frequencies in the spectra will be examined using conventional beamforming with the ground-positioned microphone phased array. The output maps are calculated at the array's centre, according to Equation 4.4.18.

Data acquisition and beamforming settings

Measurements were performed for 10 s at a sampling frequency of 47 998 Hz. The signals were A-weighted before being used in subsequent calculations. The CSM is constructed with the power spectral density using Welch's method. A *Hanning* window of 1024 samples at 50 % overlap was used. Diagonal removal was also enabled. A search grid was chosen between -0.75 m and 0.75 m using 301 points in the x- and y-direction. In these figures, a dynamic range of 6 dB was chosen. The exact position of the drone was measured using a Leica Disto X3 and measuring tape. Therefore, a trace-out of the drone is given in the beamforming maps.

Power spectra and beamforming maps of a fixed drone in an anechoic chamber

The power spectral density and the results for source region integration are given in Figure 7.7. Increased levels are found around 1.5 kHz, 3.1 kHz and 5.6 kHz. Besides these peaks, significant broadband noise is visible, especially close to the array's centre. Amplitude differences are visible between the edge ($r = 1.5$m) and the centre ($r = 0$m) of the array. This difference is most possibly due to the downwash of the rotors impinging on the microphones, since no windshields had been installed yet at this stage.

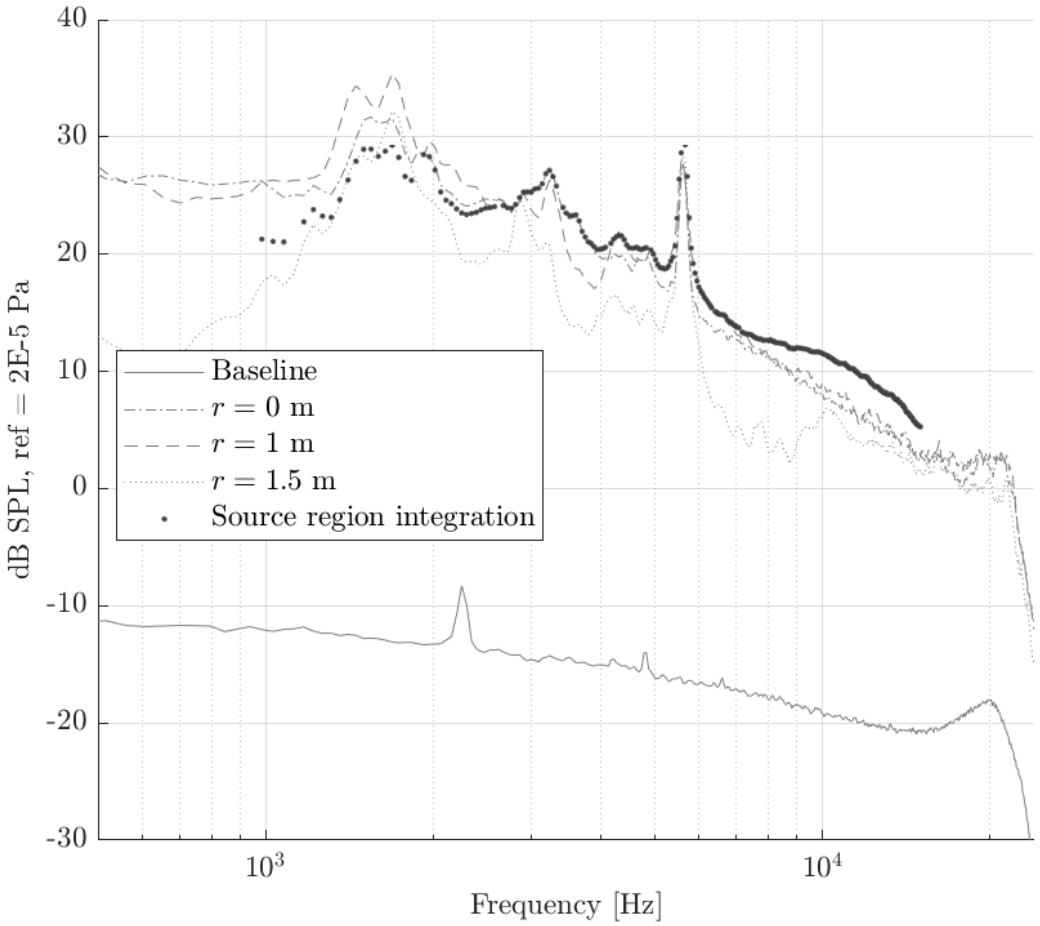

Figure 7.7: The power spectral density of a DJI Phantom 4 under slight loading at 1.3 m.

The SPL level per microphone is given in Figure 7.8. The SPL is approximately 64 dB directly underneath the drone (average over the central frame of the array). These levels reduce towards the edge of the array to 58 dB ($r = 1.5$ m). No magnitude calibration of the Sparkfun microphones was performed, which can explain some of the outliers in Figure 7.8.

The beamforming results for 1.5 kHz, 3.1 kHz and 5.6 kHz are given in Figure 7.9. The beamforming results at 1.5 kHz and 3.1 kHz show main lobes at the struts of the drone. Therefore it seems that the increased spectral levels at 1.5 kHz and 3.1 kHz are a result of rotor-strut interaction. Furthermore, this rotor-strut interaction for another rotor is presented in Figure 7.10a at 3.4 kHz.

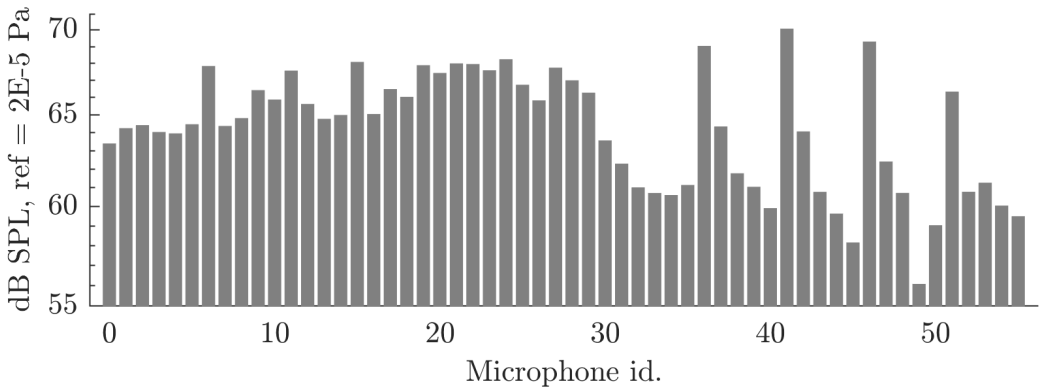

Figure 7.8: The SPL per microphone for the measurement on a DJI Phantom 4, with a baseline value of 28 dB.

The beamforming result at 5.6 kHz show four distinct main lobes at the location of the electric engines. Henderson et al. [53] showed that the electric motor noise from these DJI platforms is tonal and mainly comes from motor vibration modes and current switching of the controller.

Figure 7.10 also shows a result at 6.8 kHz, in which the rotors themselves are producing the most noise. Further investigation shows that this interaction is present at frequencies between 3.7 kHz and 10 kHz, for which some of the results are given in the appendix in Figure A.3.11. Furthermore, the maximum is found at the point where the front and aft rotors (top and bottom in the map) meet. As discussed in section 2.3, this could very well be due to the unsteady loading of a blade passing through a tip vortex created by the opposing blade in combination with turbulent flow impingement (also created by the opposing blade) [37, 38]. The tips of the front and aft rotors only have 4 mm between them, while the separation distance between the left and right rotor pairs is 10 mm. This could explain the lower levels in between the left and right rotor pairs.

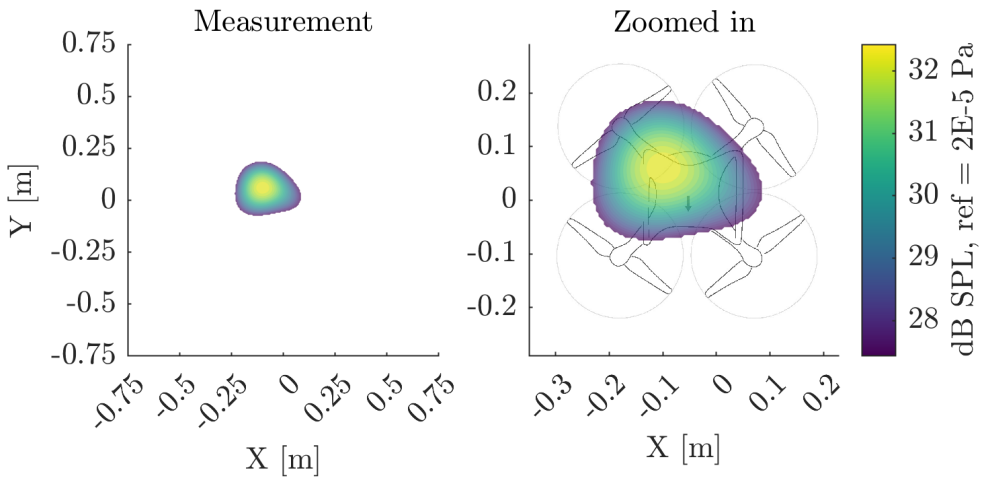

(a) Frequency of 1.5 kHz

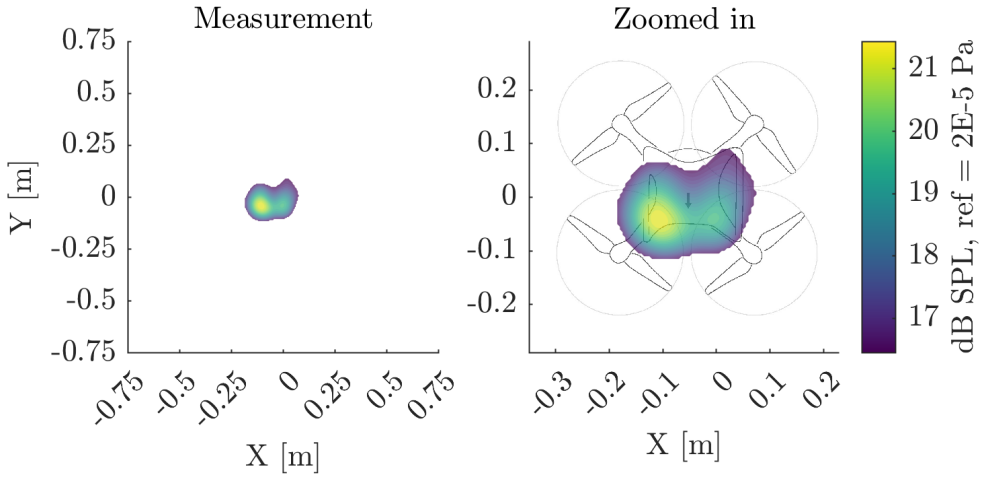

(b) Frequency of 3.1 kHz

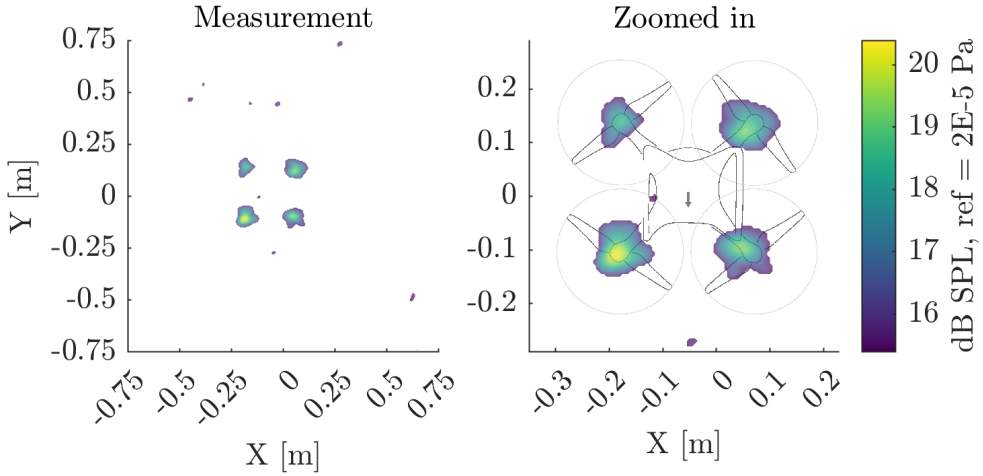

(c) Frequency of 5.6 kHz

Figure 7.9: The beamforming results for the measurement on a DJI Phantom 4. The beamforming maps correspond to some of the increased levels in Figure 7.7.

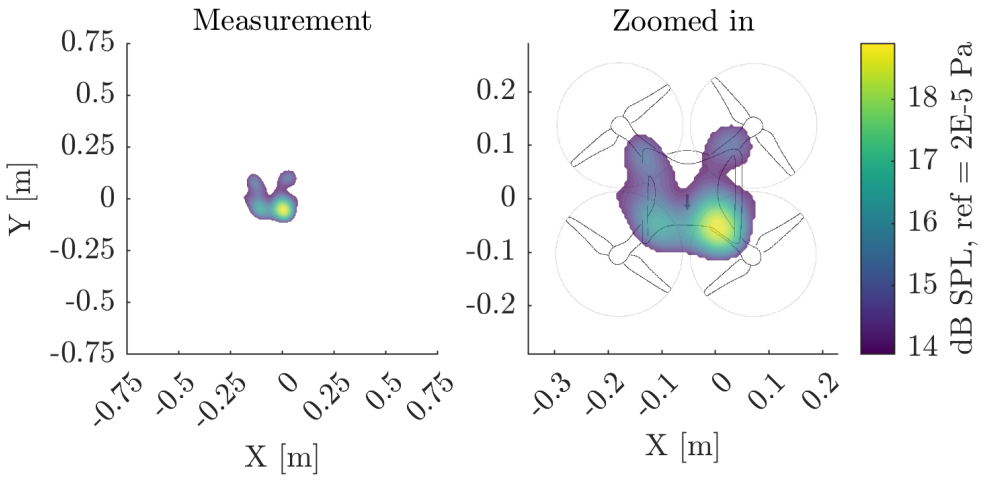

(a) Frequency of 3.4 kHz

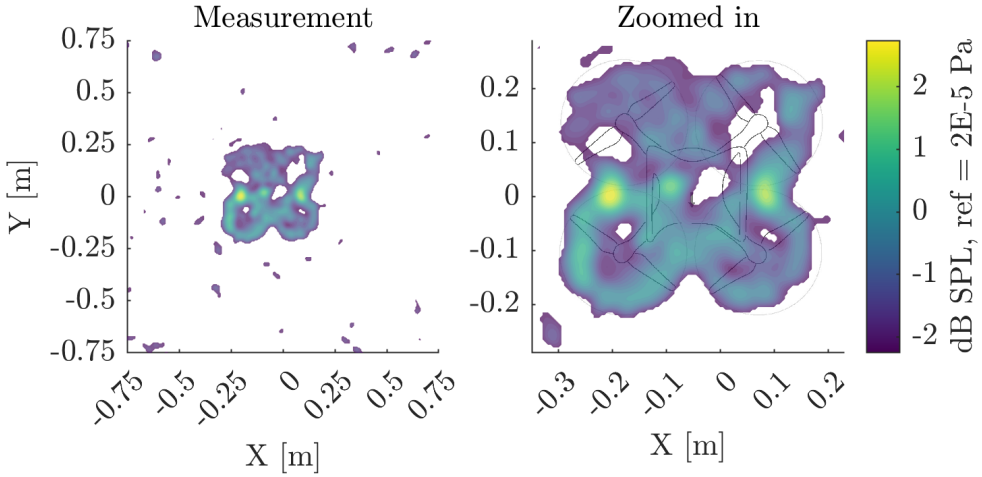

(b) Frequency of 6.8 kHz

Figure 7.10: Follow up on Figure 7.9. Two other frequencies are highlighted with lower pressure levels.

7.3 Noise source localisation on a hovering UAV

The final measurement is performed outside to validate the ground-positioned acoustic camera for UAV fly-over measurements. This is done using the same DJI Phantom 4 as in section 7.2. However, instead of mounting the UAV, the UAV hovered at different altitudes above the array's centre.

These measurements were performed at the University of Twente. A picture of the field (along with some of the equipment) is shown in Figure 7.11. All necessary precautions and legislation were followed for a safe and legal measurement.

Figure 7.11: The field in which the measurements are performed. The UAV, acoustic camera, distribution boxes, and auxiliary equipment is visible.

Power was provided by a nearby portacabin (50 m away) and was run to the measurement setup by a cable drum. Windshields were attached over the microphone ports to reduce flow-induced noise. Steel discs, acting as weights, were also added to the microphone pucks to ensure they would not move once placed. The acoustic camera was placed on a waterproof canvas to reduce the chance of moisture damage to the microphones and slightly level the uneven ground. The computer and DAQ system were placed on a table at 10 m distance from the distribution boxes. The distribution boxes were placed at 1.5 m from the edge of the acoustic array and were covered by fabric to reduce reflections. An umbrella shaded the computer and NI DAQ systems to reduce heat accumulation.

Measurements on the UAV were performed at 2 m, 2.5 m, 3 m, 4 m, 5 m and 10 m above the array's centre. The altitude was obtained from the downward-facing sensor of the UAV. Also, some measurements were performed without a hovering UAV as a baseline. The power spectral density is calculated to give an insight into the frequency content of the sound (presented as dB SPL). These power spectra are plotted for three different flight altitudes (along with the baseline measurement). Also, the microphone average SPL as a function of UAV altitude is calculated. Conventional beamforming is then used to attempt sound source localisation.

Finally, no position calibration was performed on the microphones using the aGPS. section 7.1 showed only a slight improvement in the beamforming map. Furthermore, the aGPS is currently heavy and difficult to transport.

Data acquisition and signal processing

Measurements were performed at 47 998 Hz for 10 s. The obtained signals were A-weighted. The CSM is constructed with the power spectral density using Welch's method. A *Hanning* window of 1024 samples at 50 % overlap was chosen. The diagonal elements of the CSM were removed.

A search grid was chosen between −0.75 m and 0.75 m using 301 points in the x- and y-direction. In these figures, a dynamic range of 6 dB was chosen. Output maps are presented in dB SPL at the array's centre, according to Equation 4.4.18. The position and orientation of the drone could not be retrieved from measurements or images. Therefore, no zoomed-in view is given in the output map, and there is no trace-out of the drone in the beamforming results.

Results of outdoor noise measurements on a UAV fly-over

The power spectral density of the drone at different altitudes is given in Figure 7.12 for the central microphone. This graph shows many peaks in the spectrum between 100 Hz and 2000 Hz. These peaks are visible and at similar frequencies for all three altitudes. According to the UAV's datasheet, the maximum motor RPM is 193 Hz. This means that the peak around 180 Hz probably corresponds to the BPF (with the two-bladed rotor) and a rotational velocity of approximately 90 Hz. The subsequent peaks at $n \cdot 180$ are related to the harmonics of the BPF. At 2 m distance, all of these peaks are less prominent with respect to the overall broadband level, possibly due to the downwash on the central microphone and causing flow-induced noise. Furthermore, in the frequency domain above 2 kHz, a harmonic tone at 3.5 kHz is being produced.

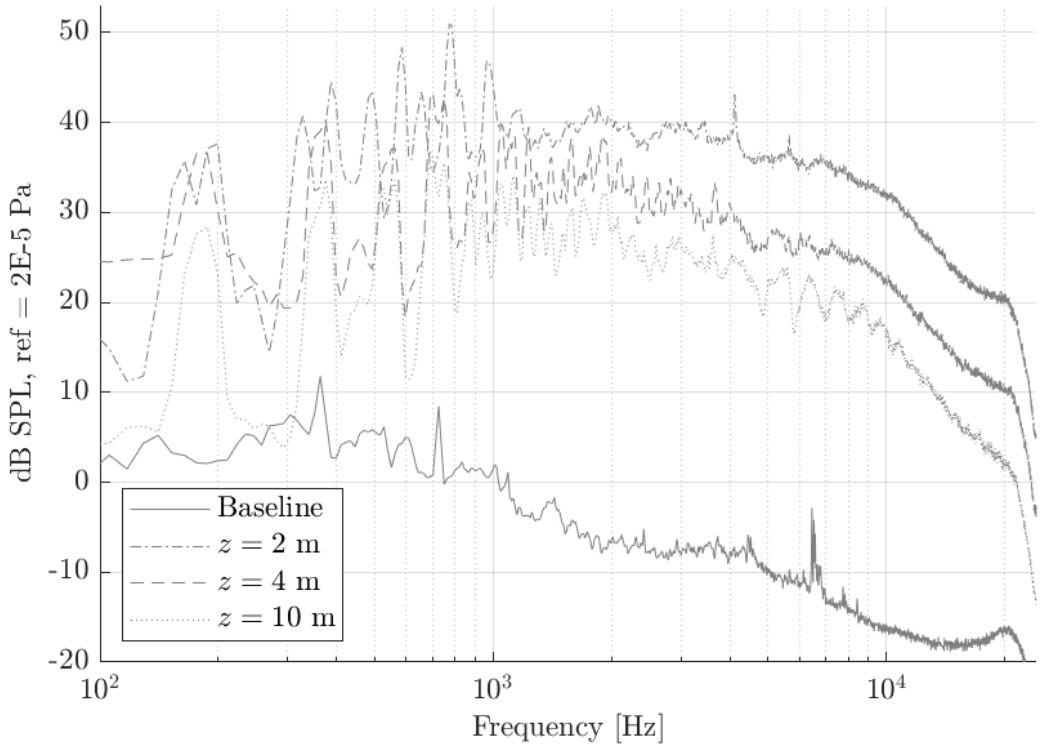

Figure 7.12: The power spectral density of a DJI Phantom 4 at three different altitudes, measured directly underneath the drone. A baseline measurement is added.

The array average SPL levels at the six different altitudes are given in Figure 7.13. At 2 m an SPL of 77.6 dB is observed, while at 4 m the pressure level is reduced to 70.9 dB (6.7 dB reduction). The same is the case when looking at 3 m to 6 m. From 3 m to 6 m the SPL drops from 74.2 dB to approximately 68.1 dB, halving the pressure level. This means that the sound pressure level is approximately halved for doubling the measurement distance. In conclusion, one can observe that the sound pressure level decreases inversely with the measurement distance.

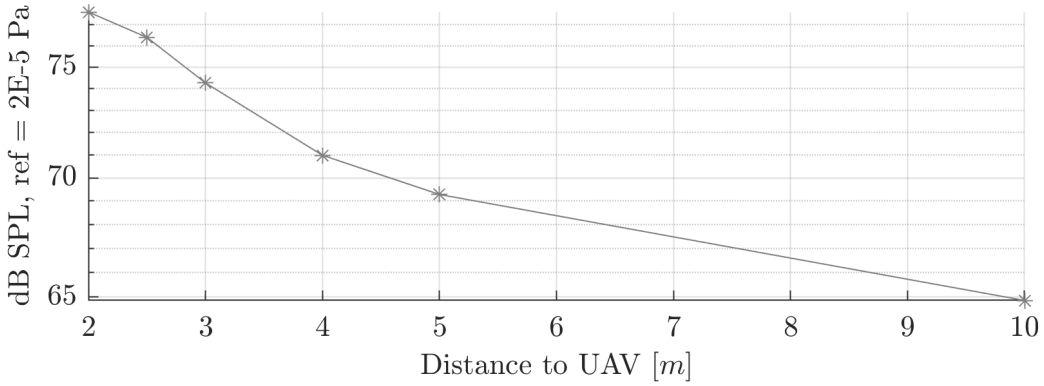

Figure 7.13: The array average SPL as a function of measurement distance to a hovering DJI Phantom 4. The SPL without a hovering UAV was calculated to be 36 dB.

Figure 7.14 shows the resulting beamforming maps at 1.4 kHz, 3.5 kHz, 5.6 kHz and 6.8 kHz at an altitude of 3 m. This increased altitude was chosen to reduce the contribution of flow-induced sound. 1.4 kHz and 3.5 kHz correspond to increased levels in Figure 7.12 with respect to the broadband noise, for which the wavelength is approximately equal to or smaller than the rotor diameter ($f \geq 1.4$ kHz). Also, 5.6 kHz and 6.8 kHz were chosen to compare with the results in Figure 7.10.

The resulting beamforming maps show the main lobes at the position of the UAV. However, it is impossible to distinguish the exact sources of the sound (e.g. rotor-strut, tip-to-tip interaction, motor sound, etc.). Furthermore, at 6.8 kHz results become more noisy than Figure 7.10. No rotors are visible, nor is the tip-to-tip interaction. This is possibly due to the uneven ground on which the microphones were laid out. This could deteriorate the output map due to inaccurate signal phase information, making source localisation difficult. This becomes an even larger problem at higher frequencies, which is shown in Figure A.3.12.

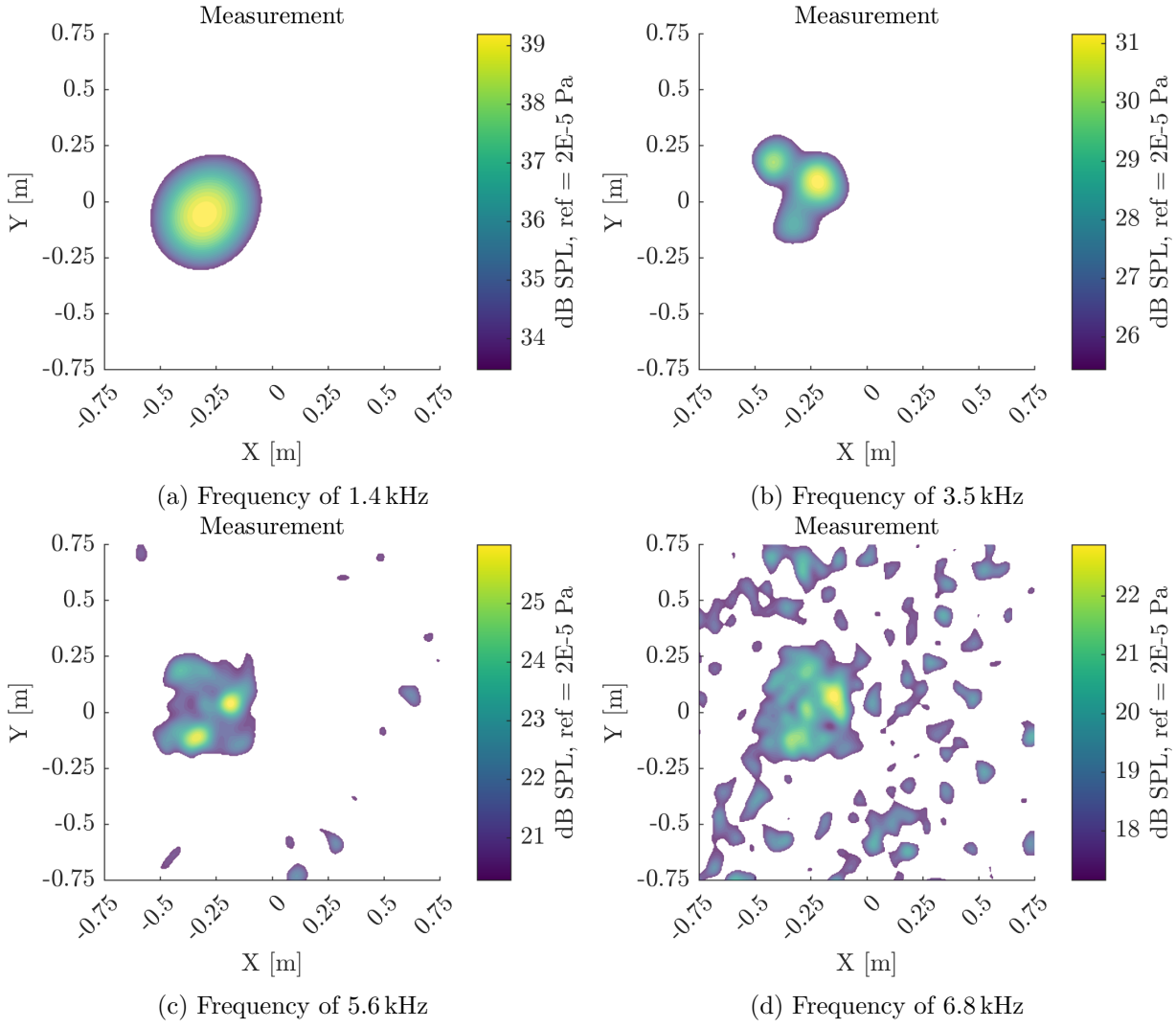

(a) Frequency of 1.4 kHz

(b) Frequency of 3.5 kHz

(c) Frequency of 5.6 kHz

(d) Frequency of 6.8 kHz

Figure 7.14: Beamforming results of a hovering DJI Phantom 4 at 3 m altitude.

Chapter 8

Discussion

aGPS experimental validation using the CAE antenna

Firstly, Ernst et al. [50] mention the need to oversample the microphone signals. For this reason, they sample at 200 kHz. Because the CAE camera was limited to 47 998 Hz, a lower sampling frequency had to be used. However, acoustic positions might have been more accurately determined if an increased sampling frequency could have been used.

Furthermore, the aGPS measurements were started at roughly the same time. However, the aGPS method requires the signals to start simultaneously. It is common for a *.tdms* file to mention the measurement start time, with which the signals could be synchronised in post-processing. However, the CAE microphone array outputted incorrect date-time data. Shifting the signals was therefore done, assuming that the central target microphone was exactly 2.0145 m from the first reference microphone of the aGPS. The expected delay between these two microphones could then be calculated. This information was used to time-shift the signals to appear as if they had started synchronously. However, this is not how the method is supposed to work. Therefore, results for externally sampled microphone arrays could be improved if *.tdms* time data was accurate, or the measurements could be coupled to start simultaneously. Coupling these measurements should, therefore, be investigated further for future use.

Phase calibration of the ground positioned acoustic camera

Results show that most microphones were placed within 1 mm of the aGPS calculated positions. This would be very coincidental and should, therefore, be carefully interpreted. It is possible that a local minimum was found in the optimisation, causing the optimiser to stop. However, this is a hypothesis and should be investigated further. This could possibly be improved with the use of multi-agent method optimisers (such as ant-colony optimisation). Furthermore, this could be a cause of the minor improvements in the beamforming results in section 7.1. Avoiding this problem might significantly improve the aGPS performance.

Performance assessment of far-field beamforming with a loudspeaker

The speaker was assumed to behave like a monopole source, so it was compared with a monopole in a simulation. However, a speaker can act as a complex source if no converging duct is used.

Lauterbach et al. showed that at increased frequencies, using a well-calibrated acoustic camera, the speaker no longer behaved like a simple monopole, and the circular diaphragm of the speaker became visible [49]. The speaker used in section 7.1 has a diaphragm diameter D of 57 mm and could, therefore, produce complex (non-monopole) beamforming maps at frequencies where the speaker's diaphragm is no longer considered acoustically compact, $D \gg \frac{\lambda}{2\pi}$, i.e. $f \gg 1\,\text{kHz}$. This could explain the considerable deviation between the simulation and the measurement at increased frequencies.

Noise source localisation on a fixed UAV

During the measurement with a mounted UAV, the rotational velocity of the rotors could not be controlled precisely. Instead, the RPM was controlled using the joystick on the controller. This resulted in unsteady rotor RPMs. This could be why a BPF could not be retrieved in Figure 7.7.

Also, no windshields were attached yet, so flow-induced noise was not filtered out in these measurements. These windshields, along with weights, were added during the outdoor measurements.

Lastly, Figure 7.8 showed that most microphones (at similar distances to the source) have approximately the same SPL. However, there were a few outliers. This could result from different microphone sensitivities and could be solved by magnitude calibration. This calibration could very well improve the beamforming results further.

Noise source localisation on a hovering UAV

The drone's location and orientation could not be exactly retrieved to overlay the beamforming results. This made the interpretation of the results difficult. An upward-facing camera could be added to the array to better understand the specific sound sources on the drone by overlaying a photograph over the acoustic output map.

Also, the results were noisy, probably because of the uneven ground on which the microphones were placed. The aGPS could have been used to find the positions of the microphones. However, the aGPS was not brought to the measurement location due to its weight and size.

Furthermore, the programmed LabView software could not accurately calculate the output map in real-time. This could be due to the computer's overheating and should be investigated further for future use.

Chapter 9

Conclusions and Recommendations

The capabilities of the ground-positioned microphone phased array were successfully demonstrated, showcasing its potential as a valuable tool for noise analysis of UAVs, ultimately contributing to the mitigation of UAV noise pollution. section 7.2 showed that the sound emitted by a DJI Phantom 4 under slight loading is most possibly a result of rotor-strut noise, tonal electric motor noise, and airfoil/rotor noise. This supports earlier research on UAV sound radiation [37,38]. It is recommended that the rotor RPMs be controlled for any future measurements. Furthermore, future research can focus on mapping these sound sources, yielding valuable information for the noise reduction of UAVs.

Secondly, it is shown that the frequency spectrum of a hovering DJI Phantom 4 consists of broadband noise and BPF-related tones. Using the resulting beamforming maps, the position of a UAV could be retrieved. However, distinguishing specific UAV sound sources (rotor-strut interaction, electric motors, etc.) proved difficult since the exact position and orientation of the UAV could not be measured. Furthermore, high-frequency results were noisy, possibly due to placing the microphones on uneven ground. Therefore, it is recommended that a light, flat frame be constructed to lay the microphones on a flat surface and that an upward-pointing camera be installed on the ground-positioned microphone phased array.

Thirdly, section 6.3 showed that the self-calibrating acoustic GPS method can successfully determine the acoustic positions of many microphones. Furthermore, it also accurately calculates the speed of sound. In section 7.1, a position calibration with the aGPS for beamforming resulted in slightly increased main lobe levels. The method could be enhanced by choosing a multi-agent optimisation method to avoid local minima. Lastly, a lightweight alternative to the currently constructed aGPS could benefit outdoor measurements with microphone position calibrations.

Furthermore, the cost of the NI DAQ makes outdoor measurements daunting. A cheaper alternative can be chosen to lower the impact of a damaged acquisition system, such as a Sirius R4 from Dewesoft or an INET-400 expandable card cage from Omega (with one 430 card and two 420 cards). These systems would allow for at least 56 synchronised analogue input channels with a sampling rate of at least 90 kHz. Choosing either system would allow students to perform beamforming measurements with the designed array at reduced system costs.

Finally, an acoustic camera with cheap analogue MEMS microphones was constructed for sound source localisation and quantification on UAVs. Moreover, an acoustic GPS was made for efficient microphone position calibrations. Five tests were conducted to validate the workings of all

equipment and show its correct functioning. All signal processing and programming were performed in Python, MatLab, and LabView, resulting in fully functional measurement equipment and editable code. Hence, these measurement devices can be customized and used in further studies.

Bibliography

[1] A brief history of drones. [Online]. Available: https://www.iwm.org.uk/history/a-brief-history-of-drones

[2] M. Dr. Palik and M. Nagy, "Brief history of uav development," *Repüléstudományi Közlemények*, vol. 31, pp. 155–166, 05 2019.

[3] "Uav," 2023. [Online]. Available: https://dictionary.cambridge.org/dictionary/english/uav

[4] H. Shakhatreh, A. H. Sawalmeh, A. Al-Fuqaha, Z. Dou, E. Almaita, I. Khalil, N. S. Othman, A. Khreishah, and M. Guizani, "Unmanned aerial vehicles (uavs): A survey on civil applications and key research challenges," *IEEE Access*, vol. 7, pp. 48 572–48 634, 2019.

[5] A. A. Molina, Y. Huang, and Y. Jiang, "A review of unmanned aerial vehicle applications in construction management: 2016–2021," *Standards*, vol. 3, no. 2, pp. 95–109, 2023. [Online]. Available: https://www.mdpi.com/2305-6703/3/2/9

[6] A. Rejeb, A. Abdollahi, K. Rejeb, and H. Treiblmaier, "Drones in agriculture: A review and bibliometric analysis," *Computers and Electronics in Agriculture*, vol. 198, p. 107017, 2022. [Online]. Available: https://www.sciencedirect.com/science/article/pii/S0168169922003349

[7] F. Outay, H. A. Mengash, and M. Adnan, "Applications of unmanned aerial vehicle (uav) in road safety, traffic and highway infrastructure management: Recent advances and challenges," *Transportation Research Part A: Policy and Practice*, vol. 141, pp. 116–129, 2020. [Online]. Available: https://www.sciencedirect.com/science/article/pii/S096585642030728X

[8] W. Greenwood, J. Lynch, and D. Zekkos, "Applications of uavs in civil infrastructure," *Journal of Infrastructure Systems*, vol. 25, 01 2019.

[9] B. Aydin, "Public acceptance of drones: Knowledge, attitudes, and practice," *Technology in Society*, vol. 59, p. 101180, Nov 2019.

[10] O. Hänninen, A. B. Knol, M. Jantunen, T.-A. Lim, A. Conrad, M. Rappolder, P. Carrer, A.-C. Fanetti, R. Kim, J. Buekers, R. Torfs, I. Iavarone, T. Classen, C. Hornberg, O. C. Mekel, and null null, "Environmental burden of disease in europe: Assessing nine risk factors in six countries," *Environmental Health Perspectives*, vol. 122, no. 5, pp. 439–446, 2014. [Online]. Available: https://ehp.niehs.nih.gov/doi/abs/10.1289/ehp.1206154

[11] F. Theakston, *Burden of disease from environmental noise*, ser. Quantification of healthy life years lost in Europe. World Health Organization, 2011.

[12] B. Schäffer, R. Pieren, K. Heutschi, J. M. Wunderli, and S. Becker, "Drone noise emission characteristics and noise effects on humans—a systematic review," *International Journal of Environmental Research and Public Health*, vol. 18, no. 11, 2021. [Online]. Available: https://www.mdpi.com/1660-4601/18/11/5940

[13] C. Ramos-Romero, N. Green, A. J. Torija, and C. Asensio, "On-field noise measurements and acoustic characterisation of multi-rotor small unmanned aerial systems," *Aerospace Science and Technology*, vol. 141, p. 108537, 2023. [Online]. Available: https://www.sciencedirect.com/science/article/pii/S1270963823004340

[14] S. Hara, Y. Mitsukura, and H. Kamide, "Noise-induced stress assessment on the difference between questionnaire-based and eeg measurement-based evaluations," *Technical Journal of Advanced Mobility*, vol. 3, no. 6, pp. 81–90, 2022.

[15] K. Cussen, S. Garruccio, and J. Kennedy, "Uav noise emission—a combined experimental and numerical assessment," *Acoustics*, vol. 4, no. 2, p. 297–312, Mar 2022.

[16] EASA, "EASA publishes first guidelines on noise level measurements for drones below 600kg," October 2022. [Online]. Available: https://www.easa.europa.eu/en/newsroom-and-events/press-releases/easa-publishes-first-guidelines-noise-level-measurements-drones

[17] B. Schäffer, R. Pieren, K. Heutschi, J. M. Wunderli, and S. Becker, "Drone noise emission characteristics and noise effects on humans—a systematic review," *International Journal of Environmental Research and Public Health*, vol. 18, no. 11, p. 5940, Jun 2021.

[18] A. J. Torija, Z. Li, and R. H. Self, "Effects of a hovering unmanned aerial vehicle on urban soundscapes perception," *Transportation Research Part D: Transport and Environment*, vol. 78, p. 102195, Jan. 2020. [Online]. Available: https://linkinghub.elsevier.com/retrieve/pii/S1361920919309861

[19] H. Eißfeldt, V. Vogelpohl, M. Stolz, A. Papenfuß, M. Biella, J. Belz, and D. Kügler, "The acceptance of civil drones in germany," *CEAS Aeronautical Journal*, vol. 11, no. 3, p. 665–676, Apr 2020.

[20] N. S. Zawodny and N. A. Pettingill, "Acoustic wind tunnel measurements of a quadcopter in hover and forward flight conditions," 2018. [Online]. Available: https://ntrs.nasa.gov/api/citations/20200002564/downloads/20200002564.pdf

[21] K. Heutschi, B. Ott, T. Nussbaumer, and P. Wellig, "Synthesis of real world drone signals based on lab recordings," *Acta Acustica*, vol. 4, 11 2020.

[22] Y. Zhang, I. Lee, and D. Lin, "Measurement of noise from a moving drone using a phased array microphone system," 10 2017.

[23] I. Besnea, "Acoustic imaging and spectral analysis for assessing uav noise," 2020.

[24] R. E. Berg. Encyclopedia britannica: acoustics. [Online]. Available: https://www.britannica.com/science/acoustics

[25] M. E. Goldstein, *Aeroacoustics*. McGraw-Hill International Book Co., 1976.

[26] M. J. Lighthill, "On sound generated aerodynamically. i. general theory," *Proceedings of the Royal Society of London. Series A, Mathematical and Physical Sciences*, vol. 211, no. 1107, pp. 564–587, 1952. [Online]. Available: http://www.jstor.org/stable/98943

[27] M. A. M. Thomas F. Brooks, D. Stuart Pope, "Airfoil self-noise and prediction," *NASA Reference Publication*, vol. 86, p. 146, 07 1989.

[28] R. W. Paterson, P. G. Vogt, M. R. Fink, and C. L. Munch, "Vortex noise of isolated airfoils," *Journal of Aircraft*, vol. 10, no. 5, p. 296–302, 1973.

[29] T. Brooks and T. Hodgson, "Trailing edge noise prediction from measured surface pressures," *Journal of Sound and Vibration*, vol. 78, no. 1, pp. 69–117, 1981. [Online]. Available: https://www.sciencedirect.com/science/article/pii/S0022460X81801587

[30] S. Oerlemans, "Detection of aeroacoustic sound sources on aircraft and wind turbines," Ph.D. dissertation, UTwente, 2009.

[31] S. Glegg and W. Devenport, "Chapter 14 - leading edge noise," in *Aeroacoustics of Low Mach Number Flows*, S. Glegg and W. Devenport, Eds. Academic Press, 2017, pp. 345–364. [Online]. Available: https://www.sciencedirect.com/science/article/pii/B978012809651200014X

[32] ——, "Chapter 16 - open rotor noise," in *Aeroacoustics of Low Mach Number Flows*, S. Glegg and W. Devenport, Eds. Academic Press, 2017, pp. 399–436. [Online]. Available: https://www.sciencedirect.com/science/article/pii/B9780128096512000163

[33] H. H. Hubbard, *Aeroacoustics of flight vehicles: Theory and practice*. Published for the Acoustical Society of America through the American Institute of Physics, 1991.

[34] R. W. Paterson, R. K. Amiet, and C. L. Munch, "Isolated airfoil-tip vortex interaction noise," *Journal of Aircraft*, vol. 12, no. 1, p. 34–40, 1975.

[35] W. Villafana, "Rotorcraft noise abatement procedures development," Ph.D. dissertation, Pennsylvania State University, 12 2016.

[36] J. Niesten, M. Tenpierik, and J. Krimm, "Sound predictions in an urban context," *Building Acoustics*, vol. 29, no. 1, p. 1–52, Jul 2021.

[37] W. Zhou, Z. Ning, H. Li, and H. Hu, "An experimental investigation on rotor-to-rotor interactions of small uav propellers," 06 2017.

[38] A. Zarri, E. Dell'Erba, W. Munters, and C. Schram, "Aeroacoustic installation effects in multi-rotorcraft: Numerical investigations of a small-size drone model," *Aerospace Science and Technology*, vol. 128, p. 107762, 2022. [Online]. Available: https://www.sciencedirect.com/science/article/pii/S1270963822004369

[39] S. Dougherty, N. L. Oo, and D. Zhao, "Effects of propeller separation and onset flow condition on the performance of quadcopter propellers," *Aerospace Science and Technology*, vol. 145, p. 108837, Feb 2024.

[40] S. Glegg and W. Devenport, "Chapter 3 - linear acoustics," in *Aeroacoustics of Low Mach Number Flows*, S. Glegg and W. Devenport, Eds. Academic Press, 2017, pp. 49–72. [Online]. Available: https://www.sciencedirect.com/science/article/pii/B9780128096512000163

[41] N.A., "A weighting." [Online]. Available: https://academic-accelerator.com/encyclopedia/a-weighting

[42] L. K. Rimskaya-Korsakova, P. A. Pyatakov, and S. A. Shulyapov, "Evaluations of the Annoyance Effects of Noise," *Acoustical Physics*, vol. 68, no. 5, pp. 502–512, Oct. 2022. [Online]. Available: https://doi.org/10.1134/S1063771022050098

[43] D. A. Russell, J. P. Titlow, and Y.-J. Bemmen, "Acoustic monopoles, dipoles, and quadrupoles: An experiment revisited," *American Journal of Physics*, vol. 67, no. 8, p. 660–664, 1999.

[44] J.-F. Blais, "Proceedings of meetings on acoustics," Jun 2013.

[45] Rayleigh, "Xxxi. investigations in optics, with special reference to the spectroscope," *The London, Edinburgh, and Dublin Philosophical Magazine and Journal of Science*, vol. 8, no. 49, pp. 261–274, 1879. [Online]. Available: https://doi.org/10.1080/14786447908639684

[46] T. F. Brooks, *Effect of Directional Array Size on the Measurement of Airframe Noise Components*. NASA Langley Research Center, 1999.

[47] Z. Prime and C. Doolan, "A comparison of popular beamforming arrays," *Proceedings of ACOUSTICS 2013*, 2013.

[48] W. Humphreys, D. Lockard, M. Khorrami, W. Culliton, R. McSwain, P. Ravetta, and Z. Johns, "Development and calibration of a field-deployable microphone phased array for propulsion and airframe noise flyover measurements," in *22nd AIAA/CEAS Aeroacoustics Conference*, 05 2016.

[49] A. Lauterbach, K. Ehrenfried, L. Koop, and S. Loose, "Procedure for the accurate phase calibration of a microphone array," *15th AIAA/CEAS Aeroacoustics Conference (30th AIAA Aeroacoustics Conference)*, May 2009.

[50] D. Ernst, T. Ahlefeldt, S. Haxter, and C. Spehr, "Microphone localization with self calibrating acoustic gps," *23rd AIAA/CEAS Aeroacoustics Conference*, Jun 2017.

[51] Faro quantum max scanarms. [Online]. Available: https://www.faro.com/en/Products/Hardware/ScanArms

[52] W. Gander, "Chapter 23. least squares fit of point clouds," *Solving Problems in Scientific Computing Using Maple and MATLAB*, Jun 2004.

[53] B. Henderson, D. Huff, J. Cluts, and C. Ruggeri, "Electric motor noise from small quadcopters: Part ii – source characteristics," 2018. [Online]. Available: https://ntrs.nasa.gov/api/citations/20180005580/downloads/20180005580.pdf

[54] M. Born, E. Wolf, A. B. Bhatia, P. C. Clemmow, D. Gabor, A. R. Stokes, A. M. Taylor, P. A. Wayman, and W. L. Wilcock, *Principles of Optics: Electromagnetic Theory of Propagation, Interference and Diffraction of Light*, 7th ed. Cambridge University Press, 1999.

Appendix A

Appendix

A.1 Balance equations

The modelling of many physical phenomena assumes that one cannot create something from nothing. Therefore, specific physical quantities have to be balanced within a bounded volume. Three transported quantities are considered within the framework of continuum fluid mechanics. These quantities are mass, momentum, and energy. The derivation of the mass and momentum balance is discussed. Along with the results from the conservation of energy, they are used to derive the wave equation in section 3.1.

Mass balance

Assume a medium in which an infinitesimally small arbitrary control volume can accurately describe the transfer of mass, momentum, and energy. We define the volume as large with respect to the molecular length scales but small with respect to other length scales of our problem. The control volume V_c for which the mass and momentum balance equations are derived is given in Figure A.1.1 where the bounding surface is expressed as S_c and the unit outward normal vector as n_i.

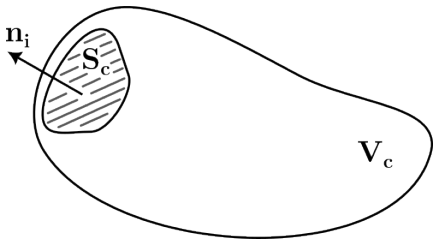

Figure A.1.1: A control volume V_c

The mass contained in the control volume is given by a volume integral of the mass density as $m = \int_{V_c} \rho \, dV$. Where ρ is the (possibly time-varying and inhomogeneous) mass density in the volume. The outward mass flux, defined as the mass exiting the domain per unit of time, is defined as $\frac{d}{dt}m = \int_{S_c} \rho u_i n_i \, dS$. Where u_i is the velocity vector on the boundary of the surface.

In the absence of mass sources, mass change per unit of time is only a function of mass flux over the boundary. Therefore, we can write $\frac{d}{dt}\int_{V_c} \rho \, dV = -\int_{S_c} \rho u_i n_i \, dS$.

The integral formulation can be rewritten into the differential form using the divergence theorem, resulting in the mass continuity equation, given in Equation A.1.1.

$$\frac{\partial \rho}{\partial t} + \frac{\partial (\rho u_i)}{\partial x_i} = 0 \tag{A.1.1}$$

Momentum balance

The momentum balance equation can be derived similarly to the mass balance equation. The total momentum within the control volume V_c can be mathematically written as $\int_{V_c} \rho u_i \, dV$.

According to Newton's second law (i.e. axiom), the momentum rate of change is equal to the net sum of external forces applied to the control volume. Mathematically, this can be written as $\frac{d}{dt}\int_{V_c} \rho u_i \, dV = \sum_i F_{ext,i}$. The external forces, expressed with $\sum_i F_{ext,i}$, consist of two types of forces. Firstly, body forces. Forces that act throughout the entire volume. Examples of body forces are gravity or magnetic forces. Secondly, pressure and friction exert surface forces on the volume's boundary.

$$\sum_i F_{ext,i} = \int_{S_c} \sigma_{ij} n_j \, dS + \int_{V_c} f_i \, dV \tag{A.1.2}$$

In which σ_{ij} denotes Cauchy's stress tensor and f_i the density of the body forces in V_c. Using the formulation for the external forces in the balance of momentum results in Equation A.1.3.

$$\frac{d}{dt}\int_{V_c} \rho u_i \, dV = \int_{S_c} \sigma_{ij} n_j \, dS + \int_{V_c} f_i \, dV \tag{A.1.3}$$

Reynold's transport theorem can be used to include the time derivative in the first term in the integral. This theorem states that $\frac{d}{dt}\int_{V_c(t)} \mathbf{f} \, dV = \int_{V_c(t)} \frac{\partial \mathbf{f}}{\partial t} \, dV + \int_{S_c(t)} (u_i n_i)\mathbf{f} \, dS$, where $\mathbf{f}$ may be tensor-, vector-, or scalar-valued. This results in Equation A.1.4.

$$\int_{V_c} \frac{\partial(\rho u_i)}{\partial t} \, dV + \int_{S_c} (u_j n_j)(\rho u_i) \, dS = \int_{S_c} \sigma_{ij} n_j \, dS + \int_{V_c} f_i \, dV \tag{A.1.4}$$

Reorganising terms and using the divergence theorem results in Equation A.1.5.

$$\int_{V_c} \Big(\frac{\partial(\rho u_i)}{\partial t} - \frac{\partial}{\partial x_j}(\sigma_{ij} + \rho u_i u_j) - f_i \Big) \, dV = 0 \tag{A.1.5}$$

As long as the volume is not of size zero, this equation can only be true when the integrand is equal to zero. This yields the differential formulation of the momentum balance equation, as is given in Equation A.1.6

$$\frac{\partial(\rho u_i)}{\partial t} + \frac{\partial}{\partial x_j}(\sigma_{ij} + \rho u_i u_j) - f_i = 0 \tag{A.1.6}$$

The momentum balance consists of only 3 equations while having many unknowns. However, the number of unknowns can be reduced when considering specific applications. For example, if the fluid under consideration is said to be a *simple fluid*, Cauchy's stress tensor, defined by $\sigma_{ij} = -\delta_{ij} p + \tau_{ij}$, can reduce in unknowns using $\sigma_{ij} = \sigma_{ji}$. Furthermore, when considering a *Newtonian fluid*, τ_{ij} can be related to the velocity and dynamic viscosity μ in the fluid: $\tau_{ij} = \mu(\frac{\partial u_i}{\partial x_j} - \frac{\partial u_j}{\partial x_i}) - \frac{2}{3}\mu\delta_{ij}\frac{\partial u_k}{\partial x_k}$.

A.2 Green's functions for a solution to the inhomogeneous wave equation

Using the method of Green's functions, a solution to the inhomogeneous wave equation in 3.1.15 can be constructed. Green's function is defined as the response of the inhomogeneous equation for a unit impulse in the domain. Using this impulse response, one can solve for the acoustic field without numerically solving the inhomogeneous second-order PDE (also in an initial value problem). This domain can still include objects and surfaces to reflect and generate sound [40].

The unit impulse is defined by Equation A.2.7 at a position $\mathbf{y}$ at time τ, which is plugged into Equation 3.1.15 to obtain Equation A.2.8 in which G gives the solution of the equation.

$$q = \delta(\mathbf{x} - \mathbf{y})(t - \tau) \tag{A.2.7}$$

$$\frac{1}{c_0^2}\frac{\partial^2 G}{\partial \tau^2} - \frac{\partial^2 G}{\partial y_i^2} = \delta(\mathbf{x} - \mathbf{y})(t - \tau) \tag{A.2.8}$$

This equation shows us that the solution depends on the observer and source positions $\mathbf{x}$ and $\mathbf{y}$, as well as the time of observation and excitation, t and τ. Therefore, Green's function is often expressed as $G(\mathbf{x}, t|\mathbf{y}, \tau)$.

Multiplying Equation A.2.8 with p', Equation 3.1.15 with G, and subtracting them yields Equation A.2.9.

$$\frac{1}{c_0^2}\Big(p'\frac{\partial^2 G}{\partial \tau^2} - G\frac{\partial^2 p'}{\partial \tau^2}\Big) - \Big(p'\frac{\partial^2 G}{\partial y_i^2} - G\frac{\partial^2 p'}{\partial y_i^2}\Big) = \delta(\mathbf{x} - \mathbf{y})\delta(t - \tau)p' - Gq \tag{A.2.9}$$

By integrating both sides over a time T (between t_0 and t_1) and an observable volume V enclosing all sources (and surfaces), we obtain Equation A.2.10.

$$\int_V \int_{t_0}^{t_1} \frac{1}{c_0^2}\Big(p'\frac{\partial^2 G}{\partial \tau^2} - G\frac{\partial^2 p'}{\partial \tau^2}\Big)\, d\tau\, dV_y - \int_V \int_{t_0}^{t_1} \Big(p'\frac{\partial^2 G}{\partial y_i^2} - G\frac{\partial^2 p'}{\partial y_i^2}\Big)\, d\tau\, dV_y = p' - \int_V \int_{t_0}^{t_1} Gq\, d\tau\, dV_y \tag{A.2.10}$$

Rewriting this equation into a simplified form using the divergence theorem and reordering of terms yields Equation A.2.11.

$$\int_V \frac{1}{c_0^2}\Big[p'\frac{\partial G}{\partial \tau} - G\frac{\partial p'}{\partial \tau}\Big]_{\tau=t_0}^{\tau=t_1} dV_y - \int_{t_0}^{t_1}\int_S \Big(p'\frac{\partial G}{\partial y_i} - G\frac{\partial p'}{\partial y_i}\Big) n_i\, dS_y\, d\tau = p' - \int_V \int_{t_0}^{t_1} Gq\; d\tau dV_y \tag{A.2.11}$$

If we specify the initial condition that $p' = 0$ and $\partial p'/\partial \tau = 0$ at $\tau = t_0$, then the integrand of the first term is zero at its lower limit. If we also constrain the Green's function by setting $G = 0$ and $\partial G/\partial \tau = 0$ at $\tau = t_1$, the full integral is zero and can be ignored. This condition is called the *causality condition* and states that a sound heard at t, should have been produced at time $\tau < t$. This already simplifies Equation A.2.11 to Equation A.2.13.

A second important property of the Green's function is its *reciprocity relation*, which states that the perceived pressure perturbations are the same when interchanging the observer and source or the observer time and emission time [40]. This is mathematically given by Equation A.2.12.

$$G(\mathbf{x}, t|\mathbf{y}, \tau) = G(\mathbf{y}, -\tau|\mathbf{x}, -t) \tag{A.2.12}$$

$$p'(\mathbf{x}, t) = \int_V \int_{t_0}^{t_1} Gq \; d\tau dV_y - \int_{t_0}^{t_1} \int_S \Big(p' \frac{\partial G}{\partial y_i} - G \frac{\partial p'}{\partial y_i} \Big) n_i \, dS_y \, d\tau \tag{A.2.13}$$

When Green's function and the pressure perturbations satisfy the same boundary conditions at the boundary of V, we specify the Green's function as a *tailored Green's function*. When dealing with a tailored Green's function, the second term in Equation A.2.13 vanishes, and we are left with Equation A.2.14.

$$p'(\mathbf{x}, t) = \int_V \int_{t_0}^{t_1} Gq \; d\tau dV_y \tag{A.2.14}$$

For radiation from an infinitely small volume displacement source in an unbounded domain, Green's function is known as the free field Green's function and is given by Equation A.2.15.

$$G_0(\mathbf{x}, t|\mathbf{y}, \tau) = \frac{\delta(t - \tau - r/c_0)}{4\pi r} \tag{A.2.15}$$

Where the distance between source and observer is defined by $r = |\mathbf{x} - \mathbf{y}|$. By substituting Equation A.2.15 into Equation A.2.14, the pressure field due to an infinitely small volume displacement source is given and shown in Equation A.2.16.

$$p'(\mathbf{x}, t) = \int_V \frac{q(\mathbf{y}, t - r/c_0)}{4\pi r} dV_y \tag{A.2.16}$$

Because the free-field Green's function in Equation A.2.15 is of such importance in the methods of source localisation, it is often also considered in the frequency domain by applying the Fourier transform defined by Equation A.2.17 to $2\pi G(\mathbf{x}, t|\mathbf{y}, 0)$ to obtain Equation A.2.18.

$$\tilde{q}(\omega) = \frac{1}{2\pi} \int_{-T}^{T} q(t) e^{i\omega t} \, dt \tag{A.2.17}$$

$$\tilde{G}_0(\mathbf{x}|\mathbf{y}) = \frac{e^{ikr}}{4\pi r} \tag{A.2.18}$$

Equation A.2.18 describes the free-field Green's function in the frequency domain where $k = 2\pi/\lambda$ is the wave number, and λ is the wavelength.

A.2.1 Simple sources in a medium

Now that a description of the pressure field in the medium due to a source is known, a closer look is taken at different types of sources and the resulting radiation patterns. Firstly, stationary sources are discussed where *monopoles* and *dipoles* are touched upon. Secondly, the resulting pressure field of a moving source and the apparent frequency and amplitude shift are discussed.

Stationary sources

To illustrate the result of a stationary simple source in the domain, let us consider a point source in ξ, such that its source power distribution q equals Equation A.2.19.

$$q(\mathbf{y}, t) = \sigma(t)\delta(\mathbf{y} - \xi) \tag{A.2.19}$$

Where the time-dependent source strength is given by $\sigma(t)$. Substituting Equation A.2.19 into Equation A.2.16 results in the radiated pressure field, which is given in Equation A.2.20.

$$p'(\mathbf{x}, t) = \frac{\sigma(t - r/c_0)}{4\pi r} \tag{A.2.20}$$

It is evident that the amplitude of the source is inversely proportional to the distance and is evenly radiated in all directions. Such a source is known as a *monopole*. In practice, any sound source that is acoustically compact (smaller than the radiated wavelength) acts as a monopole. The compactness of a source is related to $kL \ll 1$, where L is the characteristic length scale of the source [43]. Such a monopole is often considered a pulsating sphere, radiating sound in an omnidirectional manner.

Also worth mentioning is that the models of these sources are only valid in the acoustic far-field. This acoustic far-field is defined as the acoustic domain at a distance r from the sound source such that $kr \gg 1$. In contrast, radiation, absorption, and reflections of sound play an important role in the acoustic near-field of a source, making the acoustic near-field very complex. However, in the acoustic far-field wave propagation prevails, being well described by the wave equation [30].

The output of a monopole source in Equation A.2.20 is often described in polar coordinates, which is given by Equation A.2.21 [43].

$$p'(r, \theta, t) = i\frac{Q\rho ck}{4\pi r}e^{i(\omega t - kr)} \tag{A.2.21}$$

$$|p(r, \theta, t)| = \frac{Q\rho ck}{4\pi r} \tag{A.2.22}$$

Where Q is the source strength, ρ is the density of the fluid, ω is the source frequency, and k is the wave number defined as $k = \omega/c_0$. The absolute value of this equation represents the pressure amplitude at any point in the medium due to a point source, given as Equation A.2.22. The equation shows the uniform radiation of a wave invariable of θ, where the wave amplitude is inversely proportional to the distance between the source and observer. The radiation pattern is graphically shown in Figure A.2.2a.

Combining multiple coherent monopoles can create more complex sound sources. For example, separating two monopole sources with a phase difference of 180° by a distance d, such that $kd \ll 1$, yields an acoustic dipole. This is one of the more straightforward multi-pole sources, for which the far-field pressure fluctuations are given by Equation A.2.23 [43].

$$p'(r,\theta,t) = -i\frac{Q\rho ck^2 d}{4\pi r}\cos(\theta)e^{i(\omega t - kr)} \tag{A.2.23}$$

$$|p'(r,\theta,t)| = \frac{Q\rho ck^2 d}{4\pi r}\cos(\theta) \tag{A.2.24}$$

In contrast to a monopole, there is no net volume injection, and the radiated pressure fluctuations are dependent on θ (non-uniform radiation). One can observe that the maximum wave amplitude is found at $\theta = 0°$, while the amplitude is zero at $\theta = 90°$. The radiation pattern of an acoustic dipole is given in Figure A.2.2b.

In theory, additional coherent monopole sources can yield increasingly complex multi-pole sources. The radiation patterns of monopoles, dipoles and two different types of quadrupoles are given in Figure A.2.2.

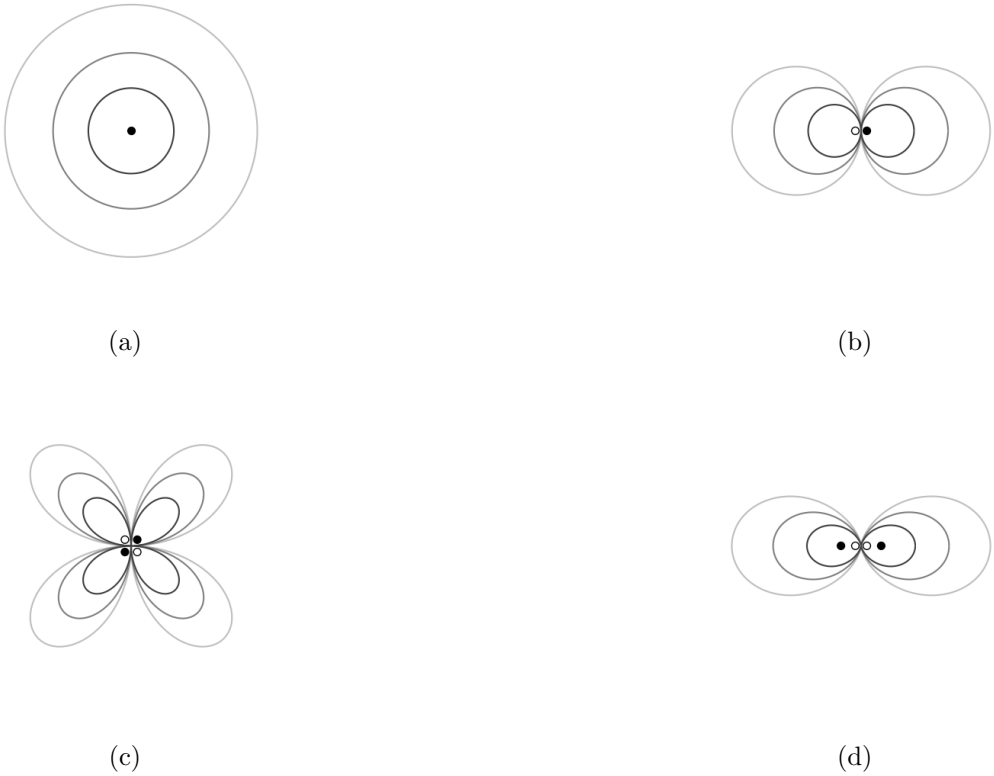

(a) (b)

(c) (d)

Figure A.2.2: Different types of simple sources and their directivity patterns. (a) Shows a monopole source, while (b) shows a dipole source. (c) Shows a lateral quadrupole, while (d) shows a longitudinal quadrupole.

Moving sources

In many practical situations, a source might be moving with respect to the observer. This can alter the perceived sound between the observer and the source. To show this, let us consider a moving point source in a stagnant medium such that its source power distribution is defined by Equation A.2.25.

$$q(\mathbf{y}, \tau) = \sigma(\tau)\delta(\mathbf{y} - \xi(\tau)) \tag{A.2.25}$$

We should consider the sound the observer perceives at time t radiated by the source at time τ. Therefore, the observed pressure perturbations can be defined by Equation A.2.26.

$$p'(\mathbf{x}, t) = \int_V \int_{t_0}^{t_1} \frac{\sigma(\tau)}{4\pi|\mathbf{r}'|}\delta(\mathbf{y} - \xi(\tau))\delta(t - \tau - |\mathbf{r}'|/c_0)\, d\tau\, dV_y \tag{A.2.26}$$

Where $\mathbf{r}'$ is the vector between source and observer at the moment the sound is radiated, i.e. $\mathbf{r}'(\tau) = \mathbf{x} - \xi(\tau)$. Equation A.2.26 can be simplified to Equation A.2.27, assuming that the source lies within the volume under consideration.

$$p'(\mathbf{x}, t) = \int_{t_0}^{t_1} \frac{\sigma(\tau)}{4\pi|\mathbf{r}'|}\delta(t - \tau - |\mathbf{r}'|/c_0)\, d\tau \tag{A.2.27}$$

To further solve this equation, one of the properties of the Dirac function is taken advantage of, given in Equation A.2.28. For this equation to be valid, the function $g(\tau)$ should only contain simple zeros, i.e. $(dg/d\tau)_{\tau=\tau_i} \neq 0$ when $g(\tau) = 0$.

$$\int_{-\infty}^{\infty} f(\tau)\delta\Big(g(\tau)\Big)\, d\tau = \sum_i \frac{f(\tau_i)}{|dg(\tau)/d\tau|_{\tau=\tau_i}} \tag{A.2.28}$$

Where τ_i is the i^{th} root of $g(\tau) = 0$. In our case, $g(\tau) = t - \tau - |\mathbf{r}'|/c_0 = 0$ and only has a single solution for a subsonic source velocity, i.e. $\tau_1 = t - |\mathbf{r}'|/c_0$ [30]. Substituting Equation A.2.27 into Equation A.2.28 yields Equation A.2.29.

$$p'(\mathbf{x}, t) = \frac{\sigma(\tau_1)}{4\pi|\mathbf{r}'|_{\tau_1}} \frac{1}{|d(t - \tau - |\mathbf{r}'|/c_0)/d\tau|_{\tau=\tau_1}} \tag{A.2.29}$$

The rate of change of $|\mathbf{r}'|/c_0$ is defined by Equation A.2.30 using Figure A.2.3.

$$\frac{d(|\mathbf{r}'|/c_0)}{d\tau} = \frac{\mathbf{u}}{c_0} \cdot \frac{\mathbf{r}'}{|\mathbf{r}'|} = -M\cos(\varphi) \tag{A.2.30}$$

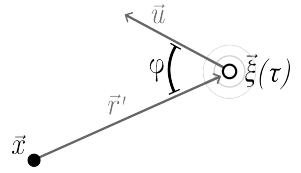

Figure A.2.3: A moving source with velocity $\mathbf{u}$ in $\xi(\tau)$ with an observer at $\mathbf{x}$.

φ is the angle between source velocity and source-observer line, while $M = |\mathbf{u}|/c_0$ is the absolute source velocity. Substituting Equation A.2.30 into Equation A.2.29, yields Equation A.2.31.

$$p'(\mathbf{x}, t) = \frac{\sigma(\tau_1)}{4\pi|\mathbf{r}'|_{\tau_1}} \frac{1}{|-1 + M_{\tau_1} \cos(\varphi_{\tau_1})|} \tag{A.2.31}$$

The subscripts denoting τ_1 indicate that these variables should be considered at the time of emission but are left out in the following equations for readability. For subsonic source velocities, the equation can be simplified further into Equation A.2.32 in which $\mathbf{r}'$, M, and φ are all considered at the source emission time.

$$p'(\mathbf{x}, t) = \frac{\sigma(\tau_1)}{4\pi|\mathbf{r}'|(1 - M\cos(\varphi))} \tag{A.2.32}$$

The resulting equation shows that the term $(1 - M\cos(\varphi))^{-1}$ either amplifies or attenuates the pressure fluctuation amplitude. In an approaching source, i.e. $-\pi/2 < \varphi < \pi/2$, the pressure is amplified since $(1 - M\cos(\varphi))^{-1} > 1$. In contrast, when the source recedes, the amplitude of the fluctuations is attenuated. This effect on amplitude is called *convective-* or *Doppler amplification*. The frequency of the perceived sound equals $f d\tau_1/dt$, where f is the signal's source frequency (frequency of σ) [30]. Using $\tau_1 = t - |\mathbf{r}'|/c_0$ and Equation A.2.30 yields Equation A.2.33.

$$\begin{aligned} \frac{d\tau_1}{dt} &= 1 - \frac{1}{c_0}\frac{d|\mathbf{r}'|}{d\tau_1}\frac{d\tau_1}{dt} \\ &= 1 + M\cos(\varphi)\frac{d\tau_1}{dt} \end{aligned} \tag{A.2.33}$$

Which finally results in Equation A.2.34.

$$\frac{d\tau_1}{dt} = \frac{1}{1 - M\cos(\varphi)} \tag{A.2.34}$$

Therefore, the observed frequency from a moving source with frequency f is observed by a stationary observer as $f/(1 - M\cos(\varphi))$. The observed frequency is higher than the radiated frequency for approaching sources, while for receding sources it is lower. A practical example is to listen to the sirens of emergency vehicles. As the vehicles pass the stationary observer (you), the observed frequency of the sound seems to increase as the vehicle approaches and decreases when it recedes. Even though the frequency of the sirens does not seem to change anymore as these vehicles come to a halt.

A.2.2 Interference and coherence of waves

In the previous sections, a simple source model is derived from the linear inhomogeneous wave equation. This model shows that the radiation of sources in the medium can be described using the simple monopole model. Using this approach of adding multiple sources into a free-field domain means that there is no longer a need to solve the complex wave equation in Equation 3.1.15 when considering the acoustic far-field.

However, when multiple sources are present in the medium, the waves of both sources start to interfere. Locally, this can cause wave reinforcement or cancellation, referred to as constructive and destructive interference. Constructive wave interference happens when the peaks of waves are aligned and combined to increase the amplitude. In contrast, destructive interference occurs when the troughs of one wave align with the peaks of another wave, cancelling each other. The alignment of these waves, called the phase difference, is an important variable in the interference between sources.

In reality, the amplitude and phase of a source undergoes rapid fluctuations. If the acoustic wave from a single source is split into two beams, the fluctuation between these beams is correlated due to a similar origin. However, if the two beams originate from two distinct sources, the fluctuations from the beams are uncorrelated, and the beams are said to be mutually incoherent. If the fluctuations are completely uncorrelated and the beams are superimposed, no interference is observed [54].

A.3 Experimental validation of the conventional beamforming algorithm

Sound sources and their respective levels can be found in a domain using conventional beamforming. To show this, a simple test setup was constructed in the anechoic chamber at the University of Twente. These tests were performed with a CAE microphone array, a laptop for data acquisition, a loudspeaker with a converging duct, a power supply, and measurement equipment to measure the loudspeaker's position in front of the acoustic camera. The loudspeaker is placed behind a converging duct to simulate a monopole sound source, as is shown in Figure A.3.4a.

Thirty-seven measurements were performed at different positions and orientations in the anechoic chamber.

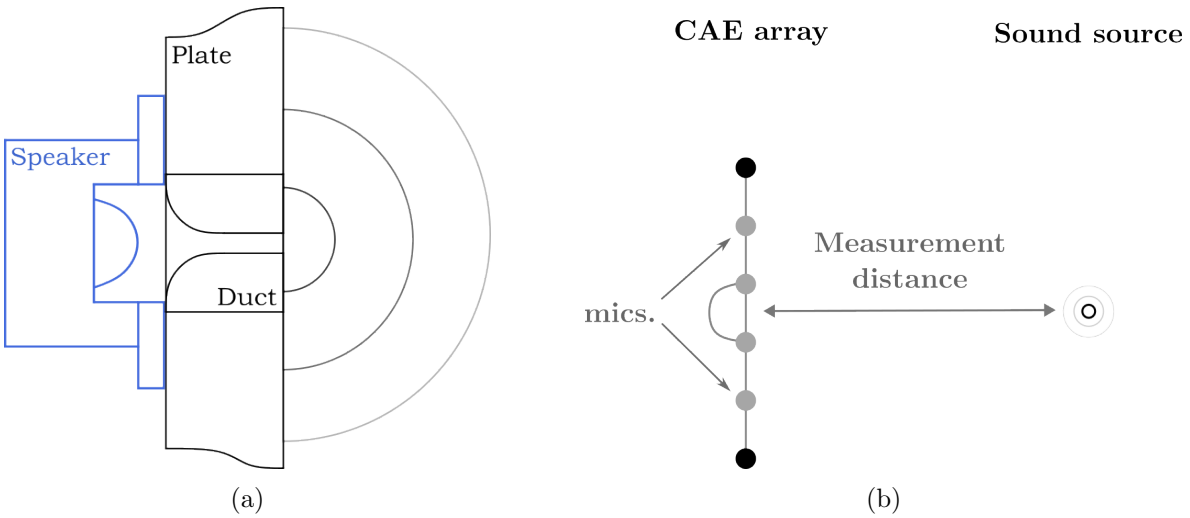

Figure A.3.4: (a) The converging duct used in the measurements to simulate a monopole sound source [49]. (b) A schematic of the measurement setup with the commercially available CAE microphone array.

Data acquisition and beamforming settings

The sampling frequency was set to 47 998 Hz for a total of 10 s. The CSM was constructed with the power spectral density using Welch's method (*hanning* window of 1024 samples and 50 % overlap). Diagonal removal was enabled.

A rectangular search grid was chosen between -0.75 m and 0.75 m (in both x and y direction). The resolution in both x and y direction was chosen to be 0.005 m. The output maps are given in dB SPL, for which the dynamic range is set to 20 dB. In addition to the measured output map, a simulated output map from a monopole source is also calculated for comparison.

Results

Figure A.3.5 until Figure A.3.7 show the resulting output maps at different frequencies and source positions. The output maps all show a main lobe at the position of the source with many artificial side lobes surrounding it. However, the experimental results are dissimilar to the simulation results, especially when looking at the side lobes of the figures. Looking, for example, at 4 kHz at 2 m in Figure A.3.6, the sidelobe in the experimental results show a misformed circle. Also, the noise floor of the experiments is higher than the simulation results.

Noteworthy is the fact that the beam width decreases as the observed frequency increases. The same is true for the distance between the array and the source; as the array is moved away from the source, the beam width increases and the accuracy of the array deteriorates. This is supported by Rayleigh's criterion in Equation 4.2.10. Finally, it is not visible in Figure A.3.7; however, the spatial resolution is decreased if the source is not positioned in front of the array, this is due to a reduced effective aperture size.

Conclusion

Using conventional beamforming techniques, one can retrieve the position of a source in a domain. Also, Rayleigh's criterion can be supported through beamforming experiments. It is shown that the spatial accuracy of an acoustic camera deteriorates as the frequency decreases and the distance to the source increases. Furthermore, the spatial resolution also deteriorates when the effective aperture of the array decreases.

To accommodate measurements on (relatively small) UAVs with closely spaced rotors the spatial resolution of the array has to be sufficient. Increasing the array's diameter can do this according to Equation 4.2.10.

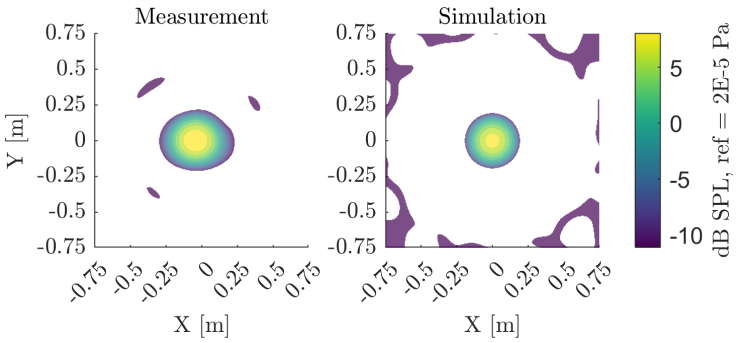

(a) Frequency of 4 kHz

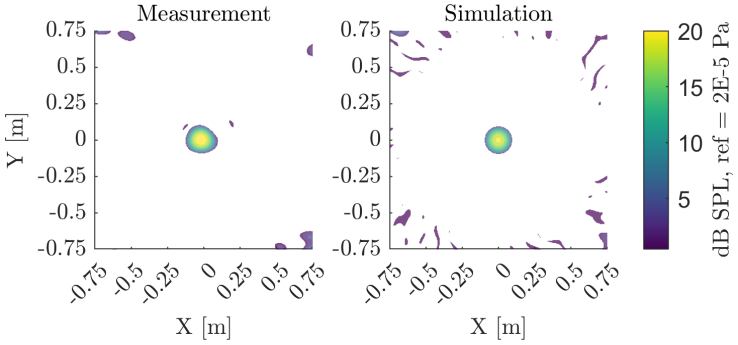

(b) Frequency of 8 kHz

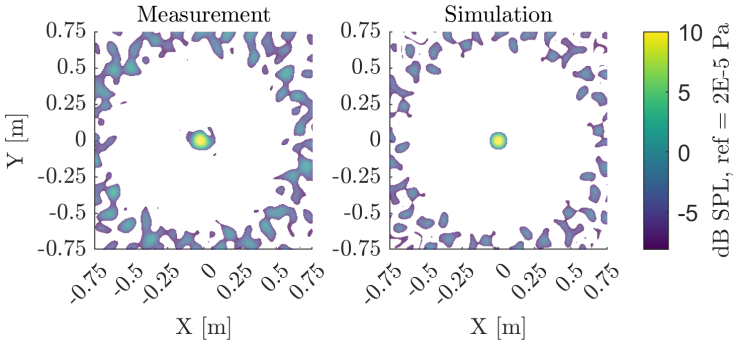

(c) Frequency of 12 kHz

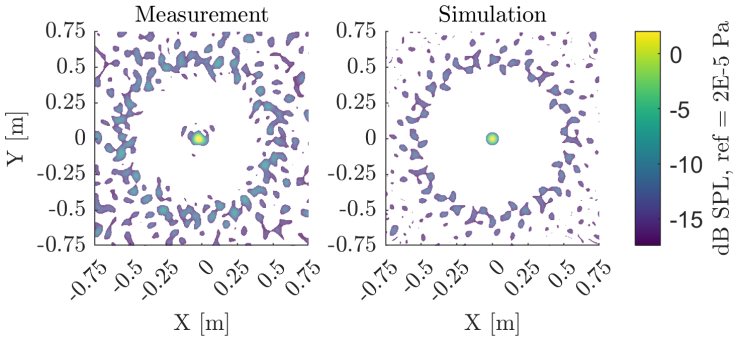

(d) Frequency of 16 kHz

Figure A.3.5: The output maps of the conventional beamforming algorithm at 2 m from the source.

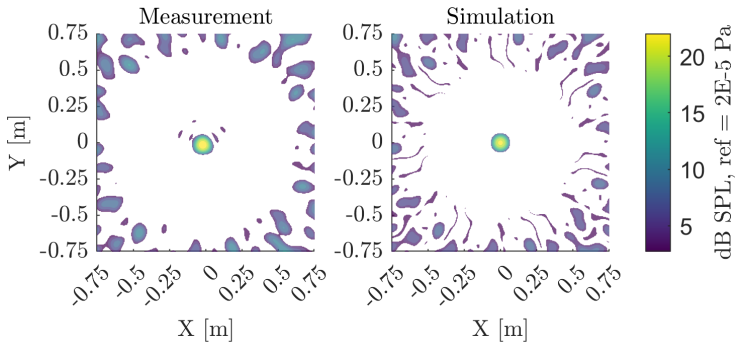

(a) Distance of 1.4 m

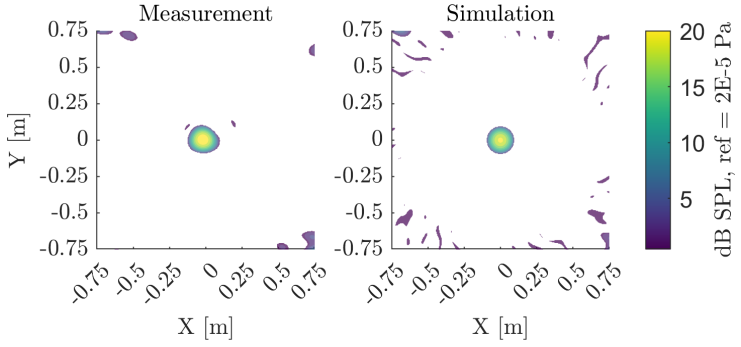

(b) Distance of 2 m

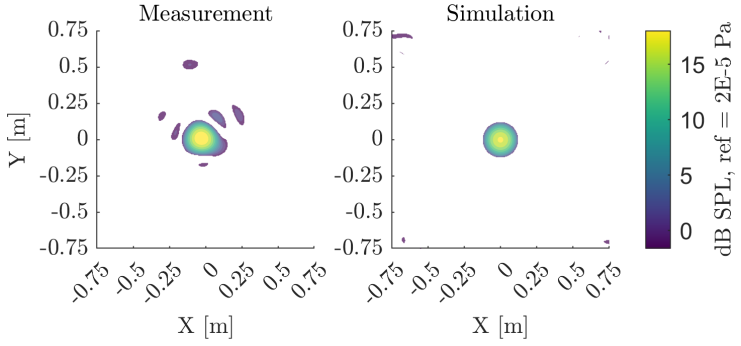

(c) Distance of 2.6 m

Figure A.3.6: The output maps of the conventional beamforming algorithm at 8 kHz.

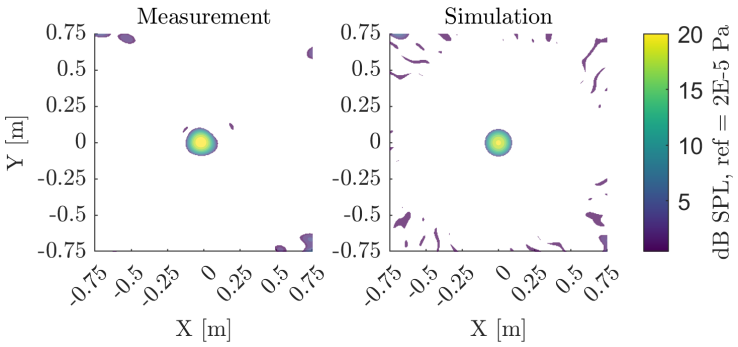

(a) Source position = $[0, 0, 2]$ m

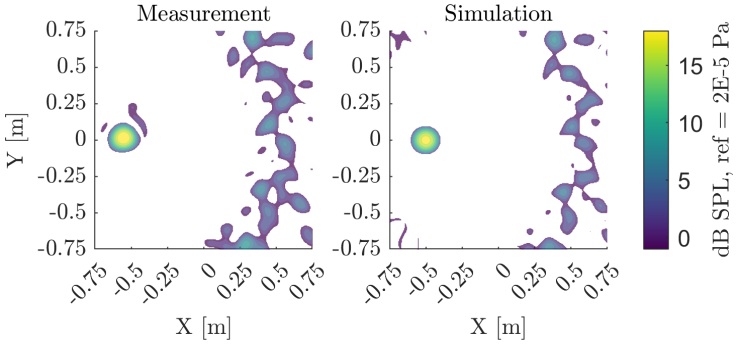

(b) Source position = $[-0.5, 0, 2]$ m

Figure A.3.7: The output maps of the conventional beamforming algorithm, comparing with a misaligned source at 8 kHz.

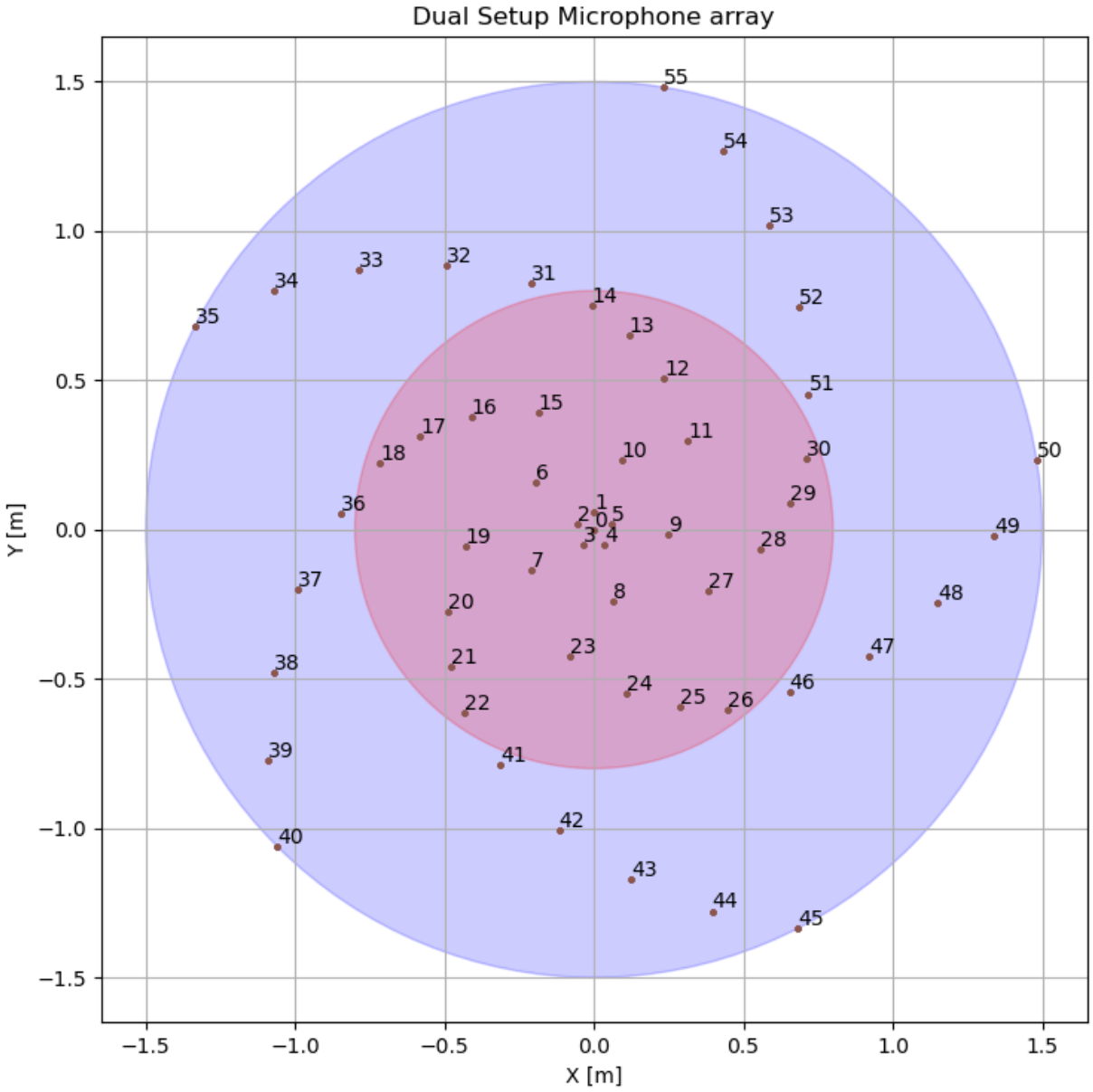

Figure A.3.8: The microphone arrangement of the ground positioned microphone array. Indices are given and are related to the coordinates in Table A.3.1 and Table A.3.2.

Microphone index	X in m	Y in m	Z in m
0	0.000000	0.000000	0.000000
1	0.000000	0.060000	0.000000
2	-0.057063	0.018541	0.000000
3	-0.035267	-0.048541	0.000000
4	0.035267	-0.048541	0.000000
5	0.057063	0.018541	0.000000
6	-0.192556	0.159443	0.000000
7	-0.211143	-0.133861	0.000000
8	0.062063	-0.242174	0.000000
9	0.249500	-0.015811	0.000000
10	0.092136	0.232402	0.000000
11	0.314218	0.297938	0.000000
12	0.232902	0.508189	0.000000
13	0.117083	0.650993	0.000000
14	-0.007582	0.749962	0.000000
15	-0.186257	0.390907	0.000000
16	-0.411346	0.378543	0.000000
17	-0.582950	0.312520	0.000000
18	-0.715599	0.224540	0.000000
19	-0.429331	-0.056344	0.000000
20	-0.487128	-0.274237	0.000000
21	-0.477366	-0.457845	0.000000
22	-0.434683	-0.611188	0.000000
23	-0.079084	-0.425730	0.000000
24	0.110284	-0.548030	0.000000
25	0.287922	-0.595484	0.000000
26	0.446950	-0.602275	0.000000
27	0.380455	-0.206771	0.000000
28	0.555288	-0.064464	0.000000
29	0.655312	0.089815	0.000000

Table A.3.1: The coordinates for each microphone, corresponding to the indices 0 until 29 in Figure A.3.8

Microphone index	X in m	Y in m	Z in m
30	0.710913	0.238961	0.000000
31	-0.210254	0.823586	0.000000
32	-0.495843	0.882777	0.000000
33	-0.787533	0.872019	0.000000
34	-1.070882	0.801323	0.000000
35	-1.336811	0.680394	0.000000
36	-0.848248	0.054539	0.000000
37	-0.992795	-0.198781	0.000000
38	-1.072700	-0.479520	0.000000
39	-1.093024	-0.770847	0.000000
40	-1.060191	-1.061129	0.000000
41	-0.313993	-0.789879	0.000000
42	-0.117738	-1.005631	0.000000
43	0.124568	-1.168378	0.000000
44	0.395356	-1.277732	0.000000
45	0.681577	-1.336208	0.000000
46	0.654190	-0.542711	0.000000
47	0.920029	-0.422733	0.000000
48	1.149687	-0.242578	0.000000
49	1.337367	-0.018835	0.000000
50	1.481429	0.235307	0.000000
51	0.718305	0.454465	0.000000
52	0.686347	0.744368	0.000000
53	0.585978	1.018457	0.000000
54	0.431183	1.266092	0.000000
55	0.233996	1.481636	0.000000

Table A.3.2: The coordinates for each microphone, corresponding to the indices 30 until 55 in Figure A.3.8

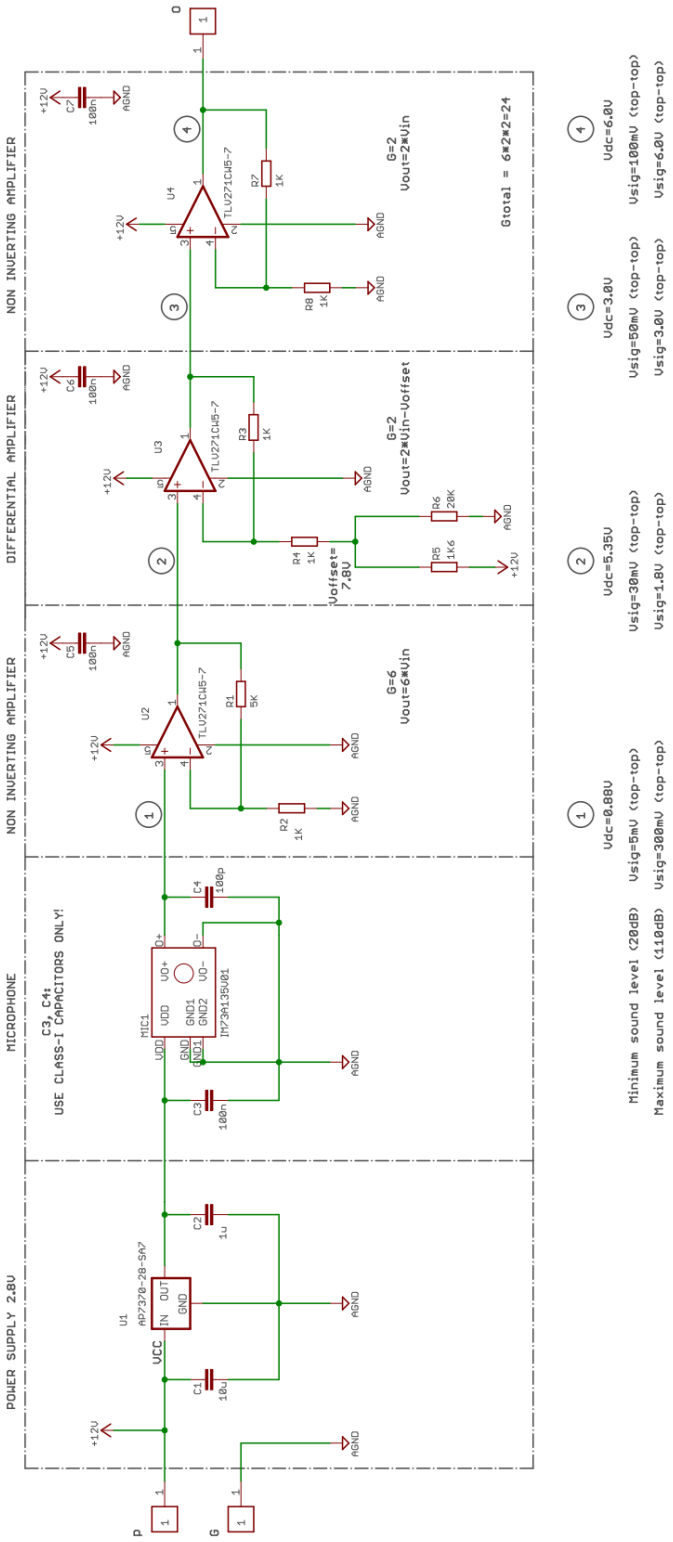

Figure A.3.9: The electrical wiring on the PCB for powering a MEMS microphone with signal amplification.

Microphone index	X in m	Y in m	Z in m
1	0	0	0
2	-0.3	-0.4	0
Loudspeaker index	X in m	Y in m	Z in m
1	0.200000	0.000000	0.000000
2	-0.135227	0.267794	0.000000
3	-0.376687	-0.134561	0.000000
4	-0.052843	-0.497200	0.000000
5	0.434865	-0.413391	0.000000

Table A.3.3: The assumed coordinates for both reference microphones and the five loudspeakers on the aGPS

Microphone index	X in m	Y in m	Z in m
1	0.0	0.0	0.0
2	-0.30232915	-0.3987271	0.0
Loudspeaker index	X in m	Y in m	Z in m
1	0.19992636	0.0	0.0
2	-0.13460529	0.26883295	0.0
3	-0.3771453	-0.13422524	0.0
4	-0.05520124	-0.49729877	0.0
5	0.43282856	-0.4145181	0.0

Table A.3.4: The coordinates for both reference microphones and the five loudspeakers on the aGPS, measured with a coordinate measurement machine

Figure A.3.10: The DJI Phantom 4 Pro, used in the measurements.

Properties	Values
Number of rotors	4
Number of blades	2
Rotor diameter	240 mm
Distance between front/aft motors	4 mm
Distance between left/right motors	10 mm
Max rotating speed	193 Hz
Max tip Mach number	0.42

Table A.3.5: Relevant information about the DJI Phantom 4 Pro, being used in the measurements of section 7.2 and section 7.3.

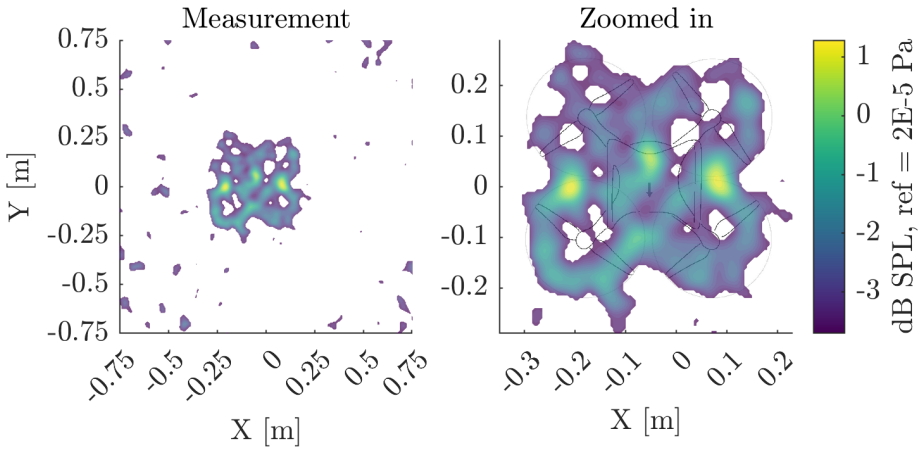

(a) Frequency of 7.5 kHz

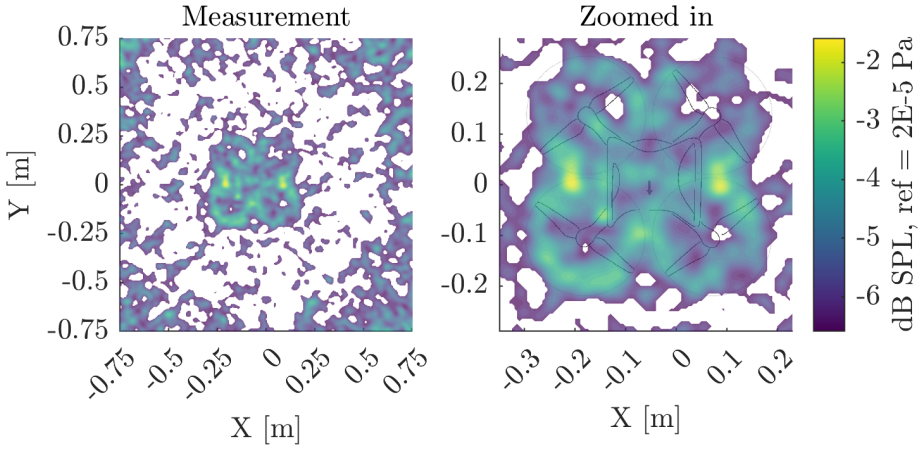

(b) Frequency of 8.7 kHz

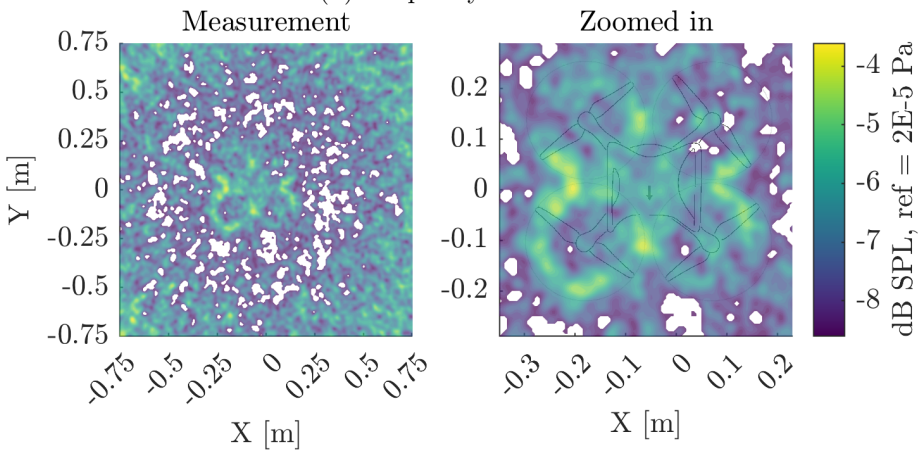

(c) Frequency of 10 kHz

Figure A.3.11: Follow up on the beamforming results section 7.2. The three output maps shown all show blade-induced noise. Increased levels are visible between the rotor-tips of the front and aft rotors.

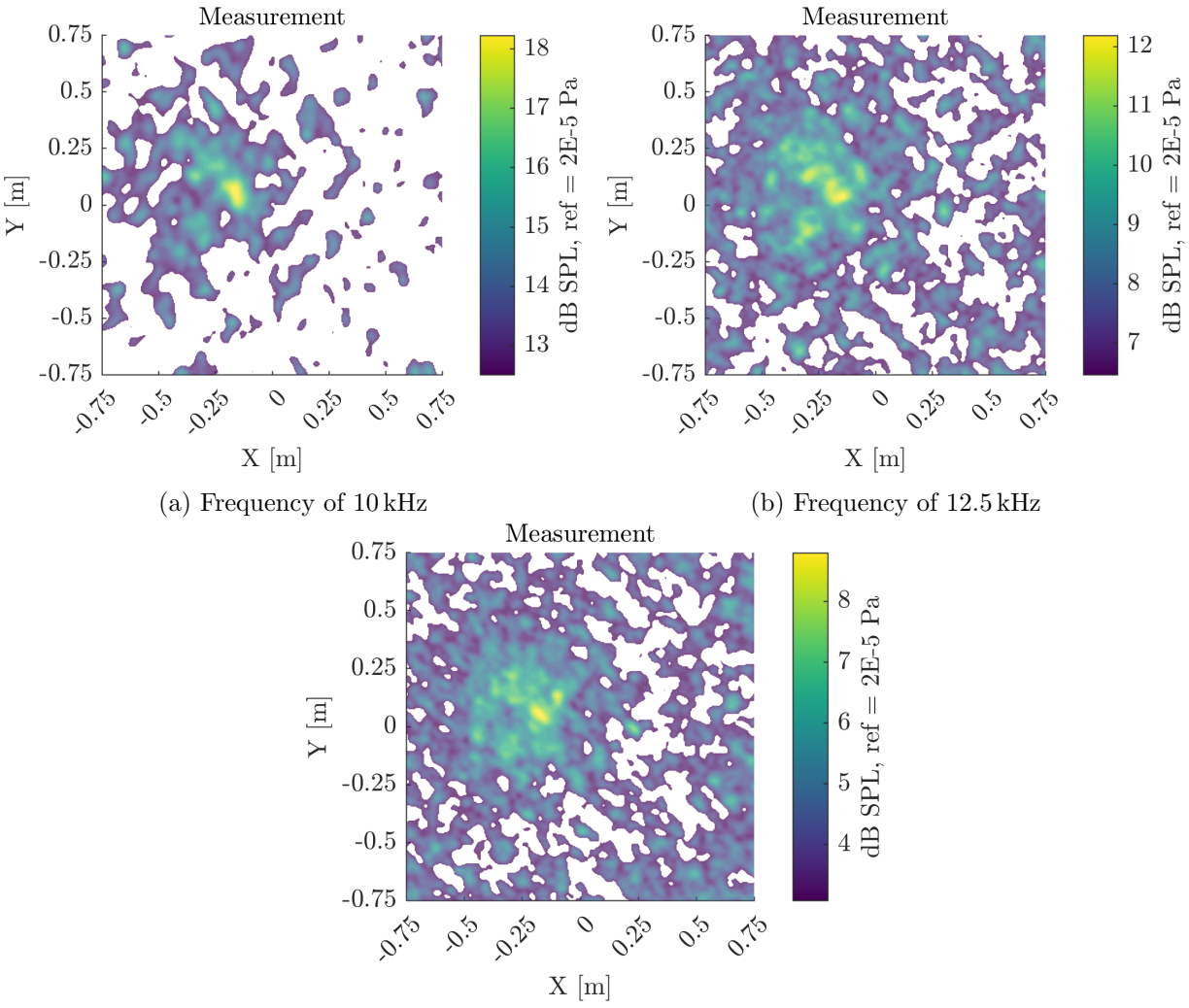

(a) Frequency of 10 kHz

(b) Frequency of 12.5 kHz

(c) Frequency of 15 kHz

Figure A.3.12: Follow up on Figure 7.14. Beamforming results of a hovering DJI Phantom 4 at increased frequencies at 3 m.

PAPER NAME

Msc_Thesis___Ground_Positioned_Phased_Array___JS_s2107910.pdf

WORD COUNT

24217 Words

CHARACTER COUNT

122185 Characters

PAGE COUNT

93 Pages

FILE SIZE

17.6MB

SUBMISSION DATE

Sep 11, 2024 3:23 PM GMT+2

REPORT DATE

Sep 11, 2024 3:25 PM GMT+2

12% Overall Similarity

The combined total of all matches, including overlapping sources, for each database.

- 8% Internet database
- 9% Publications database
- Crossref database
- Crossref Posted Content database
- 1% Submitted Works database

Excluded from Similarity Report

- Bibliographic material